ABSTRACT

Title of thesis: MONOLITHIC SUSPENDED OPTICAL WAVEGUIDES FOR INP MOEMS

Daniel P. Kelly, Master of Science, 2005

Thesis directed by: Professor Reza Ghodssi
Department of Electrical and Computer Engineering
Institute for Systems Research

A key platform technology for InP optical waveguide MEMS is developed. The novel waveguide design is entirely released from the substrate by sacrificial etching and the suspended waveguide is supported by lateral tethers. This allows free-standing, movable segments of waveguide while preventing substrate leakage loss in fixed segments of the waveguides. The optical, mechanical, and material design process is presented. A single-mask fabrication process is developed that can be extended to more complex devices employing electrostatic actuation. Relative power and Fabry-Perot contrast measurements indicate the fabricated suspended waveguides exhibit a propagation loss of 2.2 dB/cm and tethers induce 0.24 dB additional loss per pair. Future optical MEMS devices built with suspended InP waveguides are briefly introduced.

MONOLITHIC SUSPENDED OPTICAL WAVEGUIDES FOR INP MOEMS

By

Daniel P. Kelly

Thesis submitted to the Faculty of the Graduate School of the
University of Maryland, College Park in partial fulfillment
Of the requirements for the degree of
Master of Science
2005

Advisory Committee:
Professor Reza Ghodssi, Chair
Professor Pamela Abshire
Professor Martin Peckerar

ACKNOWLEDGEMENTS

I would like to thank the committee members: Prof. Martin Peckerar, Prof. Pamela Abshire, and especially my advisor, Prof. Reza Ghodssi, without whom none of this work would have been possible.

I would also like to thank the members of the MEMS Sensors and Actuators Lab (MSAL) for all of their help, advice, insightful discussions, and grueling questions during presentations and critical design reviews. I especially thank Mr. Marcel Pruessner and Dr. Madhumita Datta for their perspectives and insights on InP and optical MEMS related issues.

Many individuals at the Laboratory for Physical Sciences (LPS) assisted with this research. I would especially like to thank Mr. Kuldeep Amarnath for his countless hours spent training and advising me with fabrication, packaging, and optical testing issues. I would also like to acknowledge Dr. Rohit Grover for his advice and guidance, Mr. Lynn Calhoun for MBE growth, Prof. Ping-Tong Ho for use of the optical testing system, Mr. Toby Olver for cleanroom access, and Mr. Steve Brown for training and assistance with the projection lithography system, including the fine art of Post-It™ note leveling.

Finally, I wish to acknowledge and thank the sponsors for funding this research: the National Science Foundation (NSF) and the Laboratory for Physical Sciences (LPS).

TABLE OF CONTENTS

LIST OF TABLES

LIST OF FIGURES

Chapter 1 – Introduction and Motivation

1.1 Introduction to MEMS

Micro-electro-mechanical Systems (MEMS) integrate electrical and mechanical functions on the micro-scale. Traditional semiconductor chips can only read, process, and output electrical signals; exterior sensors and actuators must be used to convert mechanical functions to electrical signals and back again. Only in this way can a semiconductor chip interact with the physical world. These exterior sensors and actuators can be bulky and expensive and make packaging of a system a more complex and difficult process. MEMS, however, can exploit traditional semiconductor microfabrication processes to create mechanical sensors and actuators on the same size scale as a chip to ease packaging and interconnection (hybrid integration), or even directly on the microelectronic circuit (monolithic integration). In this manner, MEMS allow complex mechanical and electrical systems to be integrated in a small, robust, compact, batch manufacturable package.

Combining modern microelectronics with micro-scale mechanical systems on a single chip fabricated with batch-process techniques provides many opportunities and advantages over macro-scale systems. Perhaps foremost is cost – small size and batch-process fabrication combined with a simpler assembly make it easy for a MEMS device to cost orders of magnitude less than a similar macro-scale device. MEMS also offer the potential for many systems to be fabricated simultaneously on a single wafer using existing micro fabrication processes. Due to their small size, MEMS can also offer

functionality beyond macro systems. Some of the most common commercial MEMS devices are accelerometers, pressure sensors and temperature sensors. Because of their small size and low cost, these sensors can be placed throughout airplanes, automobiles, and unmanned automated vehicles to constantly monitor and provide feedback about the vehicle's environment and performance.

Although MEMS is a relatively new field, development has taken place at a rapid pace due to the maturity of the IC fabrication techniques MEMS are based on. Constructing MEMS out of the same materials as semiconductor computer chips not only offers the advantage of system integration, it also positions MEMS to be able to benefit from established semiconductor fabrication processing. Semiconductor fabrication techniques have had assistance from incredible amounts of funding and development effort over the past half-century, and are now in a very mature state. Because the same tools for lithography, deposition, and etching are used for MEMS as are used in the microelectronics industry, the tools and processes needed are already in place. Traditional microelectronic circuit fabrication, however, is strictly a 2-dimensional process. In order to break into the third dimension required for mechanical structures, several new MEMS fabrication techniques have been introduced. Two of the most common are bulk micromachining and surface micromachining.

In bulk micromachining, the "bulk" substrate is removed beneath the MEMS device in order to create a free-standing structure [1]. The substrate can be etched away by either wet chemical etchants, or through the use of dry etching such as Reactive Ion Etching (RIE). Bulk micromachining can create very large structures, however it is difficult to define precise vertical dimensions. An example of a commonly fabricated

device using bulk micromachining is a thin, pressure-sensitive membrane. Sensors or actuators can be fabricated on top of the substrate, then the substrate beneath the membrane is removed to create the MEMS device.

Surface micromachining can be used to create free-standing structures above the substrate with very well-defined vertical dimensions [2]. In surface micromachining, a sacrificial layer is deposited on the substrate beneath the device layers. After patterning the device layers, the wafer is submersed in a chemical etchant which selectively removes only the sacrificial layer, leaving the device suspended and free to move. This method lends itself well to capacitive and electrostatic MEMS devices since layer thickness can be very well controlled.

1.2 MEMS in Optical Applications

Optical MEMS, or Micro-Opto-Electro-Mechanical systems (MOEMS), are microfabricated devices that combine electrical, mechanical, and optical functions. Optics and photonics present a great potential for communication systems and networks: high transmission rate, high data density, and low power are all key aspects of an optical system. In particular, optical fiber communications networks have revolutionized networking in the past years. Optical networks can transmit data at speeds over 40 Gb/sec [5], and do so with very low signal attenuation. Originally, a significant drawback to optical communications networks was routing and switching, which had to be performed in the electrical domain. This meant converting an optical signal into an electrical signal, processing and routing, then converting the electrical signal back to the

optical domain and retransmitting. This optical-electrical-optical (O-E-O) bottleneck greatly reduces the overall speed of optical networks. Ideally, the transmitted optical signal should remain in the optical domain throughout the network in order to achieve the greatest speed and lowest power consumption. In order to realize this, all-optical switching, processing, and routing is required. By using electrooptical and thermooptical effects to modulate an optical material's index of refraction, an optical signal can be routed by making use of constructive and destructive interference such as in a Mach-Zender interferometer or micro-ring resonator [4, p. 326].

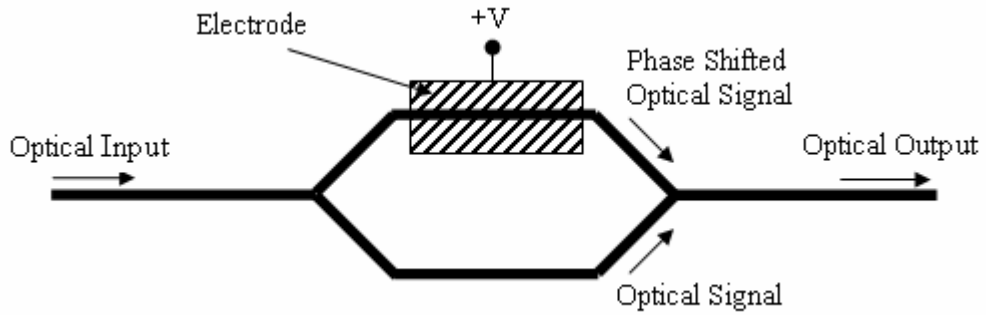

Figure 1-1: Schematic of Mach-Zender interferometer. An electric field is used to modulate the optical path length of the top branch and cause constructive or destructive interference when the two branches recombine.

The drawback of these types of all-optical switches is that they are wavelength dependant, polarization dependant, or both. This puts tight restrictions on the optical system, especially for wavelength division multiplexed (WDM) data. In order to maximize the data density in an optical communication system, multiple wavelengths or "channels" can be transmitted in the same fiber. By then filtering the output to the desired wavelength, each channel of data can be individually addressed. This transmission scheme is wavelength division multiplexing. Because WDM employs multiple wavelengths transmitted on a single fiber, wavelength-dependant switching

involves many challenges. For optimum performance, optical communications systems require switching and routing components that are insensitive to wavelength and polarization, have large output isolation, and are scalable to a large number of channels. One solution is to employ optical MEMS.

Optical MEMS devices bring a new capability to the table that traditional optics can not match – the ability to physically manipulate the optical path. Since MEMS devices do no rely on optical interference or polarization birefringence to manipulate the optical path, they can be entirely wavelength and polarization independent. Optical MEMS also have an advantage over macro-systems – their dimensions and scale of movement are on the same order of magnitude as the wavelength of light. So while macro-systems need a very high precision and accuracy to be able to physically direct an optical beam, MEMS devices inherently have this high precision since the manipulations involved are on the same order of magnitude as the system itself.

Two well-developed optical MEMS devices are micro-mirrors to direct light and membranes for tunable Fabry-Perot filters. One of the most well established and commonly discussed micro-mirror devices is the Texas Instruments Digital Micromirror Device (DMD) [5] (Figure 1-2). The DMD chip consists of up to 1280 x 1024 micromirrors in a 2-D array. Each aluminum mirror is 16 μm square and can be tilted up to +/- 12° from the vertical axis with a switching time of 2 μs. This type of micromirror device can be used in an optical network as a switch to perform all optical switching and routing. Not only is this device insensitive to wavelength and polarization, but due to its 2D array layout it is capable to scaling to a large number of channels.

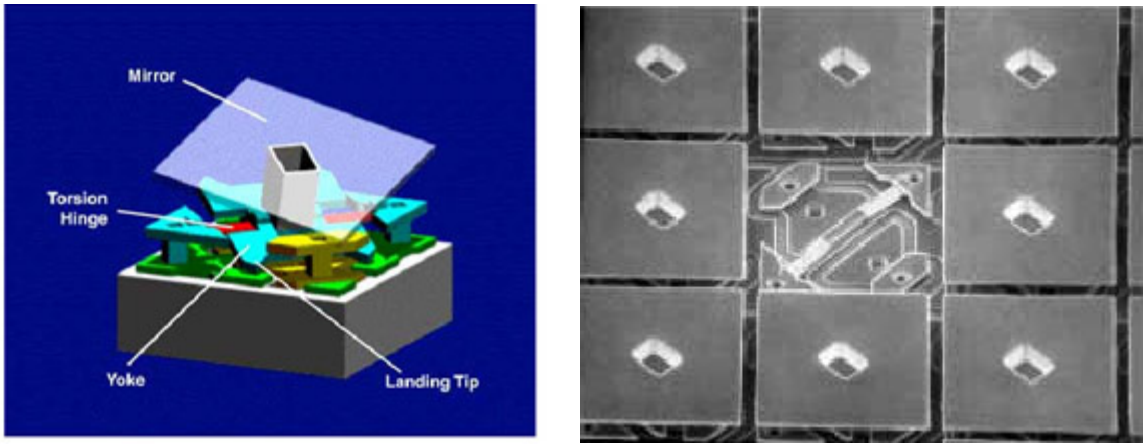

Figure 1-2: Schematic view of Texas Instruments digital micromirror (left), and SEM of 9 micromirror devices (right). The center mirror has been removed to expose the actuation mechanism [5].

Lucent's WaveStar^{TM} LambdaRouter (Figure 1-3) uses micromirrors similar to the Texas Instruments device, but the array of mirrors is used to generate a 256 channel all-optical router capable of handling over 10 Tb/s of network traffic [6]. Although these 2-dimensional arrays of micromirrors can achieve large channel densities, they can only operate on light in a path perpendicular to the surface of the substrate. They are thus limited to 3-dimensional, hybrid optical systems.

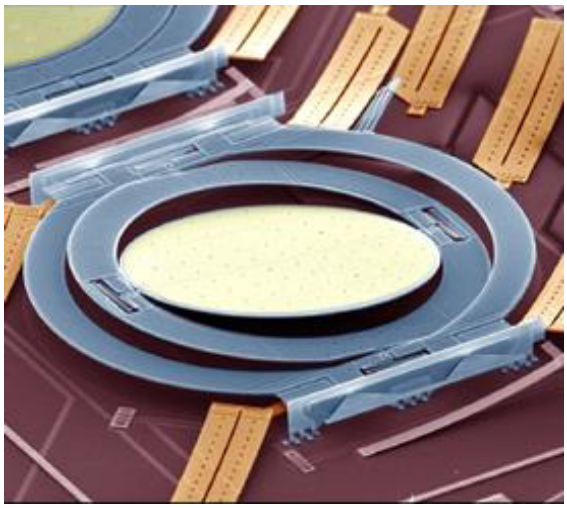

Figure 1-3: SEM of a micromirror in Lucent's WaveStar^{TM} LambdaRouter.

Another important component of a WDM communication system is a tunable filter. Fabry-Perot tunable filters can be very precisely fabricated and controlled using MEMS surface micromachining. The InP tunable filter shown in Figure 1-4 uses two vertically stacked Bragg reflectors with an electrostatically tunable gap to create a MEMS tunable filter [7]. While the use of surface micromachining allows very precise control of the layer and gap thicknesses, a significant drawback is that due to the vertical design, this type of filter is only useful as a component in a hybrid system.

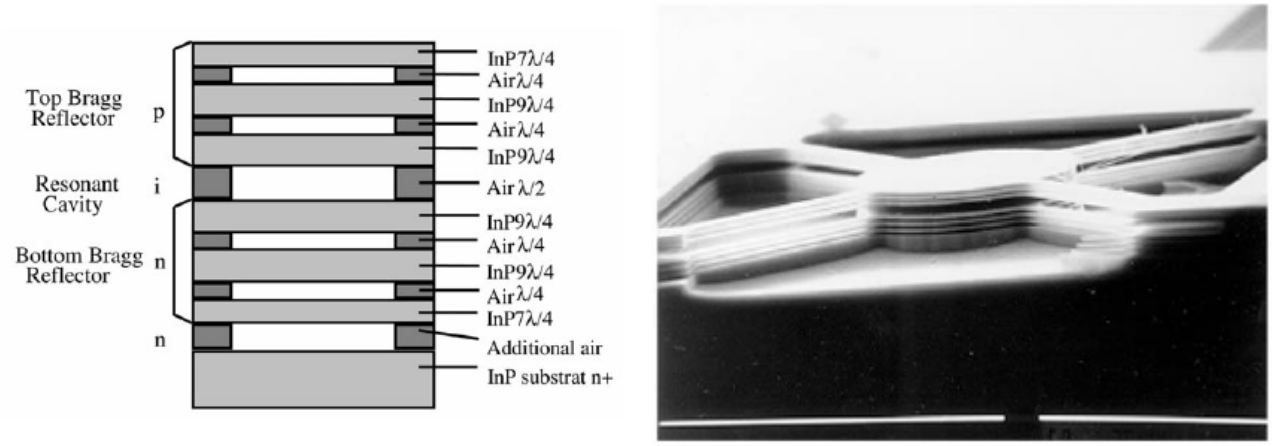

Figure 1-4: Layer structure (left) and SEM micrograph (right) of a vertically stacked, tunable MEMS Fabry-Perot filter [7].

1.3 Free Space MOEMS versus Confined MOEMS

Optical MEMS span many devices and applications, but in general can be categorized into two groups – free space and confined MOEMS. Free space optical MEMS are used to interact with light in a 3-dimentional system such as the micro-mirror and Fabry-Perot filters discussed previously. These devices have the advantage that they are based on currently-existing MEMS structures such as mirrors and membranes which are well studied and established. These traditional MEMS devices are then applied to the

optical domain to create optical MEMS devices. Being based on commonly used MEMS structures, the fabrication and development of free-space MEMS can be accelerated. Free-space optical MEMS also have great scalability. Since the third dimension in space is utilized, free-space MEMS devices can address a very dense number of channels. This makes an excellent technology for discrete packaged optical network components. However, packaging of free-space optical MEMS is challenging due to the precise alignment required in all three dimensions. This also leads to components that can be very sensitive to shock and care must be taken when dealing with free-space MEMS devices. As a result, free-space MEMS are expensive components, adding to the expensive and sometimes prohibitive cost of establishing and maintaining an optical network. If a component can integrate several functions of an optical network with a less complex packaging scheme and a more mechanically robust system is available, the costs of implementing an optical network could be lowered substantially. Confined optical MEMS offer a great potential in this area.

Rather than beginning with traditional MEMS structures and applying them to the optical domain as is done in free-space MEMS, confined MEMS take the inverse approach. Confined optical MEMS begin with traditional integrated optical structures [8] such as waveguides, then apply them to the mechanical domain. Since integrated optics is a planar technology (optical routing is confined to the plane of the substrate), the resultant confined optical MEMS, or waveguide MEMS, are also planar in nature. Although this means fewer channels can be implemented in a given volume, it makes packaging of the MEMS devices far more compact and straightforward. The real advantage of waveguide MEMS, however, is the potential for integration of multiple

optical functions. By beginning with integrated optics, there is the potential to create an optical MEMS system on a chip. With edge-emitting lasers, active amplifiers, mechanical switches, and tunable filters (either mechanical or optical), entire WDM transmitters and receivers could be implemented monolithically – one of the ultimate goals of optoelectronics [9].

An example of a confined optical MEMS device is shown in Figure 1-5. This device is a 1x2 waveguide switch implemented in GaAs. Lateral electrostatic actuation is used to direct the input waveguide to align with either of the two output waveguides. By cascading several of these switches, a 1xN switch can be implemented. A similar switch implemented in silicon is shown in Figure 1-6.

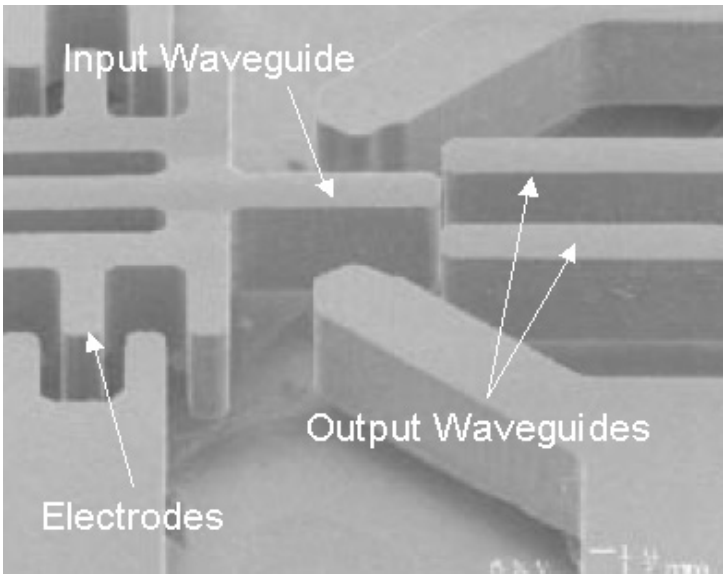

Figure 1-5: GaAs 1x2 waveguide switch [10].

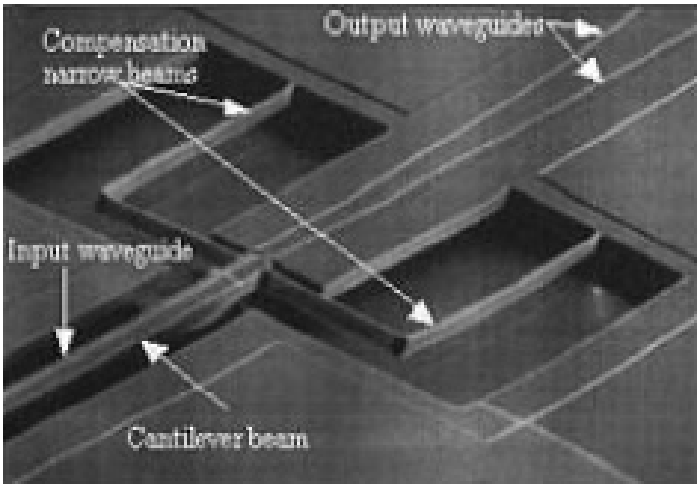

Figure 1-6: Silica 1 x 2 waveguide switch [11].

The thermo-capillarity based waveguide switch shown in Figure 1-7 is another example of a waveguide optical MEMS device. The device has relatively low loss, with a transmission loss of 0.11 dB and a reflection loss of 1.3 dB. The use of thermal actuation limits the speed of the device to 6 ms. Another drawback to this device is that the waveguides are silica and silicon based. Although silicon is a very well-established material and has many desirable properties, silicon-based optical MEMS are limited to passive operation.

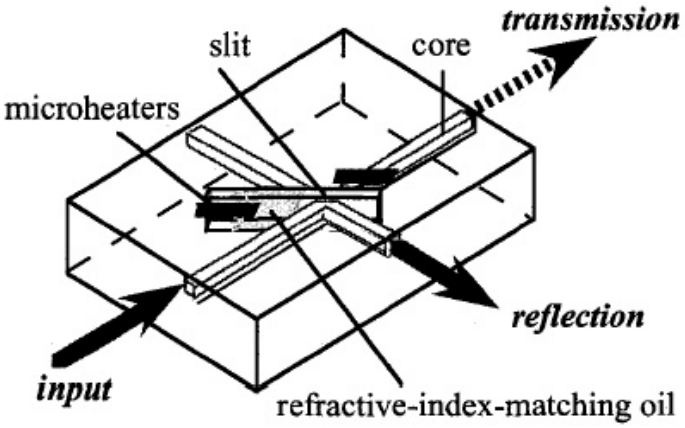

Figure 1-7: MEMS intersecting waveguide switch based on thermo-capillarity. By heating the index-matching oil, the optical path can either be transmitted or reflected at 90□, resulting in a planar 1x2 waveguide switch [12].

1.4 III-V Based MOEMS

Silicon is perhaps the most well known and well studied semiconductor material. Silicon offers excellent electrical properties, very good mechanical properties, and silicon fabrication processes are extremely mature. One distinct area where silicon falls short, however, is as an optical material. Silicon has an *indirect* bandgap, as shown in Figure 1-8. This means that both a transfer of energy and of momentum is required for an electron to fall from the conduction band to the valence band. Photons have a very small momentum ($h\nu/c$), as a result, photons are not generated by this transition and silicon cannot be used to generate light. There are many applications where strictly passive integrated optics is acceptable, however this requires the use of external optical sources and amplifiers. If one examines other groups of semiconductors, it becomes apparent that there is another class of semiconductor crystal – those with a *direct* bandgap such as InP as shown in Figure 1-9.

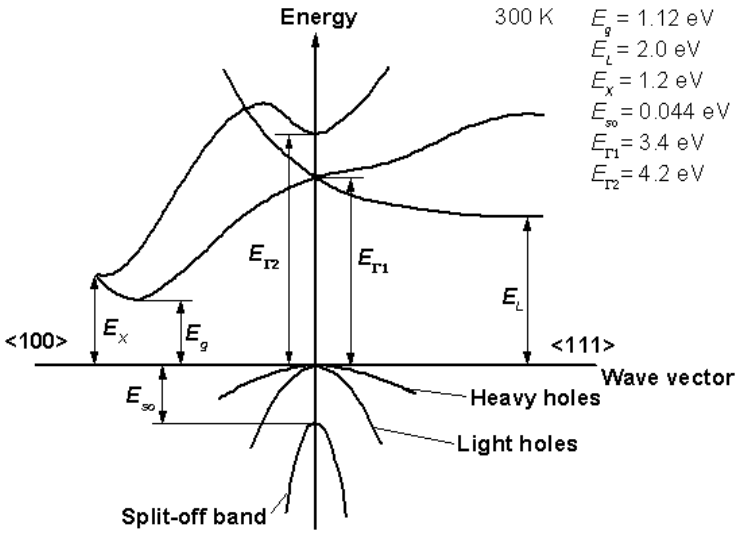

Figure 1-8: Silicon energy band diagram [13].

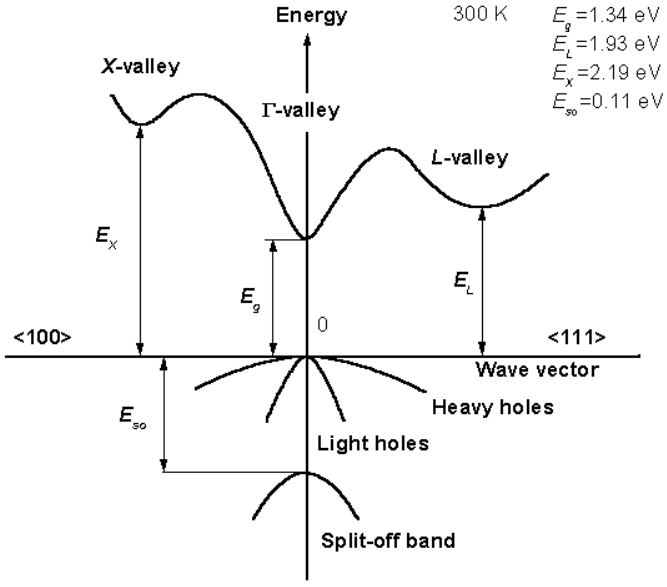

Figure 1-9: InP energy band diagram [13].

Crystal structures with a direct bandgap have both the minimum energy of the conduction band and the maximum energy of the valence band at the same momentum. So when an electron falls from the conduction to the valence band, only energy needs to be conserved and there is the possibility of a photon being generated. Figure 1-10 depicts the differences between a direct and indirect bandgap in photon generation. Semiconductors composed of elements from groups III and V are known as III-V semiconductors and have this direct bandgap. Examples of III-V semiconductors include InP, InGaP, InGaAsP, GaAs, AlGaAs, etc.

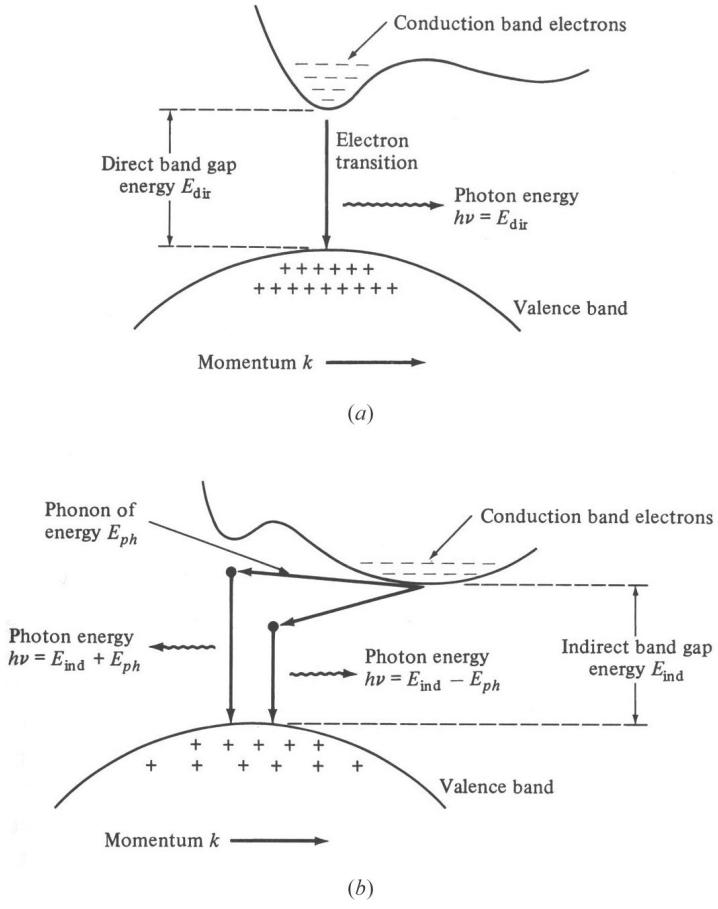

Figure 1-10: "(a) Electron recombination and the associated photon emission for a direct-band-gap material; (b) electron recombination for indirect-band-gap materials requires a phonon of energy E_{ph} and momentum k_{ph}" [14, p. 149].

There are several other advantages to using a III-V semiconductor substrate. Since crystals in the same basic group, such as the InP group or the GaAs group, have very similar structures, they can be grown epitaxially. This results in a multi-layer, single-crystal wafer with precisely controlled layer composition, thickness, and atomically-abrupt layer junctions. When these properties are combined with the ability to actively generate photons, intricate integrated optical circuits involving edge-emitting lasers, active amplifiers, waveguides, and filters can be designed and fabricated. If MEMS functionality could also be added to the integrated optical circuit, wavelength independent and high selectivity switches and tunable filters can be integrated as well. This opens the possibility for highly functional monolithic integrated optical MEMS circuits. Even a single component such as an optical MEMS switch can benefit greatly from fabrication using III-V semiconductors. Active optical amplifiers can supply gain to offset attenuation caused within the switch so that internally loss-compensated switches can be designed and fabricated.

1.5 InP as MOEMS Material

To date, extensive MEMS development has been performed using GaAs [10,15-16]. GaAs has many benefits – it has good material properties, substrates are less expensive than other III-V materials, and fabrication is well established. The area where GaAs leaves something to be desired, however, is its wavelengths of active operation. Figure 1-11 shows a graph of wavelength vs. attenuation in optical fiber. The fiber attenuation displays a distinct minimum at 1550 nm, making this wavelength optimal for optical

communications systems and networks – especially for long-haul transmission. The disadvantage of GaAs as a optical MEMS material is that it is not compatible with active operation at 1550 nm. The plot of fiber attenuation shows a local minima at 900 nm, which can be addressed with GaAs, however this is less than ideal. One of the main concerns in optical systems is low power consumption, so operating at the wavelength that incurs the least fiber transmission loss is a high priority.

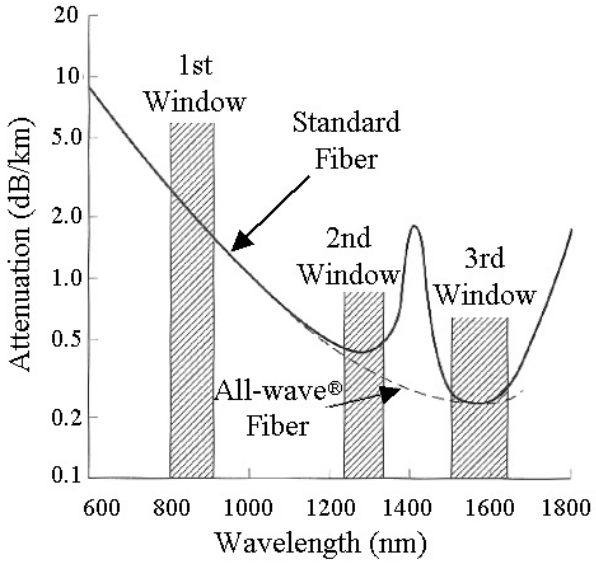

Figure 1-11: Optical fiber attenuation versus wavelength. The dashed line is for a water-free fiber [14, p.93].

The InP material system is capable of operation at the minimum fiber attenuation wavelength. Strained quantum wells can be grown in InGaAsP that produce light at 1550 nm [17], so InP is a good candidate for creating active integrated optical components. For this reason, we are investigating and developing InP as an optical MEMS material. In the future, incorporation of InP integrated optical components with InP optical MEMS

components would allow fully active, monolithic, integrated optical MEMS systems with operation at 1550 nm.

Although InP has been thoroughly studied and developed as an optical material [17,18], research to discern the mechanical properties of InP and its suitability for MEMS is limited [19-21]. Our first step was to develop mechanical test structures in InP to extract the thin-film material properties of InP *as grown at our facilities*. The detailed results of this research can be found in [22]. We determined that, although InP is a brittle material, it has acceptable mechanical properties for small displacements. For a 1 x 2 waveguide switch , the maximum mechanical displacements needed are on the order of 3 times the waveguide width (~3-6 μm). For a tunable filter, only nanometers of displacement are required. Over these small displacements, the mechanical properties of InP have proven to be perfectly acceptable.

The next step in the development of InP waveguide MEMS is to demonstrate free-standing waveguides that can be electrostatically actuated. These MEMS waveguides will serve as the building block for the future design and fabrication of InP optical MEMS and will offer the potential for active, monolithic, integrated optical MEMS circuits operating at 1550 nm.

1.6 Thesis Outline

The purpose of the research presented here is to develop and characterize free-standing optical waveguides in InP which will become the building block for InP optical waveguide MEMS. It is important that the waveguides have good optical performance as well as good mechanical characteristics. The fabrication scheme should be as simple as possible since these waveguides will be incorporated into more complex devices. Finally, it is important to have a thorough characterization of the waveguides in order to facilitate the design of future waveguide MEMS devices.

The second chapter of this thesis will describe the design considerations for creating free-standing, movable waveguides and the challenges imposed by doing so in the InP material system. The concept of a suspended waveguide will be introduced and the effects of the suspension discussed. Simulation and design of the suspended waveguide will be presented. Finally, the proposed waveguide dimensions and layer structure will be given.

The third chapter presents the fabrication of suspended InP waveguides. The growth of the initial material is performed in-house and important details are covered. A general overview of the fabrication sequence is then given, followed by a detailed description of each step. Finally, images and measurements of fabricated suspended waveguides are presented.

The fourth chapter describes the optical characterization of the waveguides. The experimental apparatus and procedures are given, followed by the results of the characterization.

The fifth chapter is a summary of the work presented here and an analysis of the results. The optical properties and fabrication sequence of InP suspended waveguides are the most important contribution of this work. Given the optical properties, these waveguides can be used to design complex InP optical MEMS devices. With a well established, robust fabrication process, the production of these MEMS devices is greatly simplified and can be performed rapidly. The extension of suspended waveguides into creating actual devices is discussed along with several applications currently being developed.

Chapter 2 – Design of Suspended InP Waveguides

This chapter will describe the design considerations for creating free-standing, movable waveguides and the challenges imposed by doing so in the InP material system. The concept of a suspended waveguide will be introduced and the effects of the suspension discussed. Simulation and design of the suspended waveguide will be presented. Finally, the proposed waveguide dimensions and layer structure will be given.

2.1 Challenges of Movable InP Waveguides

In order to design and fabricate an optical waveguide MEMS device, it is necessary to have waveguides that can be mechanically actuated. This requires waveguides that are released from the substrate, for example through surface micromachining. To retain the optical properties of the InP substrate lattice, a single-crystal wafer growth is necessary. Thus, a sacrificial layer that is both selective and lattice-matched to the substrate and waveguide layers is needed. Fortunately, the InP material system is well suited for surface micromachining due to the excellent etch selectivity between several of the lattice-matched InP compounds [23]. Both InGaAs and InGaAsP can be epitaxially grown lattice-matched to an InP substrate and are 100% selective to InP in several etchants. By incorporating a perfectly selective, lattice-matched layer beneath the waveguides, a sacrificial release can be used to separate the waveguides from the substrate and allow mechanical movement.

Using a lattice-matched sacrificial layer to release the InP waveguides presents challenges in several other areas. Other material properties such as refractive index and the requirement for minimal growth defects make the selection of an appropriate sacrificial layer difficult. Table 2-1 outlines several possible waveguide/sacrificial layer material combinations.

Waveguide Layer	Sacrificial Layer	Waveguide Index	Sacrificial Layer Index	Challenges
$In_{.69}Ga_{.31}As_{.66}P_{.34}$	InP	3.41	3.17	Thick InGaAsP gowth is difficult
$In_{.53}Ga_{.47}As$	InP	3.53	3.17	InGaAs: Eg ~ 1600 nm
InP	$In_{.53}Ga_{.47}As$	3.17	3.53	InGaAs has larger index

Table 2-1: Table of possible core/cladding and sacrificial layer materials. Data compiled from [24,25].

An InGaAsP waveguide with InP as a sacrificial layer would work well as far as etch selectivity and optical index contrast are concerned, however InGaAsP has a problem with epitaxial growth of thick layers. Due to fiber and waveguide alignment constraints, MEMS waveguides should be at least on the order of 1 μm thick. However, for InGaAsP thicknesses greater than a few hundred angstroms, the material exhibits spinodal decomposition and the resulting compositional nonuniformity is not tolerable for optical material [26]. This not only prevents the use of InGaAsP as the waveguide layer, but also as the sacrificial layer, since defects will propagate into subsequent layers and the sacrificial layer must be thick enough to prevent stiction and ensure good device reliability and yield. Another potential material choice would be to use InGaAs for the waveguide core and cladding and InP as the sacrificial layer. The bandgap wavelength of

as-grown lattice-matched InGaAs is around 1620 nm, as shown by Figure 2-1. As a result, the material will absorb photons with a larger energy than those at 1620 nm and light at 1550 nm will exhibit a large absorption loss in InGaAs. The final possibility is to use an InP waveguide layer and an InGaAs sacrificial layer. This combination has good potential, until the optical index contrast is taken into account. InGaAs has an index of 3.5, while the index of InP is 3.17. So any InGaAs sacrificial layer beneath the waveguides will couple optical power from the core, leading to large substrate leakage loss. However, if the *entire* InGaAs sacrificial layer underneath the waveguide were to be removed, the leakage loss would be eliminated. This has inspired us to design waveguides that allow removal of the entire InGaAs sacrificial layer, resulting in a monolithic, substrate removed, low-loss waveguide with both fixed and movable segments.

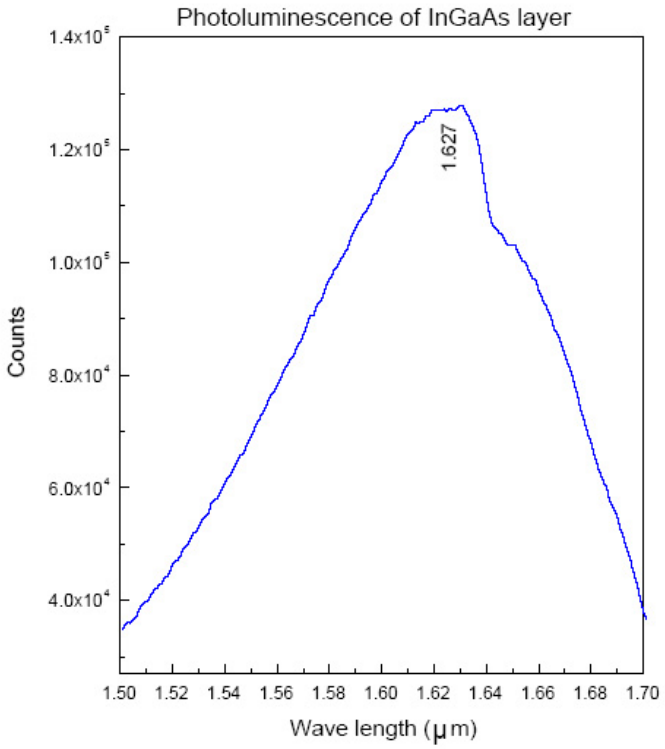

Figure 2-1: Bandgap of as-grown InGaAs as measured by photoluminescence [courtesy: S. Kanakaraju].

2.2 Suspended InP Waveguides

Due to the optical and material properties of InP compounds previously discussed, there is no obvious or easy choice of a sacrificial layer that can be epitaxially grown beneath an InP waveguide. The best available combination is to use InP for the waveguide core and cladding layers, and InGaAs as the sacrificial layer. The underlying InGaAs layer would impose large optical losses on the InP waveguides, but this combination is the only viable option. If the InGaAs were to be entirely removed from beneath the InP waveguides, however, the leakage losses would be totally prevented. Removing the entire layer would leave the waveguides unattached to the substrate, so some alternate mechanism for securing the waveguide structure would be needed. Our solution is the suspended InP waveguide, as shown in Figure 2-2.

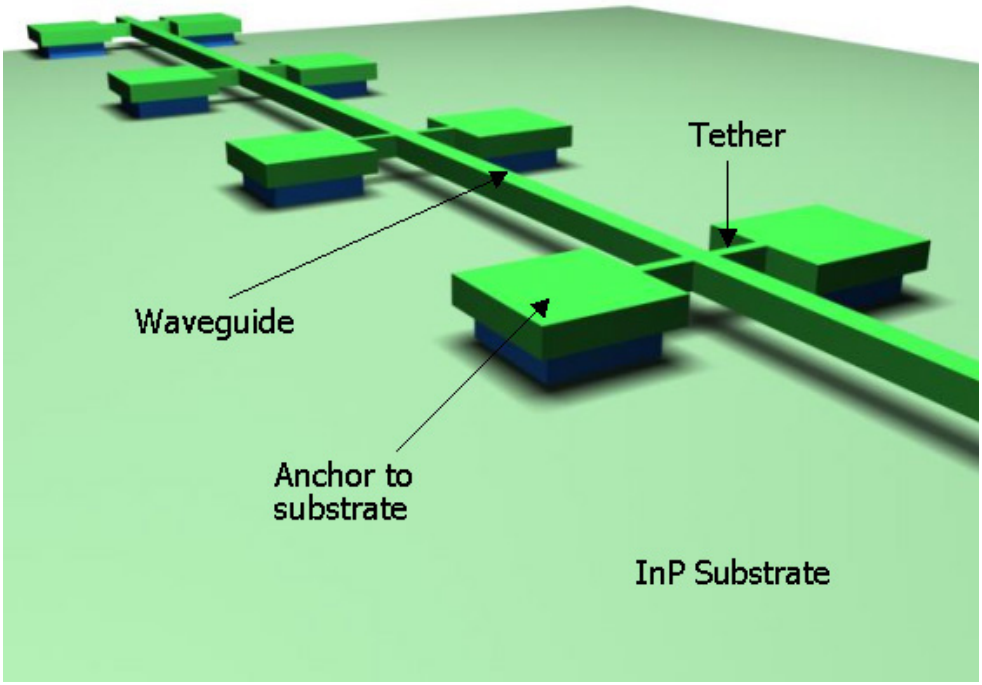

Figure 2-2: Conceptual schematic of suspended InP waveguide.

In order to support the waveguide after the sacrificial release, lateral tethers are incorporated at regular intervals along the waveguide. The tethers are fabricated out of the waveguide material layers and are patterned in the same step as the waveguides. Each tether is then fixed to the substrate through InGaAs that is unetched due to masking by InP. In this way, fabrication remains a single mask process so that it is no more complex than fabrication of the waveguide alone. Figure 2-3 shows how movable waveguides can be implemented using this design. Cantilever sections of the waveguide remain fixed at one end while the other end can be actuated. If the material is doped, electrostatic actuation can be employed by incorporating electrodes to either side of the waveguide.

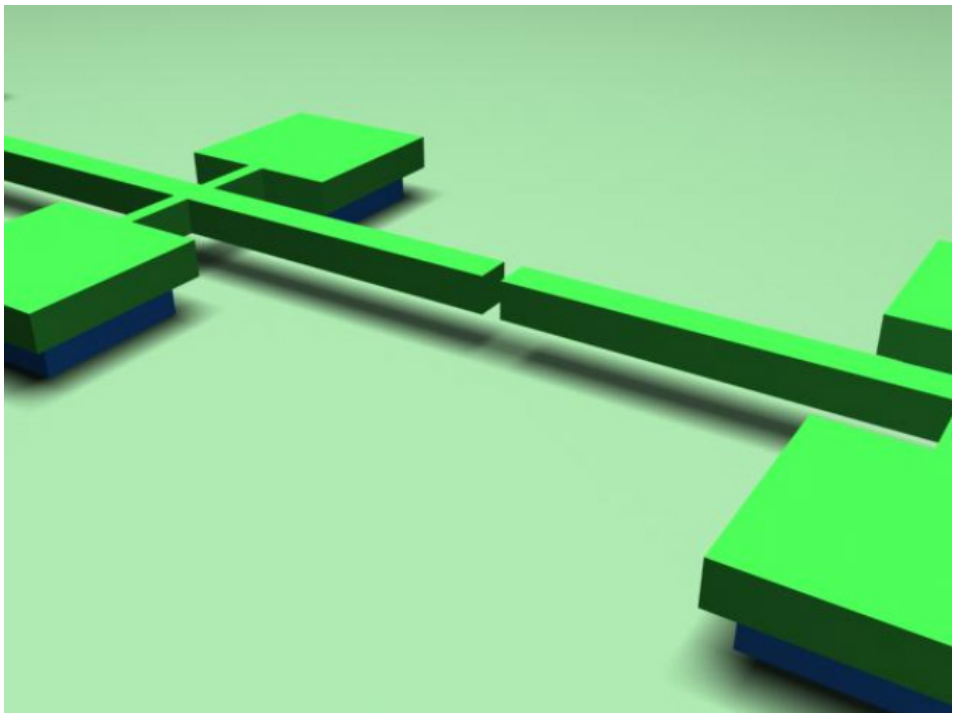

Figure 2-3: Schematic of cantilever section of a suspended waveguide. The cantilever sections are free to move to allow actuation through electrostatic or other means.

Introducing tethers into the waveguide design has several effects. The mechanical support provided by the tethers is a desired effect and is necessary to suspend the waveguide. The shorter the suspended waveguide segments between tethers, the stiffer and stronger the mechanical support will be. On the other hand, the additional optical loss incurred is an undesirable effect of the tethers. The optical loss caused by the tethers is due to beam expansion within the tether (Figure 2-4). As light propagates down the waveguide (z-direction), it is confined both vertically (y-direction) and laterally (x-direction) by the contrast in refractive index between the waveguide media and air. When the light reaches a tether, the beam is no longer confined in the lateral direction and exhibits Gaussian expansion [4, p.50]. At the end face of the tether, where the waveguide once again provides lateral confinement of the beam, the portion of the optical beam that has expanded into the tether is lost due to reflection and scattering. Additional losses within the tether are caused by reflection due to the effective index contrast between the waveguide structure and the tether structure. These unfavorable optical effects show that it is important to reduce the total number of tethers used to support the waveguides. Minimizing the optical loss per tether is also a high priority.

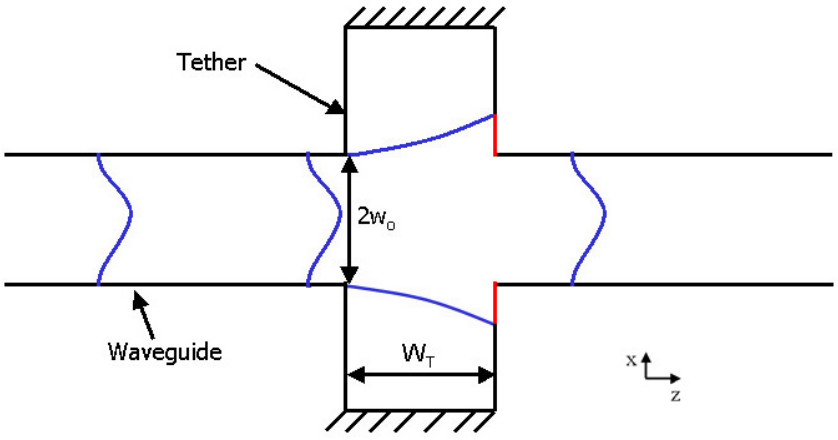

Figure 2-4: Schematic of optical beam expansion within a tether.

2.3 Waveguide Simulation and Design

Several factors contributed to the dimensions of the InP waveguides. In order to achieve single-mode operation, which is necessary for long haul communication systems, the waveguide cross-section should be small (<1 μm). Larger waveguide dimensions facilitate the physical alignment and actuation of the waveguides and reduce loss across gaps and due to misalignments. In order to ease the development of first generation waveguides, dimensions were chosen large enough to facilitate alignment and relieve fabrication tolerances rather than trying to attain single-mode operation. Figure 2-5 shows a cross sectional diagram of the waveguide core and cladding dimensions – the waveguide is 2 μm wide with 1 μm thick upper and lower cladding and 2 μm thick core. The core and cladding refractive indices are a result of the material composition and will be discussed later.

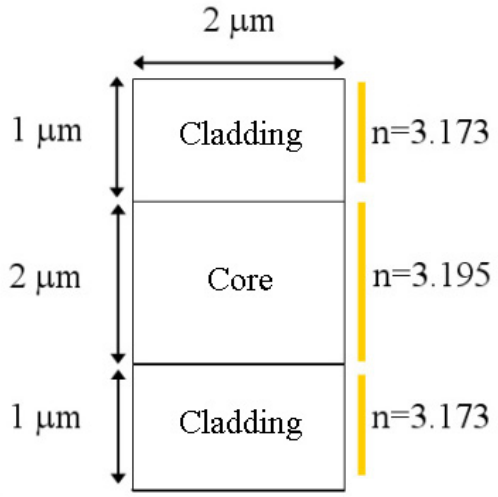

Figure 2-5: Cross section of waveguide showing dimensions and refractive index of the core and cladding.

The software used to solve for optical modes supported by the waveguide is the Optical Waveguide Mode Solver (OWMS) package. This software uses finite element analysis and refractive index boundary conditions to solve for supported modes in an optical structure as well as the effective index seen by each mode. Figure 2-6 shows the 0^{th}, 1^{st}, and 2^{nd} order TE modes in our waveguide structure. These results show that, while several modes are supported, the higher order modes have decreasing effective indices. The effective optical index seen by the 0^{th} order mode is 3.193, while the 2^{nd} order mode already sees an effective index of 2.81. This indicates that a large fraction of the higher order modes are traveling at the air-waveguide boundary and these modes will be very lossy due to scattering at the waveguide-air interface. Although OWMS simulations still indicate multiple supported modes for waveguide dimensions of 1μm x 1μm and less, the simulation does not factor in any loss mechanisms. In reality the higher order modes could become so lossy due to interface scattering and radiation that a waveguide less than 1μm x 1μm could, for all practical purposes, be single mode.

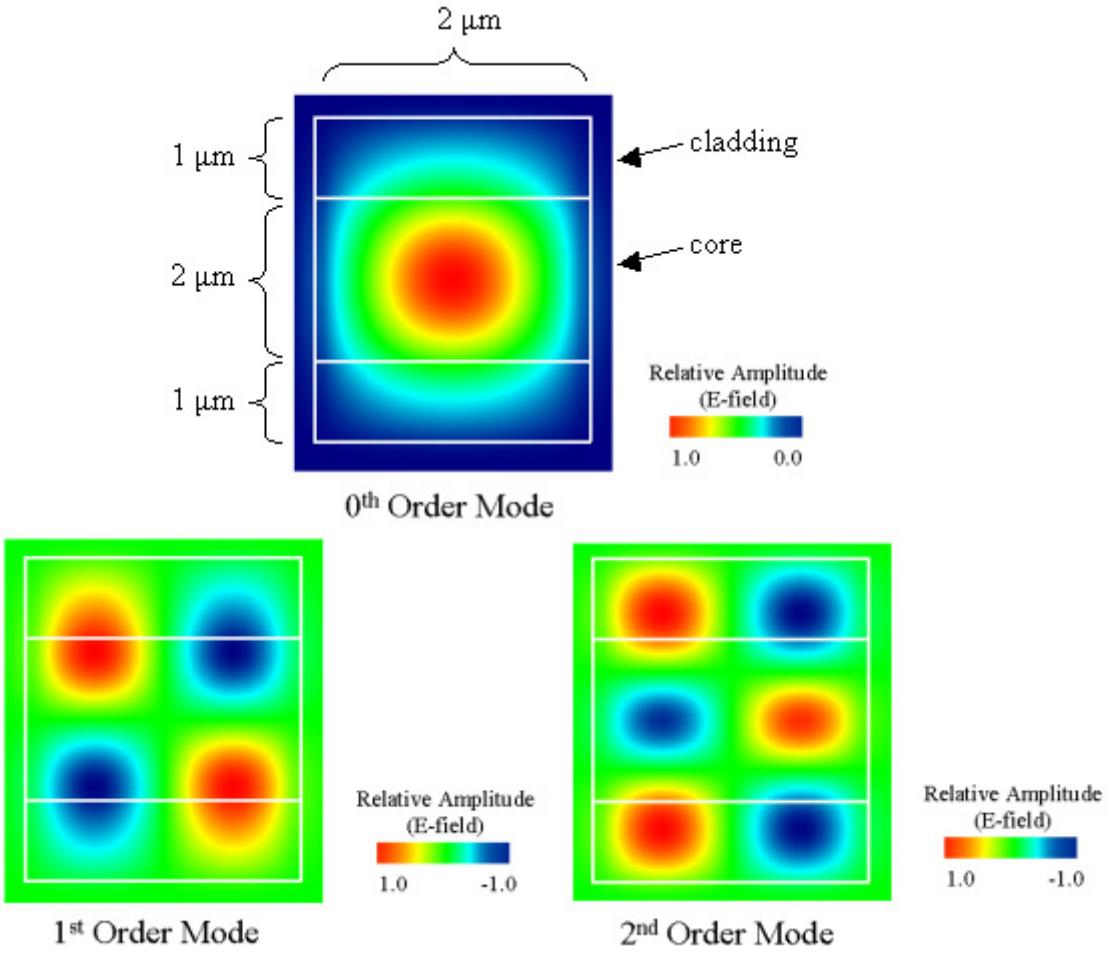

Figure 2-6: Simulated mode field amplitudes for the 0^{th}-2^{nd} order TM modes in the suspended InP waveguide.

2.4 Tether Simulation and Design

One of the primary objectives of this research is to characterize the waveguide tethers for future design and optimization of suspended waveguides. In order to understand and predict the optical effects of the tethers, several Matlab simulations were used. These simulations were used to predict the optical loss of the tether based on

numerous design specifications such as tether width, waveguide width, and material index of refraction. Figure 2-7 shows a top-view schematic of the waveguide, tether, and optical beam.

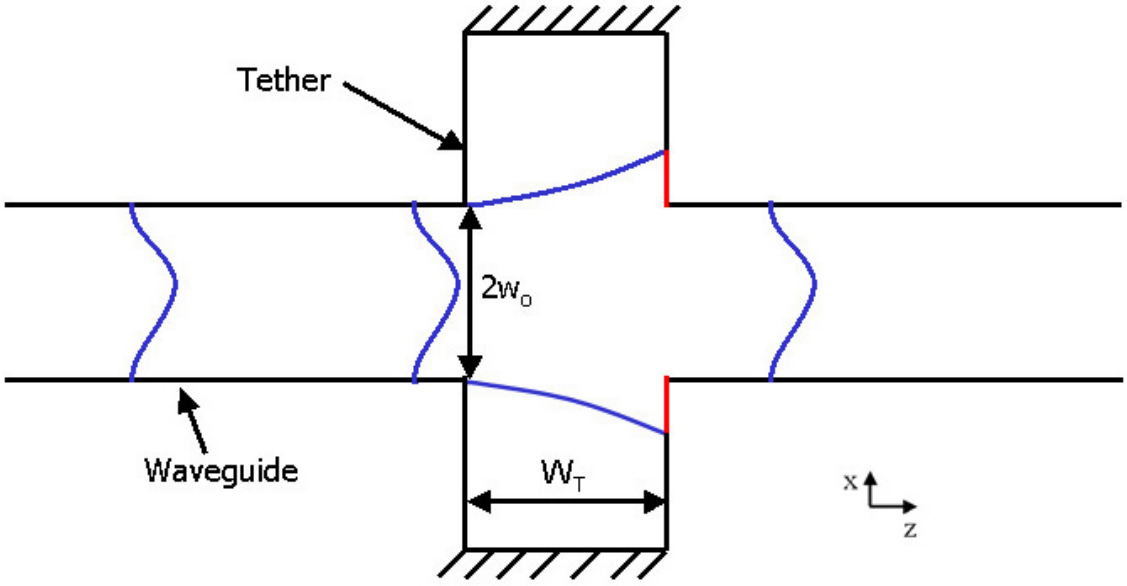

Figure 2-7: Overhead cross-section of waveguide tether, and optical beam propagating down the waveguide. w_o = optical beam radius, W_T = tether width.

The tethers introduce two main causes of loss in this system: loss due to beam expansion and loss due to beam reflection. When the optical beam propagates through the waveguide, it is confined by the refractive index contrasts (Δn) in both the x- and y-directions. At the waveguide-tether interface (z=0), however, the beam is no longer confined laterally (x-direction) and exhibits Gaussian expansion. For a confined optical beam with the confinement removed at the boundary z = 0, the radius of the beam, w(z), is given by equation 2.1 [4, p. 50-53].

$$w^2(z) = \frac{\lambda}{\pi n}\left[\frac{z^2 + (\frac{\pi n w_0{}^2}{\lambda})^2}{\frac{\pi n w_0{}^2}{\lambda}}\right] \tag{2.1}$$

w_0 = beam waist; z = axial distance from beam waist

Where w_0 is the radius of the confined beam at z = 0 (beam waist). This shows that the rate at which the beam expands is proportional to the square of the beam waist, which is dependant on the dimensions and optical confinement of the waveguide. So for a narrow waveguide, on the order of the wavelength being used, with tight confinement, the beam will expand rapidly. Once the optical beam has expanded within the width of the tether and reaches the tether-waveguide interface, z = T_w, the fraction of the beam that is outside the waveguide dimensions will be scattered or reflected back into the tether and lost. This expansion is the greatest contribution to the tether loss.

Reflection losses at the waveguide-tether interfaces are caused by the difference in effective index of refraction of the two structures. While propagating in the waveguide, a small lateral evanescent field travels through the air. Within the tether the optical beam sees only InP in the lateral direction. This causes a slight change in the effective optical index of each structure. As shown by OWMS simulations, the effective index of the 0^{th} order mode in the waveguide is 3.191. An identical simulation with the lateral confinement removed indicates that the effective index of refraction in the tether is 3.194. Due to Fresnel reflection at the step difference in optical index, some amount of optical power will be reflected back at the interface. The amount of reflected power is given by equation 2.2.

$$R = \left[\frac{n_1 - n_0}{n_1 + n_0} \right]^2 \tag{2.2}$$

Using the waveguide-tether Δn obtained from our simulations, the reflection coefficient, R, is 2.2×10^{-7}. This is negligibly small compared with beam expansion losses and is not included in the further simulations.

In order to understand and predict the optical loss due to beam expansion within the tethers, a simple Matlab program was written based on a Gaussian beam expansion and an elliptical propagating mode. The simulation makes two assumptions. The first is that any portion of the original optical mode that spreads outside of the waveguide boundaries is entirely lost due to reflection or scattering at the waveguide-tether interface. To be completely accurate, the waveguide area does not define the fraction of light coupled back into the waveguide, the area of mode overlap defines the coupled power. Because the InP waveguides provide tight confinement (Δn = 2.2), the NA of the waveguide is large and very little of the supported modes travel outside of the waveguide, so it is a good assumption that the fraction of the power within the waveguide area of the interface will continue to propagate. The second assumption is that the power is evenly distributed along the width of the waveguide. OWMS simulations show that the InP waveguides we fabricated are multi-mode, so using a single-mode exponential power distribution could be misleading. An accurate calculation of the power distribution between the lower-order modes is beyond the scope of this work, so we assume a uniform power distribution.

The Matlab simulation performs several functions. First, it calculates the mode radius as a function of distance, z, for a given initial mode diameter, w_0 (equation 2.1). Given the waveguide dimensions, which were obtained by SEM measurements, the

simulation then calculates and plots the fractional loss per tether as a function of tether width based on the overlap area between the fundamental mode and the expanded mode.

$$Loss = \left[\frac{y_{wg}\, w(W_T) - y_{wg}\, w_0}{w_0\, w(W_T)} \right] \tag{2.3}$$

y_{wg} = height of the optical beam; $w(W_T)$ = beam width after the tether width; w_0 = beam waist

Finally, the program calculates the waveguide loss due to tethers as a compound function of the number of tethers, since the magnitude of loss at each tether is a fraction of the power transmitted from the previous tether.

Figure 2-8 - Figure 2-10 show the results of the Matlab simulations. The results predict 0.24 dB loss per tether for our waveguides. This calculation is based on SEM measurements of the fabricated waveguide and tether width. Figure 2-10 indicates that one of the most significant ways to reduce loss due to the tethers is to reduce the tether width. The minimum tether width is defined by physical limitations during fabrication, which will be discussed in the third chapter.

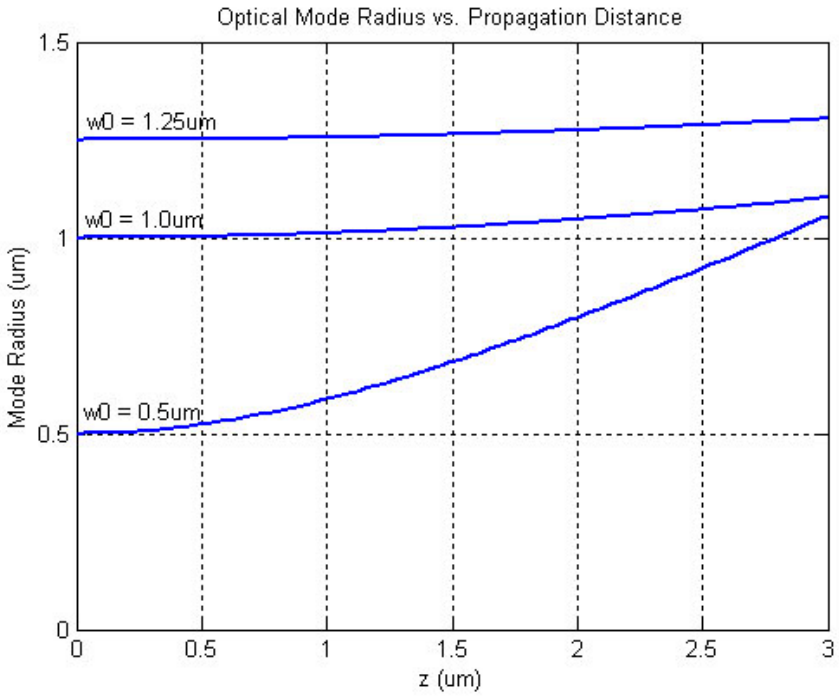

Figure 2-8: Gaussian beam radius, w(z), versus distance, z, for an initial beam waist of 0.5, 1.0, and 1.25 µm.

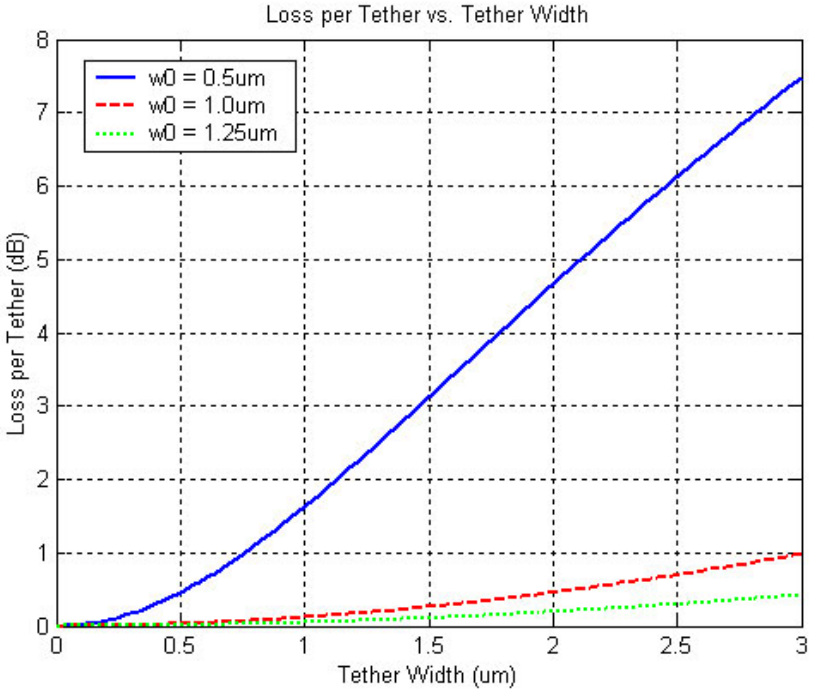

Figure 2-9: Loss per tether versus tether width for a beam waist of 0.5, 1.0, and 1.25 µm.

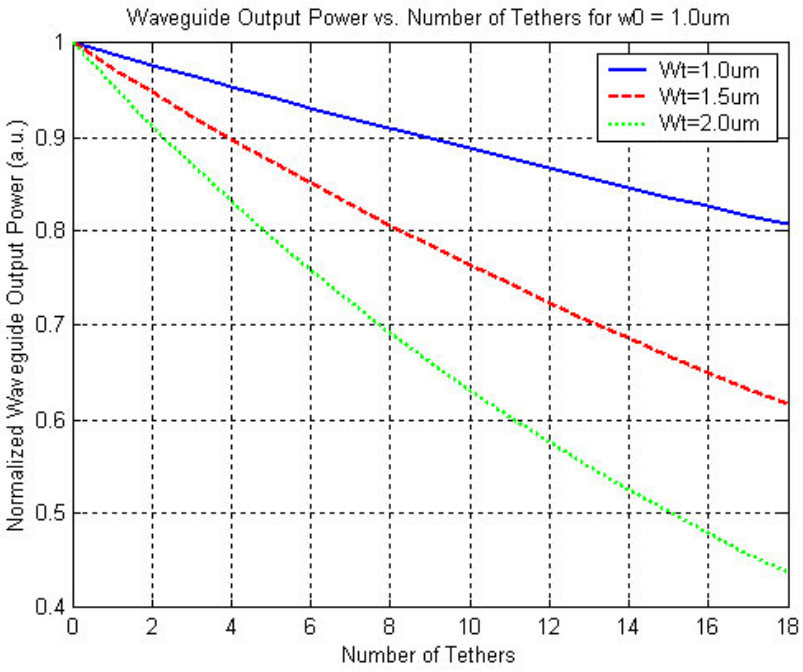

Figure 2-10: Simulated waveguide output power versus total number of tether pairs used to support the waveguide. Results are shown for several tether widths (Wt).

2.5 Material Layer Structure

The material layer structure used for our waveguides is shown in Figure 2-11. All layers are grown using solid-source Molecular Beam Epitaxy (MBE) and are designed to be lattice matched or nearly lattice matched to the (100) InP substrate misoriented 4° toward (111). Growing the wafer epitaxially is important so that the entire wafer is a single-crystal structure. This type of growth also offers many advantages over amorphous layers that are commonly used in MEMS designs. MBE growth uses atoms, in our case from a solid source, and deposits the atoms onto the surface of the wafer while maintaining the temperature and pressure so that each atom will fall into the lowest surface energy state, extending the crystal lattice of the wafer [27, p. 140]. The growth is

very slow, on the order of one monolayer per second, but allows extremely precise control of material composition and thickness and atomically abrupt layer junctions.

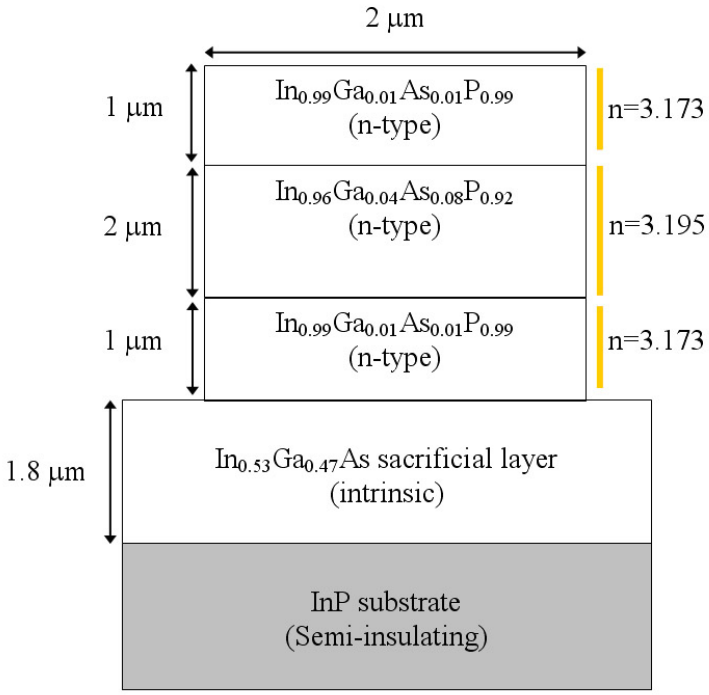

Figure 2-11: Material growth parameters for suspended InP waveguide substrate.

The InGaAsP (n=3.195) core of the waveguide is 2 μm x 2 μm and the upper and lower cladding are 1 μm thick and consist of InGaAsP (n=3.173). The refractive indices of the InGaAsP were calculated based on experimentally developed formulas in [24,25]. The InGaAs sacrificial layer is 1.8 μm thick and has a gallium mole fraction designed to be lattice matched to the InP substrate. The waveguide core is designed to be large in order to relieve tolerances on waveguide-to-waveguide axial alignment for first generation waveguide MEMS devices. This results in a multimode structure, but the dimensions can be decreased for single mode operation in subsequent devices. To allow electrostatic actuation of the waveguides for MEMS devices, the InP layers are doped n-type with a concentration of $5 \cdot 10^{17}$ cm^3 using sulfur atoms while a semi-insulating InP

substrate is used. An n-type doping is used for the waveguide layers because as-grown InP naturally has an electron concentration of about 10^{16} cm^3. Thus doping the InP further n-type reduces the number of dopant atoms necessary to obtain an adequately conductive material versus using a p-type dopant to overcome the naturally n-type material. This is important since dopants and impurities in the InP increase the volumetric refractive index inhomogeneity scattering of the material, increasing the waveguide propagation loss [28].

It is important to point out here that the gallium and arsenic mole fractions of the InGaAsP waveguide core and cladding are very low - low enough that they may be considered as added impurities to an InP lattice. Although the composition of the material is technically InGaAsP, it still retains the physical and chemical properties of InP. The slight gallium and arsenic mole fractions are incorporated in the waveguide layers in order to provide the desired refractive index contrast and to incorporate very slight tensile strain ($\varepsilon < 0.05\%$). The material strain is calculated through experimentally devised formulas found in literature [29]. Since the released waveguides are not only an optical light guiding structure, but also a free-standing mechanical structure, the stress of the material becomes important. If a portion of the suspended waveguide that is fixed by tethers on two ends (fixed-fixed beam) exhibits compressive stress, the waveguide will buckle either up or down. For this reason it is important that the waveguide material be slightly tensile so that the waveguides remain flat.

Another reason to slightly dope the waveguide InP is that pure InP could not be obtained given our layer structure. The InGaAs layer grown directly beneath the InP layers has a high arsenic content, and the arsenic atoms used in the this growth have a

long residual period in the MBE chamber. This contaminates the subsequent material growth with a linearly decreasing arsenic composition. In InP, this arsenic contamination causes compressive stress, while gallium causes a more tensile material. For this reason, the InP waveguide layers incorporate gallium to increase the tensile stress and overcome the arsenic contamination.

Another challenge that arises from the arsenic contamination is a strain gradient in the material. Cantilever sections of the suspended waveguides that are supported on only one end will curl upwards if there is a strain gradient in the material, for example from arsenic contamination. Figure 2-12 shows several previously fabricated InP cantilever beams that exhibit this strain gradient [22]. This gradient cannot be easily compensated for through material design, so the mechanical design of our device must take this into account and cannot include long sections of waveguide suspended on only one end.

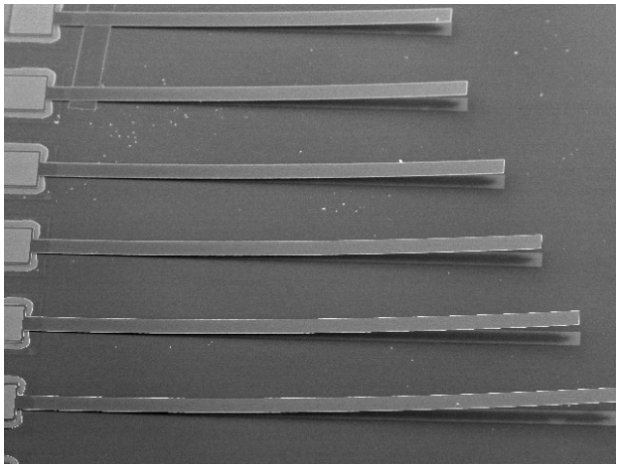

Figure 2-12: 800 μm to 1200 μm long InP cantilever beams exhibiting curl due to strain gradient as a result of arsenic contamination [22].

2.6 Summary of Suspended InP Waveguide Design

The design of free-standing, movable, suspended InP optical waveguides has been presented. The novel suspension mechanism and total release of the waveguides from the substrate is necessary due constraints of the InP material system. Both optical and mechanical characteristics of the waveguides have been taken into consideration. A finite-element model of the waveguide was created in the Optical Waveguide Mode Solver (OWMS) software package and a Matlab simulation was used to characterize the optical effects of the waveguide tether supports. The composition of the waveguide material was designed to induce slight tensile strain so that the suspended waveguides remain flat after release.

Chapter 3 – Fabrication of Suspended InP Waveguides

This chapter presents the fabrication of suspended InP waveguides. The growth of the initial material is performed in-house and important details are covered. A general overview of the fabrication sequence is then given, followed by a detailed description of each step. Finally, images and measurements of fabricated suspended waveguides are presented.

3.1 InP Suspended Waveguide Material

The underlying material used for fabrication of the suspended InP waveguides is an InP substrate with a single-crystal, multi-layer stack epitaxially grown on the top surface. The material parameters are given in Figure 3-1. All layers are grown using solid-source Molecular Beam Epitaxy (MBE) and are designed to be lattice matched or nearly lattice matched to the (100) InP substrate misoriented 4° toward (111). The InP substrate is semi-insulating while all subsequent layers are doped n-type, allowing electrostatic actuation of the waveguides to be employed. An n-type dopant, sulfur, was chosen because as-grown InP is naturally n-type with an electron concentration on the order of 10^{16} cm^3. In order to achieve a semi-insulating InP substrate, the purchased substrate was counter-doped with a p-type dopant during the crystal growth, in this case iron. Two layers that are shown here and not previously discussed are the InP buffer layer and the InP capping layer. The buffer layer is grown on the virgin InP substrate wafer to facilitate lattice matching of the grown layers to the substrate. The InP capping layer is 20 nm of highly doped InP to provide a good ohmic contact with metal layers deposited

to make electrical connections to the waveguides for actuation. Staff at the Laboratory for Physical Sciences (LPS) performed the MBE growth and subsequent material characterization.

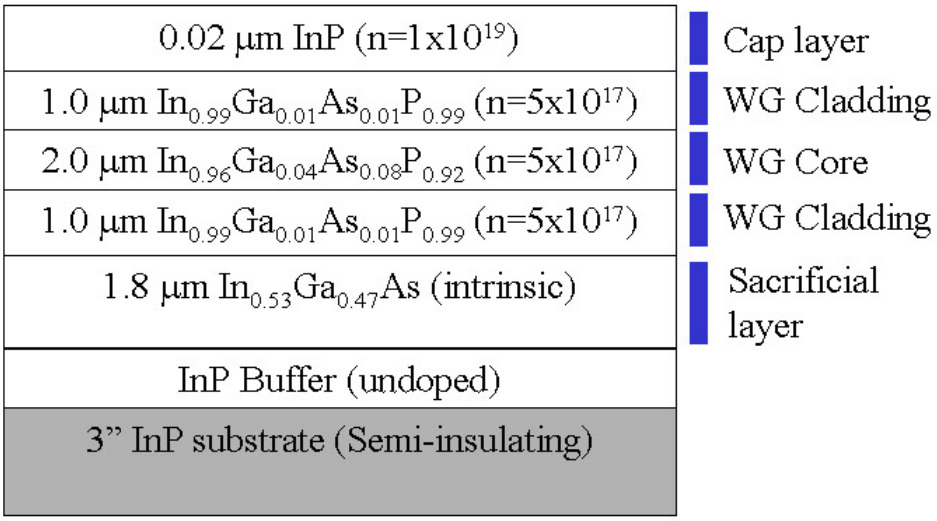

Figure 3-1: Molecular Beam Epitaxy (MBE) growth parameters for epitaxial layer growth.

The wafer growth was performed on a 2" substrate, which was cleaved into 7 chips for individual processing, each on the order of 12 x 12 mm. The device area used on each chip is 10 x 10 mm, so this provided the most efficient use of the material for development purposes.

3.2 Fabrication Process

Suspended InP waveguides are positioned to become a platform technology for the fabrication and design of InP waveguide MEMS. For this to be achieved, it is important that the fabrication process is simple, reliable, and extendable to complex devices. An overview of the developed fabrication process is given in this section, followed by a more detailed discussion of individual steps. All fabrication is performed in a class 10

cleanroom at the Laboratory for Physical Sciences (LPS) except for the supercritical dry, which is done in the MEMS Sensors and Actuators Lab (MSAL) at the University of Maryland, College Park.

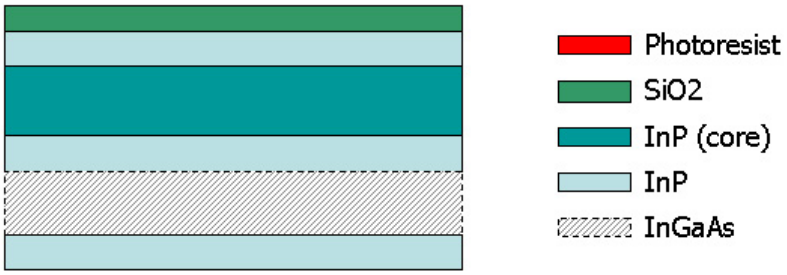

Figure 3-2: Fabrication step 1.

1) A 7000 Å SiO_2 masking layer is deposited via plasma enhanced chemical vapor deposition (PECVD). The oxide is used as a hard mask for etching of the underlying InP.

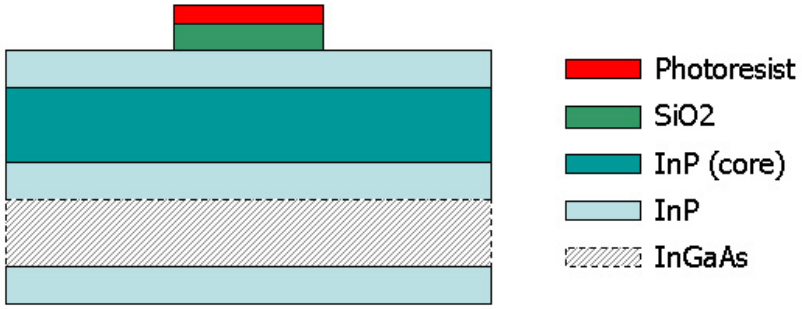

Figure 3-3: Fabrication steps 2-3.

2) The devices are patterned using a 5x optical stepper to expose 1 μm thick Arch OIR 906-10 positive photoresist to pattern the oxide hard mask. HMDS adhesion promoter is spun on beneath the resist. A focus/exposure matrix is processed prior to each exposure to determine the optimum exposure parameters. The resist is developed in Arch ODP 4262 developer.

Spin speed:	3000 rpm; 60 sec
Pre-bake:	90 ˚C hotplate; 60 sec
Exposure:	100-120 mJ·cm^{-2} / -1:1 focus
Post bake:	110 ˚C hotplate; 60 sec
Develop:	60 sec

3) The pattern is transferred into the SiO_2 hard-mask using a reactive ion etch (RIE) in CHF_3/O_2 plasma at 100W RF with a flow rate of 10 sccm CHF_3 and 3 sccm O_2. The resulting etch rate of the SiO_2 is 410 Å/min.

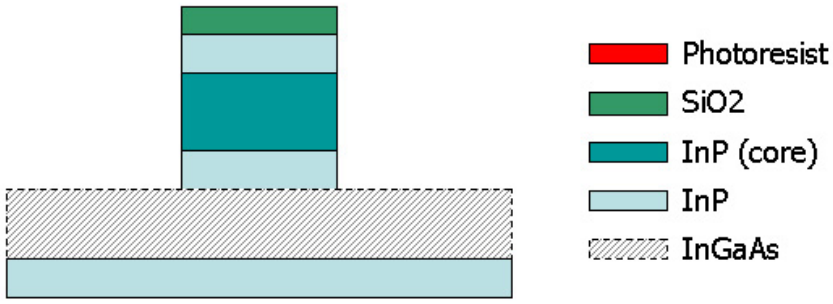

Figure 3-4: Fabrication steps 4-5.

4) Removal of all photoresist prior to the InP etch step is critical to a clean etch. To ensure photoresist removal, the chip is exposed to a 30-second O_2 plasma at 100W and 16 sccm O_2, a 30-second UV flood exposure, a 5-minute soak in Arch ODP 4262 developer, and finally a 5-minute soak in acetone.

5) To obtain highly-vertical, optical-quality sidewalls in InP, a multi-step RIE process was developed. After chamber conditioning, the first step of the process is a 5-minute InP etch using CH_4/H_2 plasma at 100W RF with 8 sccm CH_4 and 32 sccm H_2. The second step is removal of the polymer etch byproduct from the sidewalls in a 3-minute O_2 plasma at 100W and 16sccm. Each cycle results in an etch depth of 0.23 μm. This process is repeated to an

etch-depth of 5 μm to ensure the waveguide layers have been etched through. The details of this process are given in section 3.5.

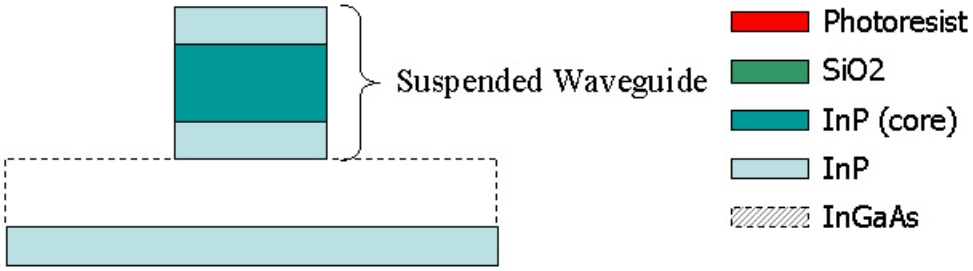

Figure 3-5: Fabrication steps 6-10.

6) The SiO_2 hard mask and polymer buildup from the InP etch are removed by a 1-minute O_2 plasma at 100W and 16 sccm followed by a 5-minute BOE (6:1) etch.

7) The chip is cleaved to expose the end facets of the waveguides. A micropositioner scribe tool is used to align the waveguides perpendicular to the cleave and align the cleave within 200 μm of the waveguide end to ensure tether supports at the ends of the waveguides.

8) The sacrificial InGaAs is removed in $HF:H_2O_2:H_2O$ (1:1:8). The lateral etch rate of the InGaAs is about 0.6 μm/min, resulting in a total release time of 6 minutes.

9) The released waveguides are immediately transferred to a beaker of de-ionized water (DIW) where they soak for 5 minutes. They are then immediately transferred to a solution of 75% DIW / 25% methanol for 5 minutes, then 50/50 DIW/methanol, 25/75 DIW/methanol, and finally the

waveguides are transferred to pure methanol. This process is used to ensure that the volume under the released waveguides is entirely displaced by methanol. It is important during this entire process that the chip is not allowed to dry or stiction could occur.

10) Finally, sublimation in supercritical CO_2 is used to dry the waveguides and prevent stiction to the substrate.

3.3 Projection Lithography

In order to achieve optimum sidewall roughness and angle and the best possible feature resolution, projection lithography was used to pattern the suspended waveguides. A 5X reduction Alphastep 1000 was used to achieve critical dimensions down to 0.5 μm. This is an important asset to our fabrication and testing because the width of the waveguide tethers has a strong influence on the tether loss. Having the capability to fabricate features down to 0.5 μm can reduce the total loss of the suspended InP waveguides. A 5" chrome on quartz mask with a 5 cm x 5 cm mask area and a 0.1 μm spot size was used. This 25 cm^2 mask area was stepped down to a 100 mm^2 area on the chip. Arch OIR 906-10 photoresist was spun on the chip to a thickness of 1 μm at 3000 rpm for 60 seconds with an adhesion layer of HMDS spun on at 3000 rpm as well. The adhesion promoter was necessary since SiO_2 was used as the hard mask. Before exposure, the resist is pre-baked for 60 seconds on a 90 °C hotplate. The exposure time and focus depth of the stepper optics varied from run to run due to drift in the stepper system. Both parameters were determined before every exposure using a focus-exposure

matrix on a test InP/SiO_2 chip. After exposure and a 60 second post bake on a 110 °C hotplate, 60 seconds in Arch ODP 4262 developer is used to develop the pattern.

The Alphastep stepper at LPS provided many challenges to our work: auto leveling of wafer pieces cannot be implemented on this stepper and the lamp intensity can fluctuate over periods of only a couple hours. In order to level the wafer pieces, we employed a technique of shimming the chuck using various pieces of aluminum foil and Post-It™ notes. A program is run to measure the wafer height across the chip using the stepper's laser measurement system, then the chuck is shimmed to try and level the surface. The focal depth of the stepper optics is 2 μm, so this process is repeated until the die to die variation in height is less than 1 μm. In our case, a single 10x10 mm die per chip was used so the entire chip area had to be leveled to +/- 1 μm to achieve optimum resolution. In order to provide the correct exposure time and focus depth, a focus-exposure matrix was used prior to exposing each chip. A mask with a test pattern of bars and spaces varying from 2.0 μm down to 0.5 μm in width was used for this matrix. An exposure dose between 100 – 120 $mJ \cdot cm^{-2}$ with a focus depth between –1 and 1 provided the best feature resolutions and resist profiles.

3.4 InP Etch Development

For optoelectronics, sidewall quality is one of the defining characteristics for optical loss. In tightly-confined waveguides such as our ridge structure, interface scattering loss at the sidewall is predicted to dominate other loss mechanisms [28]. Interface induced scattering is proportional to $E^2(n_2^2-n_1^2)$ and A^2 where A is the r.m.s roughness of the waveguide sidewalls. Thus, one of the greatest contributing factors to sidewall scattering

loss is the roughness of the waveguide. For this reason, a great deal of characterization and optimization went into the development of the InP sidewall etch process.

The process of dry-etching InP using various halogen based chemistries such as $SiCl_4$ and Cl_2 is commonly used, however these chemistries are unacceptable for optoelectronics processing due to the high damage and surface roughness caused. As an alternative, using a methane-hydrogen-argon chemistry [30,31] to etch InP results in sidewall roughness 15-20 times less than halogen based etches [32]. The highest etch rate and most vertical sidewall profile are reported to occur around a concentration of 1:5 CH_4:H_2. Lower concentrations of methane result in a reduced etch rate due to reactive species depletion, while higher concentrations lead to a reduced etch rate caused by excessive byproduct surface deposits. We believe it is possible that the excess surface deposits also lead to an increase sidewall verticality due to the in-situ passivisation.

We used a Plasmatherm 790 Reactive Ion Etcher with an aluminum oxide bottom plate for our process. InP etching has previously been studied in this system at LPS [33]. Optimum results were reported by using a multi-step etch process with a Ti/SiO_2 bi-layer hard mask. The etch process involves repeated cycles - each cycle consists of a 5 minute CH_4/H_2/Ar etch step followed by a 3 minute O_2 polymer removal step. The etch step is extremely directional and involves a chemical etch of the InP via a 1:4 ratio of methane and hydrogen respectively as well as a physical milling etch caused by the heavy argon ions. The chemical etching of InP produces a carbon-based byproduct that is redeposited on the substrate and sidewalls of the InP [32]. The oxygen plasma step is used to remove this buildup so that etching can proceed. The net result of this etch is very similar to a

Deep Reactive Ion Etch (DRIE) – excellent verticality and sidewall roughness can be attained due to the in-situ passivisation of the sidewalls during the etch process.

When this etch recipe was employed for our fabrication of InP waveguides, we encountered several unexpected problems. During the process, an extremely dense nano-grass formed, covering the substrate. The nano-grass quickly became so dense that etching could no longer proceed. Figure 3-6 shows an SEM of the nano-grass. Figure 3-7 shows optical microscope photographs of an InP substrate before and after the formation of dense nano-grass during InP etching. This nano-grass is a side effect of the passivisation by the etch byproducts. In a normal RIE etch process, if a small particle lies on the substrate, it will mask the area beneath and a small column will begin to form. Any plasma that attacks this column from an angle, however, will quickly undercut it and etching will proceed. In our process, we believe that the sidewalls of the column formed are passivated with the polymer byproduct, protecting the column from lateral undercut. Small particles of this polymer are then sputtered off and re-deposited close-by, forming more columns. As a result, a very dense nano-grass forms covering the substrate.

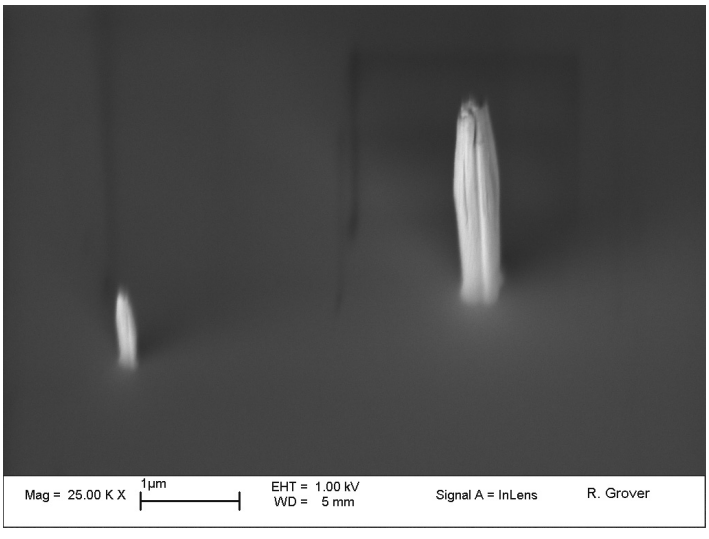

Figure 3-6: SEM image of two nano-grass structures formed during reactive ion etching of InP.

Figure 3-7: Optical micrograph of the formation of dense nano grass. The unetched InP substrate (left) shows no sign of grass, while the substrate after 10 cycles of RIE etching (right) has formed dense grass (the black region) on the unmasked InP substrate.

We theorized that sputtering of the Ti masking layer by the argon ions could be causing this nano-grass to form. The Ti layer above the SiO_2 helps to prevent edge erosion of the SiO_2 mask, but using an oxide thickness of greater than 5000 Å proved sufficient to prevent the edge erosion from being transferred into the InP. Using only a SiO_2 hard mask relieved the problem slightly, but after about 0.5 μm of etching the nano-grass still began to form. We found that, by removing the heavy argon ions from the etch process, etch depths of over 1 μm could be obtained with no formation of nano-grass. Using only a methane-hydrogen chemistry, we have now optimized our etch process to prevent the formation of nano-grass during normal etching with no decrease in sidewall verticality after the removal of argon. This grass cannot be prevented if it occurs due to contamination within the chamber, however. By careful prevention of chamber contamination, we can repeatably etch InP to up to 5.4 μm, more than sufficient for fabrication of suspended InP waveguides.

Unless strict RIE chamber contamination control is employed, the formation of dense nano-grass is still a severe problem. There are two likely causes of this nano-grass formation. The first is external contamination. The Plasmatherm 790 RIE system is used

by many research groups at LPS for a variety of materials. Photoresist, BCB, and other polymers are etched and these materials can be redeposited on the walls of the RIE chamber. We especially found that it was difficult to obtain clean InP etch results after the chamber had been used for BCB etching. The issue of chamber contamination was resolved by including an extensive cleaning process before our InP etch. First, the chamber walls and shower head are wiped down using isopropyl alcohol. Next, we run a 4-hour oxygen plasma cleaning process followed by 30 cycles of the InP etch. This process is run overnight so that we can begin etching in the morning. Another source of external contamination during the InP etch is any photoresist residue on the chip from the hard mask patterning. To remove all traces of photoresist, the aggressive resist stripping procedure described in the fabrication process is used.

If these preliminary cleaning steps are followed, up to 1 μm of InP can be etched without any formation of nano-grass. After this etch depth, however, we began to observe slight formation of nano-grass. Chamber vacuum is maintained throughout the etch cycles, so this contamination must be due to internal sources. Sputtering and redeposition of the etch byproduct polymer onto the chip and RIE chamber is the most likely source of internal contamination. To resolve this problem, we remove the InP chip from the RIE and initiate a shortened version of the chamber clean after every 1 μm of InP etch. The chamber clean includes 30 minutes of O_2 plasma clean followed by 3 cycles of the InP etch.

Although some of the chamber preparation and cleaning times may be excessive, by following this procedure repeatable etch depths of over 5 μm can be obtained while maintaining consistent etch rate and smooth, highly vertical optical-quality sidewalls. In

the future, the RIE chamber cleaning times could be gradually reduced to shorten the time required for the process.

Another problem encountered during the etch development is micro-loading. Micro-loading is a commonly encountered problem in RIE etching - small enclosed trenches and areas etch at a lower rate than large open areas [34]. This is due to the limited transport of reactant species and byproducts from enclosed areas. Figure 3-8 to Figure 3-10 show several examples of micro-loading. These devices were etched 4.5 μm deep in the open areas, exposing the sacrificial layer below the top 4 μm of InP. In trenches less than 5 μm wide the InP was not entirely etched through, however. To overcome this micro-loading, subsequent devices were etched to a depth of 5.4 μm. This ensured that all InP was removed from the trenches and enclosed areas. In the layout used for these waveguides, the smallest spacing included was 5 μm. This effect should be taken into account for the design of future devices since spacing less than 5 μm will require even longer over-etches to remove all InP.

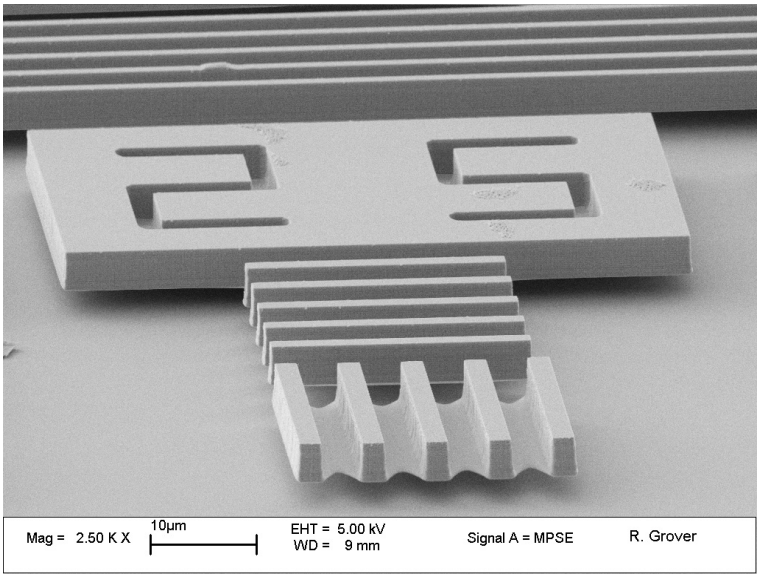

Figure 3-8: SEM showing unetched InP due to micro-loading within trenches. The spacing of these sacrificial etch test bars is 2.5 μm.

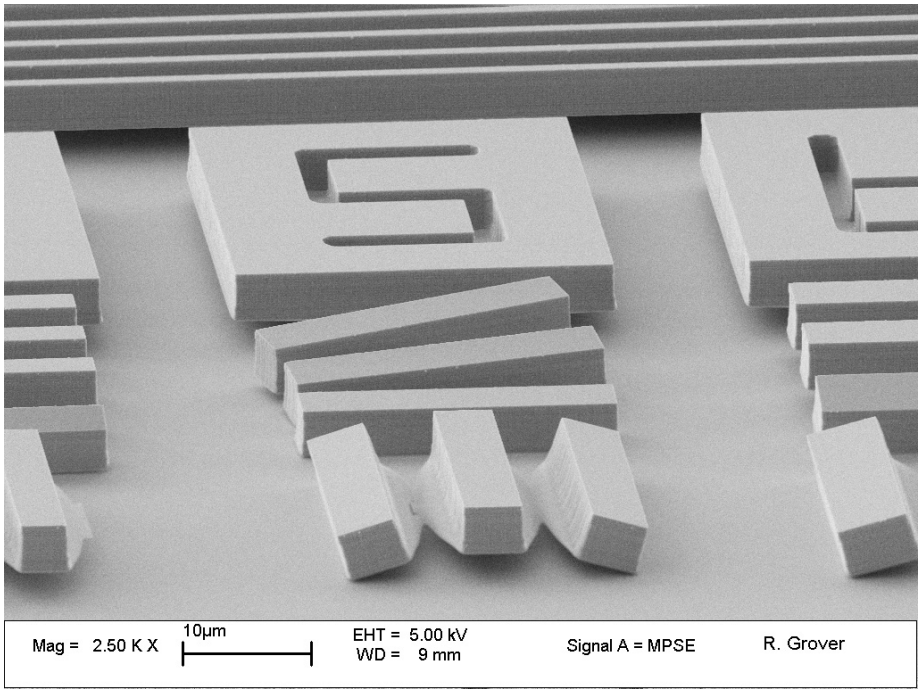

Figure 3-9: SEM showing more results of micro-loading. Notice that these sacrificial etch test bars have a larger spacing (5 µm) and the InP is almost removed.

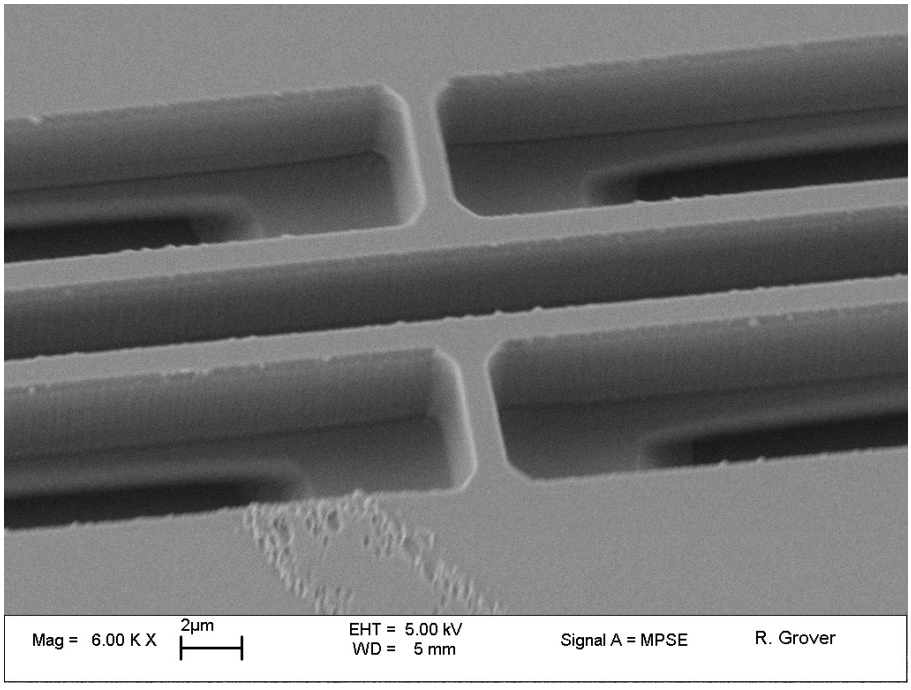

Figure 3-10: SEM showing 5 µm trench on the sides of two suspended InP waveguides. The InP was not entirely removed due to micro-loading.

3.5 InP Etch Process

The final InP RIE etch process we developed is as follows. First, an overnight RIE chamber cleaning process is run. The chamber clean consists of a 180 minutes of O_2 plasma at 300W RF power and 16 sccm O_2 followed by 30 cycles of the InP etch process. Before etching, the wafer undergoes an extensive clean to remove any photoresist residue along with any other contaminants. The wafer clean involves a 30-second O2 plasma at 100W RF and 16 sccm O2, a 20-second UV flood exposure, 5-minutes in Arch ODP 4262 developer, a 5-minute acetone soak, and finally a standard clean in acetone/methanol/isopropanol. The chip is then loaded into the RIE chamber and cleaned with 3 minutes of O2 plasma before running 5 InP etch cycles. The pre-etch oxygen treatment consists of 16 sccm O_2 at 100W. Each InP etch cycle includes 5 minutes of 8 sccm CH_4/32 sccm H_2 etch at 100W RF power and 3 minutes of 16 sccm O_2 cleaning at 100W RF power. Each etch cycle removes an average of 0.23 μm of InP, resulting in 1.15 μm etch depth per 5 cycles. After every 5 cycles, the wafer is removed and an abbreviated chamber clean is run. The abbreviated chamber clean retains the same parameters as above, but only 30 minutes of O_2 plasma and 3 cycles of InP etch are included. This process is repeated until the desired etch depth is reached. In our case we found that a 5.4 μm etch depth was sufficient to remove the InP from all the 5 μm-wide trenches and enclosed areas in the devices.

Figure 3-11 shows the results of the InP etch. With the use of a scanning electron microscope (SEM), we measured the sidewall parameters resulting from this etch. A sidewall roughness of less than 50 nm was achieved, which is approximately 1/10 of the wavelength in the waveguide (1.55 μm / effective optical index = 0.49 μm) (Figure 3-12).

The angle of the sidewall was determined to be better than 89° (Figure 3-13). Mask erosion of the SiO_2 was limited to the upper half of the oxide and therefore did not transfer into the InP (Figure 3-14). InP to SiO_2 mask selectivity was measured to be better than 50:1.

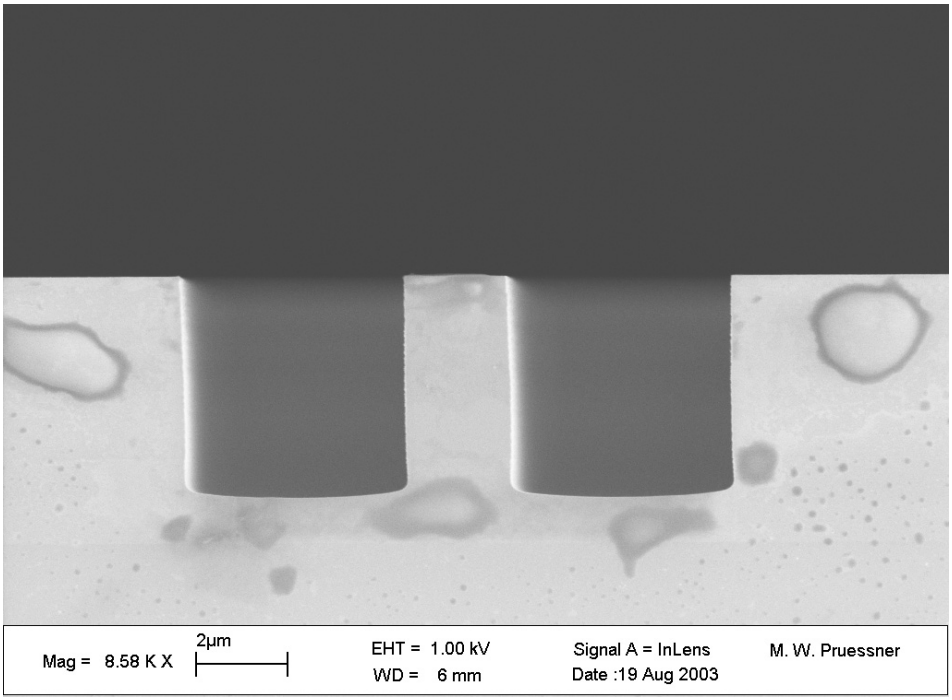

Figure 3-11: SEM of cross-section of InP etch showing vertical 5.4 µm deep, optical quality sidewalls.

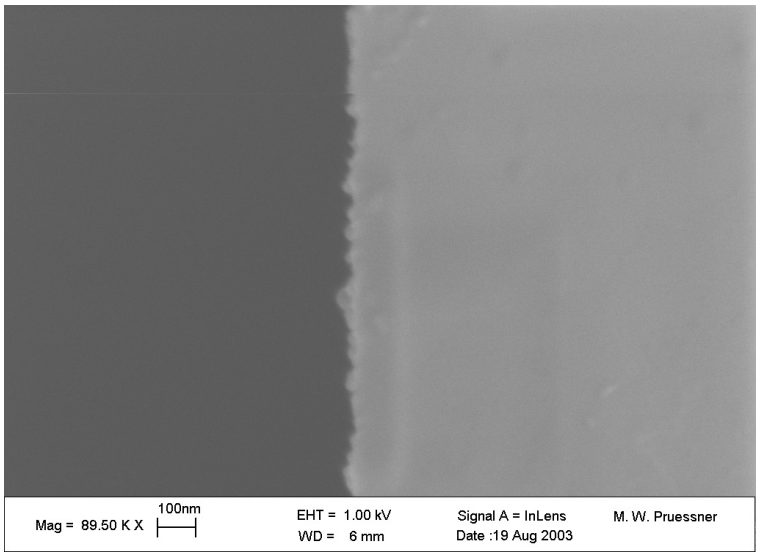

Figure 3-12: SEM of cleaved InP sidewall with less than 50nm sidewall roughness.

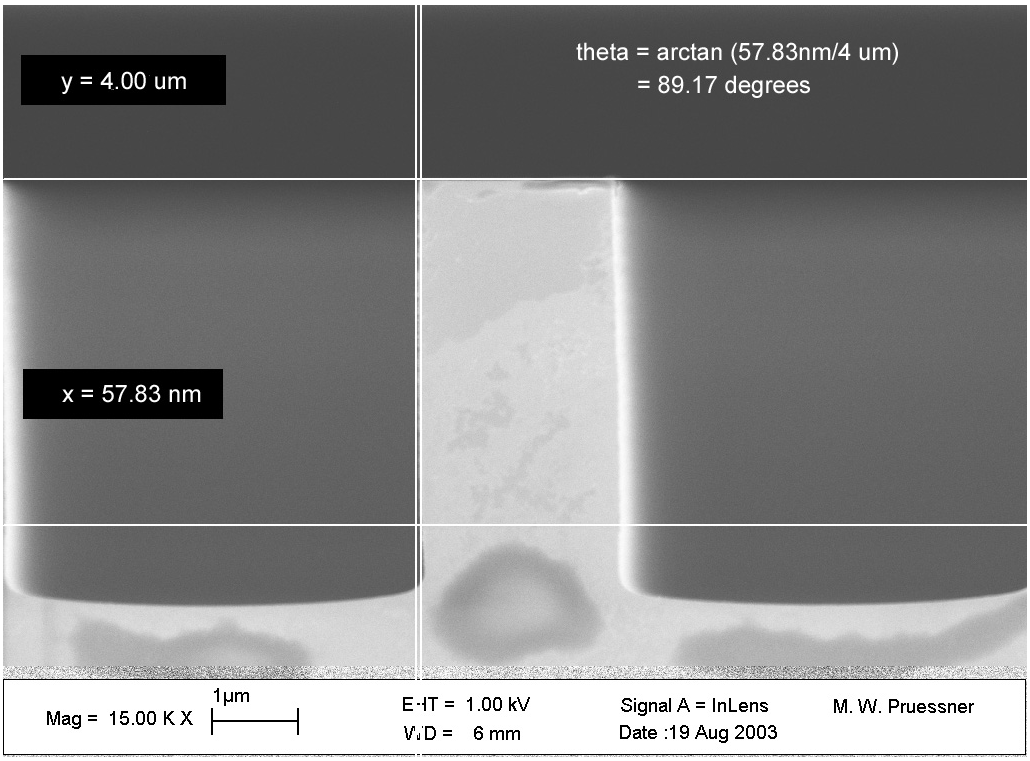

Figure 3-13: SEM measurements of sidewall angle for InP etch.

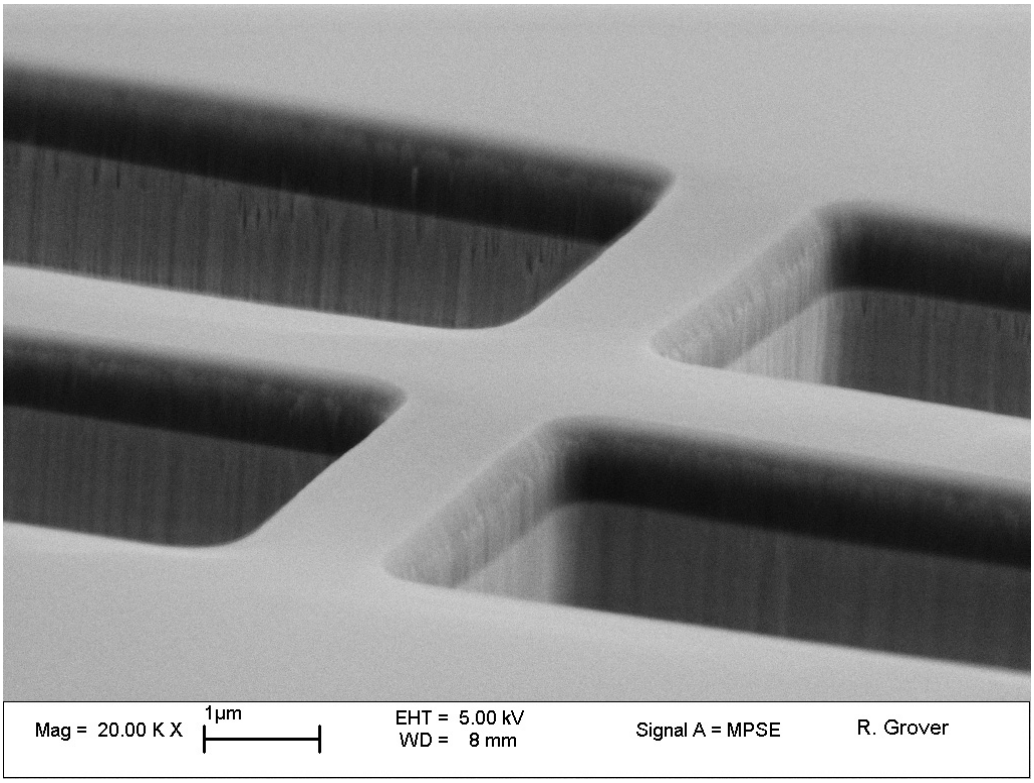

Figure 3-14: SiO_2 hard-mask after 5.4 µm InP etch. Only the top half of the oxide shows edge erosion, which prevented this roughness from being transferred into the InP.

3.6 End Facet Cleave

The two main categories of loss through a waveguide are waveguide propagation loss and insertion loss. Internal waveguide propagation loss can be minimized by design considerations and high quality fabrication as discussed in the InP etching section. To minimize insertion loss, it is important to have a perfectly smooth facet to focus light into the waveguide and to extract it at the other side via optics or fibers. Cleaving is a common technique for exposing perfectly smooth facets and can be employed only on single-crystal substrates and waveguides. As long as the waveguides are fabricated perpendicular to the major or minor axis of the crystal, a small crack in the substrate lattice introduced at the edge of the substrate will propagate along the crystal axis, revealing an atomically flat edge.

In the fabrication of traditional semiconductor waveguides, cleaving of the end facets is the final step. By the end of our process, however, the suspended waveguides are no longer a solid crystal since the sacrificial layer has been removed, dictating that the chips be cleaved just prior to the sacrificial release. This does not present any particular challenges, but great care must be taken not to contact anything with the cleaved edges of the chip during the release and critical dry. Any scratches or blemishes on the cleaved facet can dramatically increase the waveguide insertion loss due to roughness-induced reflection and scattering. Another challenge unique to these suspended waveguides is that the cleaved end facets of the waveguides must be within approximately 100 to 200 μm of a tether. Since the end of the waveguide is effectively a cantilever beam, the strain gradient introduced by arsenic contamination during growth will cause the end facets to curl upwards. As the angle of the end facet increases, the amount of light coupled into

the waveguide will be reduced. To solve this, the design of each waveguide includes a "cleaving zone" at both ends. Within this cleaving zone, the tethers are spaced only 75 μm apart, meaning that as long as the waveguides are cleaved inside the cleaving zone the ends will not curl up measurably. This length was determined based on our previous mechanical studies of InP cantilever beams epitaxially grown over an InGaAs sacrificial layer [22]. In our case, the width of each cleaving zone is 200 μm, which is adequate provided a precision scribing tool is used.

To cleave the waveguide facets, we begin by mounting the chip in a precision scribing tool. The tool consists of a diamond-tipped scribe mounted beneath an angled microscope objective. A vacuum chuck is used to hold the chip in place and micropositioners on the chuck are used to position the chip. The waveguides are aligned and an approximately 2 mm long scribe is made on both ends of the waveguides within the designed cleaving zones. Next, the chip is positioned above a razor blade and the blade is aligned with the scribe mark using a microscope objective. Pressing down gently on both sides of the chip will propagate the scribe mark along the crystal axis, exposing an atomically flat end facet for the waveguides.

3.7 Sacrificial Etch

The next to last step in fabrication of suspended InP waveguides is release of the waveguides by removing the InGaAs sacrificial layer. A 100% selective etch between InP and InGaAs is accomplished using a mixture of $HF:H_2O_2:H_2O$ (1:1:8) [35]. Although almost any acid can be used in this reaction, HF is used since we found it to be slightly more isotropic than other acids when used to etch InGaAs.

The chip was submerged in the etch solution at room temperature for 1-minute intervals until the sacrificial etch bars of the desired thickness had been removed. These etch bars are used to indicate and measure the lateral etch rate by observing the maximum width of etch bar that has been entirely undercut. We measured a lateral etch rate of 0.6 μm per minute. Figure 3-15 shows the sacrificial etch bars after 5 minutes of etching. A total of 6 minutes was required to release the waveguides entirely. SEM images of our final fabricated devices show that the waveguide layers are not attacked by the sacrificial etch (Figure 3-16). This shows that, as predicted, the waveguide layers behave chemically as InP, even with the slight mole fractions of gallium and arsenic included.

Figure 3-15: Optical micrograph showing sacrificial etch bars released up to 6 μm wide after 5 minutes of etching.

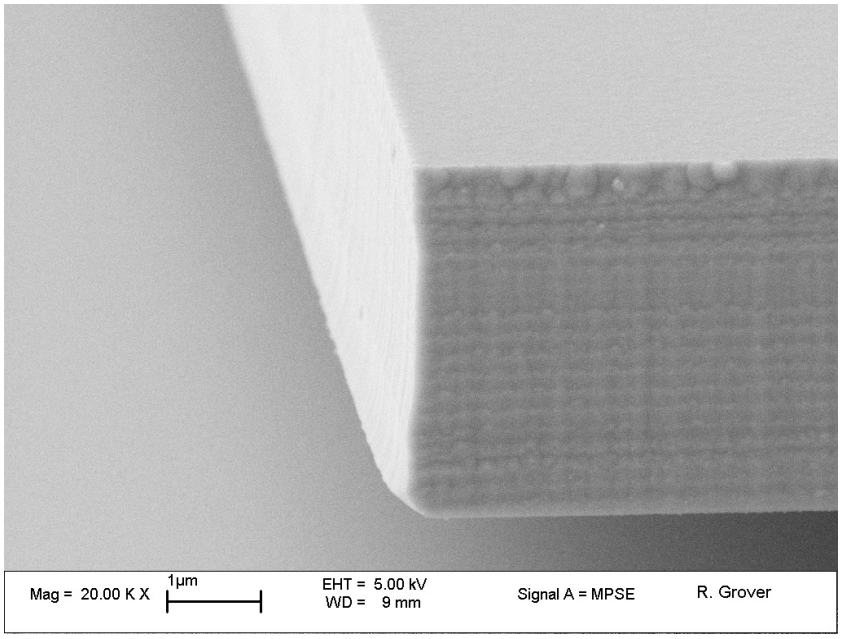

Figure 3-16: Close-up of SEM of released InP waveguide showing unetched InP waveguide layers.

3.8 Supercritical Drying

Stiction is a common and well-known problem with reliability and yield of MEMS devices. Stiction can occur either during device actuation, or during drying of a released device after the sacrificial etch. In our case, we are concerned with stiction that can occur during post-release drying of the suspended waveguides [35,36]. After release, the waveguides are surrounded by fluid. As the fluid evaporates, the surface tension can cause the suspended waveguide to be pulled toward the substrate. As a result, the waveguide can come in contact with the substrate, at which point van-der-Waals forces take over. These forces are extremely strong on the atomic scale and the end effect is that the waveguide will be permanently stuck to the substrate beneath it. This stiction is not an issue for devices with a large gap between the released device and the substrate, but because the suspended sections of the waveguide are up to 2.5 mm in length, they are compliant and even the 1.8 µm gap to the substrate may not be enough to prevent stiction

from occurring. Although this presents a challenge, there are well-established means to overcome stiction.

One method is to use supercritical drying. Supercritical drying takes advantage of the critical point in a state diagram of a fluid such as CO_2 (Figure 3-17). Liquid CO_2 is used to displace the methanol surrounding the released device. Next, the pressure and temperature of the CO_2 are increased past the critical point then the pressure is decreased while the temperature is held constant. This allows the liquid to sublimate, transforming directly from liquid to gas, which has useful anti-stiction properties. Because the densities of the liquid and gas phases of a supercritical fluid are equal, there is no interface between the phases of the fluid and no surface tension. Using this type of fluid is a novel way to prevent surface tension from bringing two surfaces together when it evaporates. CO_2 is commonly used for supercritical drying since the temperatures and pressures involved in its sublimation are readily attainable: the critical temperature, Tc, is 31.1 ºC and the critical pressure, Pc, is 72.8 atm.

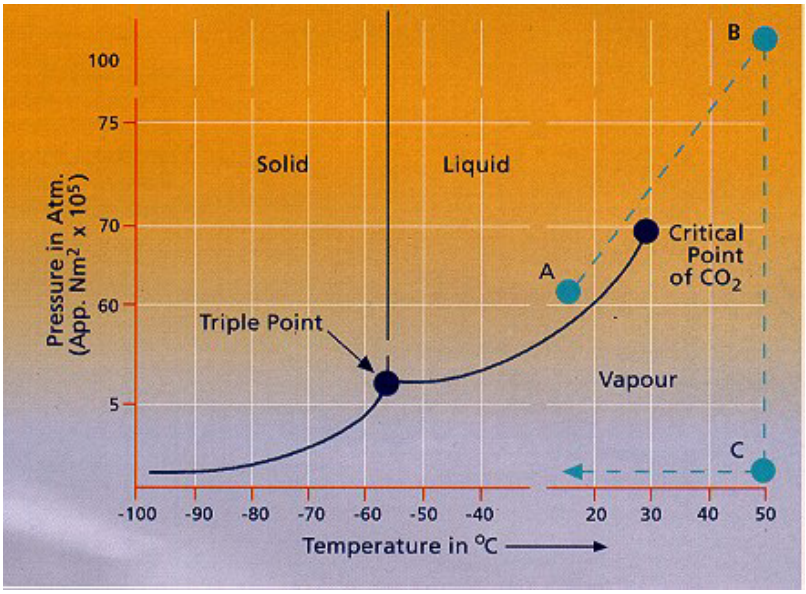

Figure 3-17: Phase diagram of CO_2 showing pressure-temperature route of critical drying (A-B-C) [37].

For our process, we used a Tousimis Samdri-795 CO_2 Supercritical Dryer. The tool is hooked up to a tank of ultra-pure liquid CO_2 for both cooling and as the supercritical fluid. The sample must first be entirely submersed in methanol as described in step 9 of the fabrication procedure in section 3.2. It is important that all water is replaced by the methanol since water would freeze when the liquid CO_2 is introduced to the sample. The chamber of the Samdri supercritical drying tool is only large enough for chips approximately 2 cm x 2 cm, but that is more than sufficient for our devices. Using this tool, we were able to reliably and repeatedly dry our released waveguides without observing any stiction to the substrate, even for suspended waveguide lengths up to 2.5 mm.

3.9 Fabrication Results

After supercritical drying of the devices, we inspected the suspended waveguides using a scanning electron microscope (SEM). The measurements of the fabricated devices are very close to the original specifications in the design. Figure 3-18 – Figure 3-20 show the final suspended waveguides. The waveguide facet in Figure 3-18 shows the extremely smooth surface exposed by the cleave and also highlights the selectivity of the sacrificial etch. Even with the slight mole fractions of gallium and arsenic in the InP waveguides, the material was not attacked by the $HF:H_20_2:H_20$. Figure 3-19 shows a released cantilever beam with the same dimensions as the waveguides. The beam is 200 μm long and displays slight vertical deflection due to arsenic contamination. The short 30 μm beam in Figure 3-20 displays no measurable deflections, showing that even with the arsenic contamination during growth causing a slight strain gradient, short cantilever

sections of the waveguide remain flat. Furthermore, sections of suspended waveguide up to 2.5 mm long remain perfectly flat with no buckling, demonstrating that the material does exhibit slight tensile stress, as designed.

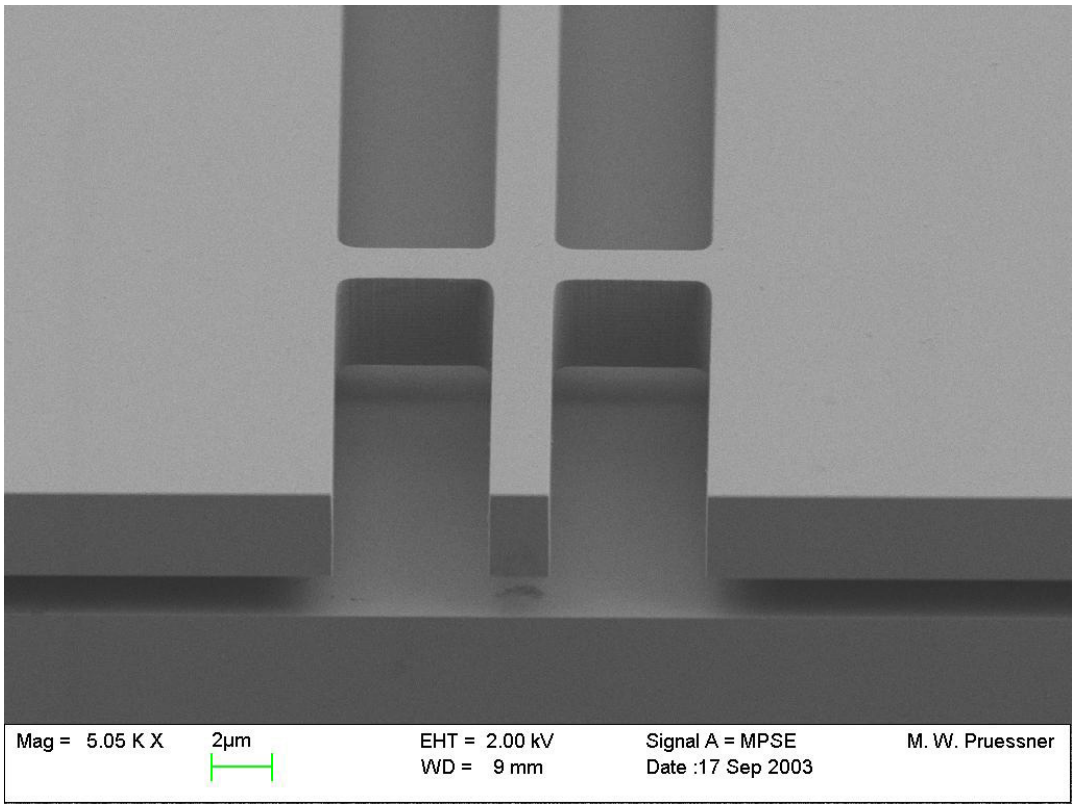

Figure 3-18: SEM of suspended InP waveguide showing cleaved end facet and a pair of tethers.

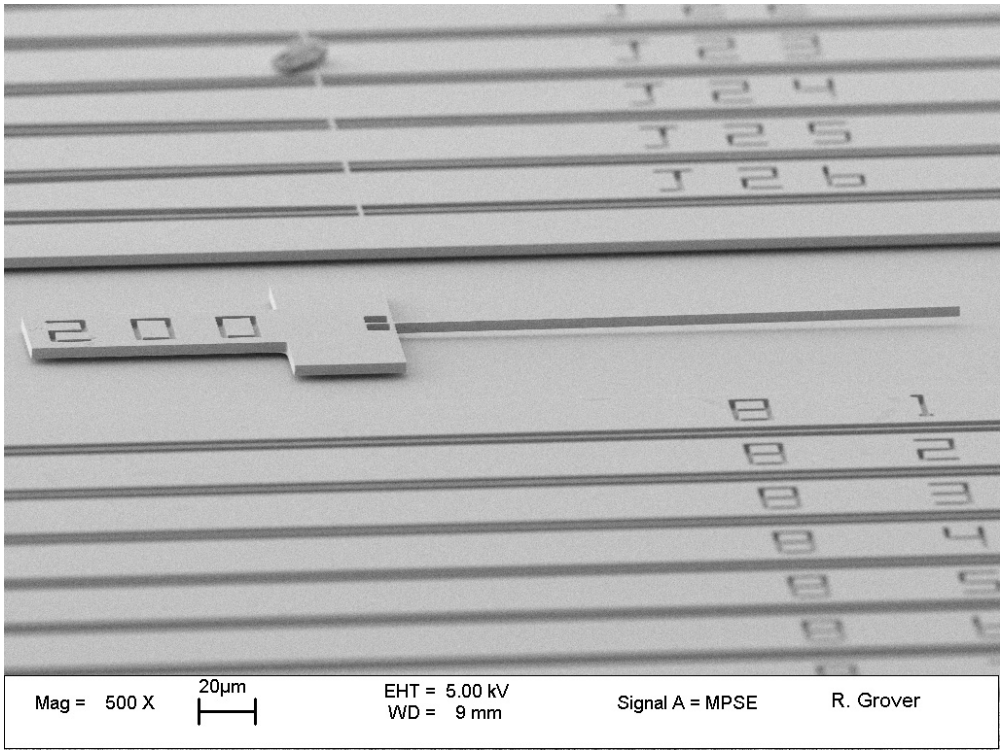

Figure 3-19: SEM of 200 µm long cantilever beam with dimensions identical to the waveguides.

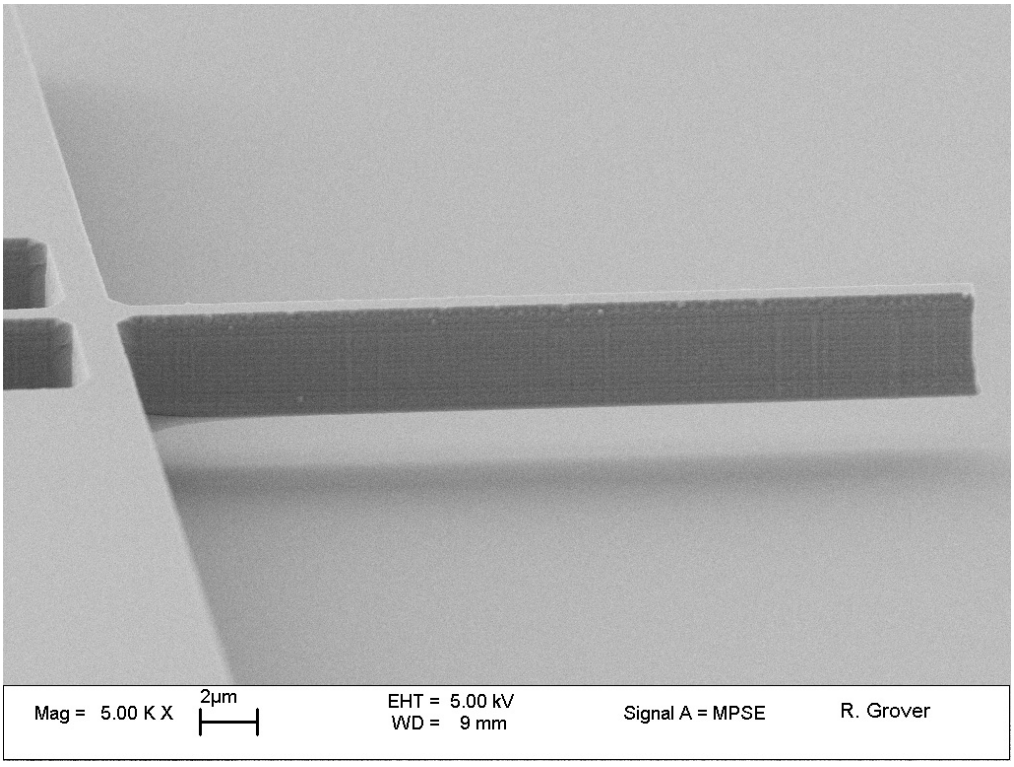

Figure 3-20: SEM of 30 µm long cantilever waveguide with no measurable vertical deflection.

One problem encountered with the fabricated devices is some rounding of concave corners at each tether as is shown in Figure 3-21 from a top-down view.

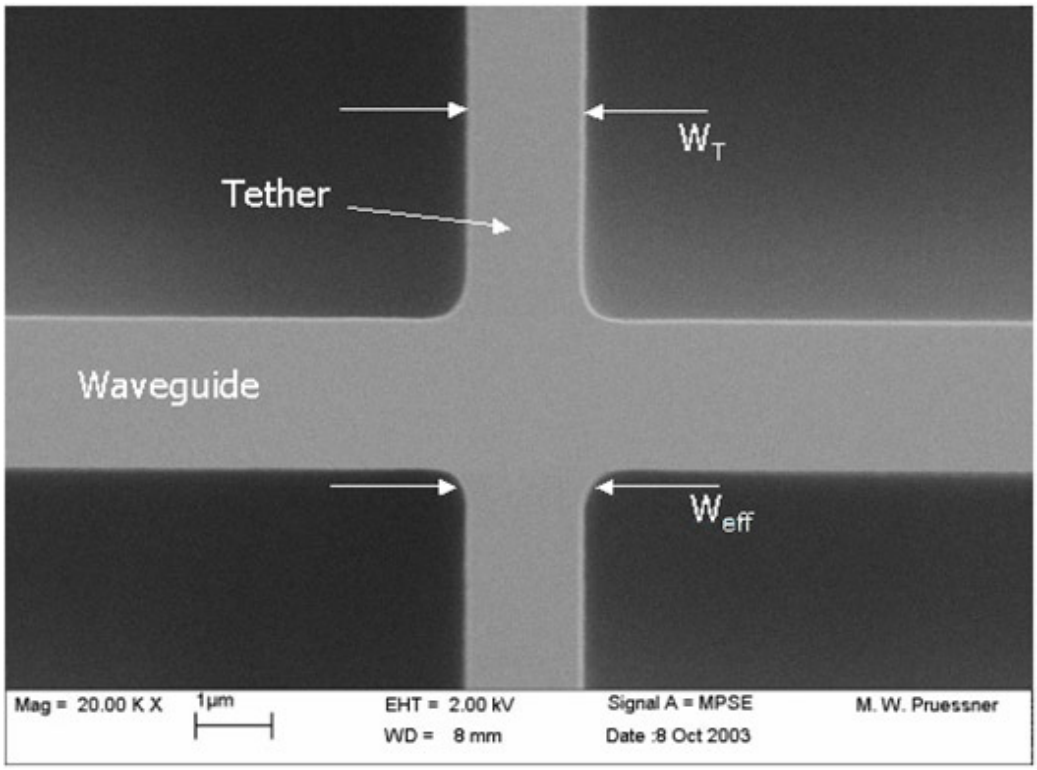

Figure 3-21: Top-view SEM showing waveguide and tether pair with rounded concave corners. This results in a larger "effective" tether width than designed. W_T = designed tether width; W_{eff} = effective tether width due to corner rounding.

The rounding of concave corners is due partially to photoresist processing limitations and partially due to diffraction during lithography once the features fall below the resolution of the optical system. While this rounding was optimized, it could not be entirely eliminated using the current fabrication equipment. The consequence of these rounded corners is to produce an effective tether width that is larger than the designed width. From SEM measurements, we found that the effective tether width is about 0.5 µm larger than the designed width. The problem with this larger effective tether width is that, from

the perspective of the optical mode propagating through the waveguide, the tethers become about 0.5 μm wider. As a result, the beam radius from equation 2.1becomes:

$$W_{eff} = W_T + 0.5\,\mu m \tag{3.1a}$$

$$w^2(W_{eff}) = \frac{\lambda}{\pi n}\left[\frac{W_{eff}^{\ 2} + (\frac{\pi n w_0^{\ 2}}{\lambda})^2}{\frac{\pi n w_0^{\ 2}}{\lambda}}\right] \tag{3.1b}$$

w_0 = beam waist; W_{eff} = effective tether width; W_T = designed tether width

The fractional optical loss per tether becomes:

$$Loss = \left[\frac{y_{wg}\, w(W_{eff}) - y_{wg}\, w_0}{w_0\, w(W_{eff})}\right] \tag{3.2}$$

y_{wg} = height of the optical beam; $w(W_{eff})$ = beam radius after the effective tether width; w_o = beam waist

This results in a larger optical loss per tether. To some extent, the design of the waveguide can compensate for this rounding of corners by incorporating a narrower tether. We have demonstrated tether widths down to 0.5 μm, so 1.0 um is the minimum possible effective tether width for our suspended InP waveguides using this fabrication process and equipment.

3.10 Summary of Fabrication Results

A single-mask process for the fabrication of suspended InP waveguides has been developed and optimized. The process uses optical projection lithography to obtain good photoresist profiles at a resolution down to 0.5 μm. We optimized a RIE process for etching InP using a SiO_2 hard mask. This etch results in etch profiles up to 5.4 μm deep with better than 89° verticality and sidewall roughness less than 50 nm. The sacrificial etch used is 100% selective and releases all suspended waveguides up to 2 μm wide in a 6 minute etch. We implemented a supercritical drying procedure in CO_2 and did not observe any stiction of the waveguides to the substrate. The resulting suspended InP waveguides are mechanically robust and we did not observe any broken or defective waveguides or tethers. The fabrication process developed was designed to be simple so that suspended InP waveguides can be utilized as a basic component in the design of more complex InP waveguide MEMS systems.

Chapter 4 – Optical Waveguide Characterization

This chapter describes the optical characterization of the waveguides. The experimental apparatus and procedures are given, followed by the results and analysis of the characterization. A table of the measured parameters is presented for use is future design work.

4.1 Characterization Goals

The purpose of this research is to design and characterize suspended waveguides as an enabling technology for InP waveguide MEMS. So far, the purpose and concept of suspended InP waveguides has been introduced and their design and fabrication developed. The design is flexible to allow for any length of waveguide, number of tethers, and bends or routing of the waveguides. The fabrication of the waveguides is simple and involves only a single lithography step with three etch steps. This simple fabrication process facilitates incorporation of InP suspended waveguides into a more complex design. The final stage of this research is to optically characterize the waveguides. In designing and laying out an InP optical waveguide MEMS system, it is important to know the optical loss of the waveguides as well as the allowable tether spacing to plan where to incorporate tethers.

Due to the lateral tether suspensions and lack of a substrate beneath the lower cladding, suspended InP waveguides are a unique and new technology. As such, it is important to characterize them for use in the design and construction of InP optical

MEMS systems. This chapter focuses on the optical characterization of InP suspended waveguides. The key parameters to be determined are listed in Table 4-1.

Property	Primary Parameters	Units
Waveguide Loss	Waveguide material, Sidewall roughness	dB/cm
Tether Loss	Tether width, Waveguide width	dB/tether
Maximum Tether Spacing	Material stress	mm

Table 4-1: Key InP suspended waveguide design parameters.

Waveguide loss is a measurement of the signal attenuation per unit length of the waveguide. Waveguide propagation loss can be broken down into several components [28]:

$$Lt = L\alpha + Lss + Lvs + Lc + Lins \tag{4.1}$$

L*t*: total loss
L*a:* absorption loss
L*ss*: interface induced scattering
L*vs*: volumetric refractive index inhomogeneity scattering
L*c*: coupling of guided modes to substrate modes
L*ins*: insertion loss

In our case, the coupling of guided modes into the substrate can be ignored, however we have to add the effect of tether loss. Tether loss is a measurement of the optical power attenuation induced by each tether. This is mainly a function of waveguide width and tether width, which in turn is dependant on design and fabrication tolerances. Tether spacing is the distance between tethers. The greater the tether spacing, the fewer number of tethers that are required for a given suspended waveguide. As tether spacing increases, however, mechanical issues come into play such as stiction to the substrate and reliability and yield of the waveguide.

This chapter will present the experimental setup used for measurements, the theory and methods used for testing, the results of relative power and Fabry-Perot contrast measurements, and a summary of the as-fabricated characteristics of the suspended InP waveguides. Once these parameters have been measured and characterized, the necessary information will be available for the design and fabrication of complete InP waveguide MEMS systems based on suspended waveguide technology.

4.2 Experimental Setup

After the design work, establishing and modifying the fabrication process, and creating suspended InP waveguides have been completed, it is important to have a reliable and repeatable testing and measurement apparatus. In testing optical waveguides, it is necessary to couple optical power into the waveguide and extract the output power at the far end. The losses induced by misalignment, mode mismatch, reflection, and scattering of the optical power being coupled into and out of a waveguide are lumped into one parameter: insertion loss. One particular challenge in testing optical waveguides is obtaining a repeatable insertion loss.

There are several common methods to overcome this problem and separate the waveguide insertion loss from the waveguide propagation loss [38], however the geometry of suspended waveguides precludes us from using most of these methods. One of the simplest and most common methods for testing optical waveguide loss is the cutback technique [38-40]. In this method, the output power of a waveguide is measured, then the waveguide is cleaved and the power measured again. This process is repeated

several times. The idea is that the insertion losses should be the same each time since the same waveguide and measurement tools are used while waveguide propagation loss decreases linearly with decreasing waveguide length. The set of measurements can then be used to separate the waveguide insertion loss and waveguide propagation loss. Once InP waveguides have been released and suspended above the substrate, however, they are no longer attached to the rest of the single-crystal substrate and new facets can not be cleaved. An interesting nondestructive testing method that can be used in our case is the Fabry-Perot contrast method [38]. Using the Fabry-Perot contrast method, the waveguide propagation loss can be extracted provided a tunable laser source is available. A second method we employed is simple relative power measurement. If the measured power output for a single waveguide is repeatable, then it can be assumed that the insertion loss is reproducible since the propagation loss is constant. By utilizing an advanced automatic fiber alignment system, we were able to record very repeatable measurements, making relative power measurements another useful measurement technique.

A schematic diagram of the measurement setup used is given in Figure 4-1.

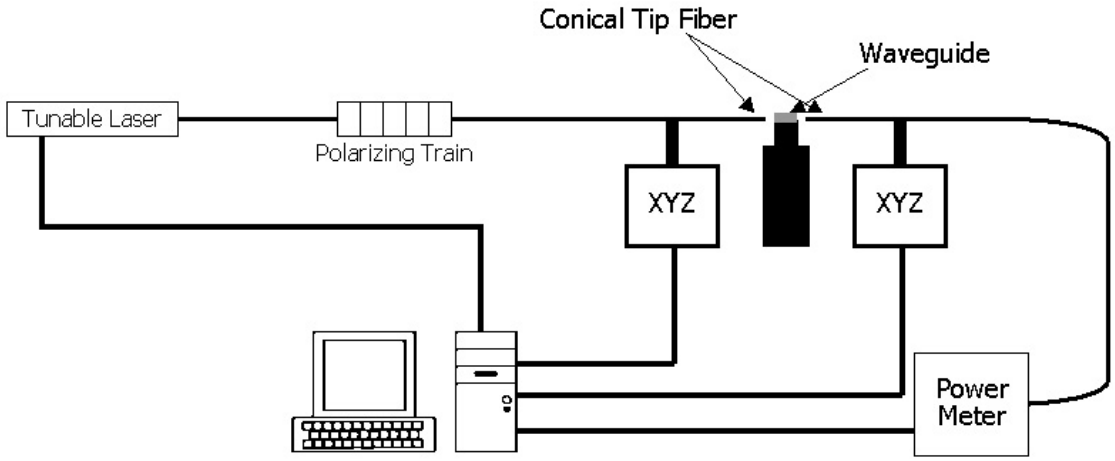

Figure 4-1: Schematic of experimental setup for characterization of suspended InP waveguides.

The optical signal originates from a tunable laser source with 3 mW maximum output power and wavelength tunability from 1500 – 1637 nm. The light is routed through low-loss optical fiber to a polarizing train. In conjunction with a polarizing prism, the polarizing train can be used to tune the system to couple either Transverse Electric (TE) or Transverse Magnetic (TM) modes into the waveguide. The optical fiber is spliced to a lensed-tip fiber with an 8 μm focal length. This focuses the optical beam onto the input facet of the waveguide under test. Another conical tipped fiber is used to couple the optical beam from the output facet of the waveguide. A germanium detector continuously monitors the output power, which is measured by an optical power meter calibrated to the detector. Both input and output conical tipped fibers are mounted on 4-axis micropositioning stages with stepper motors realizing 0.05 μm resolution. The waveguide chip under test is mounted on a copper block with a silver epoxy and is then placed on a fixed support between the fibers. A Newport AutoAlign^{TM} computer system controls the tunable laser, input and output fiber alignment, and monitors the output power. With this setup, both input and output lensed-tip fibers can be positioned to achieve maximum coupling efficiency with excellent resolution. By automating this critical alignment, we are able to obtain repeatable insertion losses so that measurements can be directly compared. Having computerized measurement and laser tuning ability with the Newport computer system also has the advantage of automating data recording. The measured output power for every input power and wavelength can be recorded in a data file to facilitate the analyses of the waveguide data.

4.3 Testing Methods

Two waveguide testing methods were used to characterize the suspended waveguides. The first, simpler method is relative power measurements that can only measure the combined insertion and propagation loss of a waveguide. The second method is the Fabry-Perot contrast method [38]. This technique uses Fabry-Perot resonance in the waveguide to determine the propagation loss, removing the insertion loss from the calculation entirely. In the end, the results from both methods agreed very well, supporting the validity of our measurements.

Relative power measurements are very useful for comparing the total loss of several waveguides. The method is simple:

1) Use the Newport AutoAlign^{TM} to optimize the alignment of both the input and output conical tipped fibers. The fiber tip is maintained 8 μm from the waveguide facet.
2) Tune the laser to a set power and wavelength, in our case 2 mW and 1550 nm.
3) Again using the Newport AutoAlign^{TM}, scan the input fiber across the waveguide facet in both X- and Y- directions. The measured output from this scan is recorded in a data file by the computer.
4) Optimize alignment for the next waveguide to be tested and repeat until all waveguides have been measured.
5) Repeat the entire process at least 3 times for all waveguides.

The results from the measurements obtained by this method are recorded in an Excel file and can be analyzed in Matlab. We are able to obtain very repeatable measurements with this method, with a run-to-run variation of less than 5%. We developed step 3 of this procedure in order to achieve provide these accurate and repeatable results. The problem encountered was that due to the small size of the waveguide facets (2 μm), the alignment tolerance is extremely tight. Figure 4-2 shows a scan of position versus measured output power. It can be seen that a fiber offset of only a few tenths of micons dramatically reduces the coupling efficiency. Even though the positioning system used is extremely precise, vibrations not damped by the air table and even air currents can move the fiber tip by small amounts, so an optimized alignment one moment might not be optimized the next moment. By sweeping the fiber tip across the facet in 0.05 μm increments and recording the output, however, the maximum coupling efficiency will lie somewhere within the sweep and can be read out from the data recorded by the computer. A Matlab program was written to read through all the data files created during the measurements and extract the maximum of each sweep. This method allowed us to achieve our excellent repeatability.

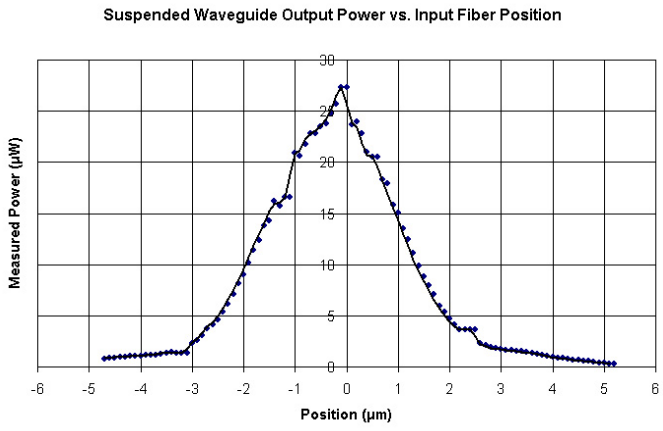

Figure 4-2: Measured waveguide output power versus input fiber position.

Fabry-Perot contrast analysis uses the constructive and destructive interference of light propagating in the waveguide and reflecting from the waveguide facets to measure and calculate the waveguide propagation loss. The resonance condition for light of wavelength λ propagating in a waveguide cavity of length L_w is given by:

$$L_w = 2N(n\lambda) \tag{4.2}$$

Where N is an integer and n is the refractive index of the waveguide. By tuning the input laser wavelength, the resonance condition of the waveguide cavity changes and maximum and minimum output power peaks occur.

In an ideal waveguide with no propagation loss and perfectly reflective facets, the minimum output power due to destructive interference would be zero (of course with perfectly reflective facets this would be impossible to measure). This condition represents a contrast of 1 between the peaks and troughs of the output power where the Fabry-Perot contrast is given by equation 4.3 [38]:

$$K = \frac{T_{\max} - T_{\min}}{T_{\max} + T_{\min}} = \frac{2r}{1 + r^2} \tag{4.3}$$

T: waveguide transmitted power
$r = \mathrm{Re}^{-\alpha L}$

In this case, 100 percent of the power launched into the waveguide reflects from the output facet, reflects from the input facet, returns to the output facet π radians out of phase. As the reflectivity of the facets decreases and the propagation loss increases, smaller fractions of the initial power incident on the output facet actually return out of phase to cause destructive interference. The total out-of-phase power at the output facet

of the waveguide forms a geometrical series with the total transmitted power given by equation 4.4 [38]:

$$T(\phi) = \frac{(1-R)^2 e^{-\alpha L}}{(1-r) + 4r\sin^2\phi} \tag{4.4}$$

T: transmission
Φ: phase
R: facet reflectivity
α: propagation loss
$r = Re^{-\alpha L}$

Combining these two equations, the relation between K, R, and α is shown in equation 4.5 [38]:

$$\ln\left[\frac{1-(1-K^2)^{\frac{1}{2}}}{K}\right] = \ln R - \alpha L \tag{4.5}$$

It can be seen from this equation that the contrast ratio between measured peaks and troughs in the output power is a function of only the waveguide facet reflectivity and waveguide propagation loss. So if the waveguide reflectivity is known, the propagation loss can be determined from waveguide transmission measurements.

Due to the difficulty of measuring the reflectivity of the facets and our inability to perform cutback on the waveguides, we begin by making the assumption that the reflectivity of the facet for the 0^{th} order mode with effective index, n = 3.193 is:

$$R = \left[\frac{n-1}{n+1}\right]^2 = 0.274 \tag{4.6}$$

Where n is the effective refractive index of the 0^{th} order waveguide mode and 1 is the refractive index of air. In our case, we only want to compare several variants of waveguides with increasing number of tethers and tether width to determine the effects of the tethers. The precise value of the facet reflectivity is actually not critical as long as the reflectivity is consistent between waveguides, which is ensured since all waveguides being compared share the same facet cleave. This facet reflectivity is the key assumption made in our Fabry-Perot contrast measurements.

In order to ensure accurate measurements, a wavelength scan is initiated from 1540 nm to 1560 nm for each waveguide. The Free Spectral Range (FSR) (equation 4.7, [4, p. 125-131]) for the 2.5 mm waveguides is only 0.15 nm, so numerous peaks and troughs occurred over this range.

$$FSR = \Delta\lambda = \frac{{\lambda_0}^2}{2nL} \tag{4.7}$$

A LabVIEW program recorded all of the data into a file and a Matlab program was written to average the waveguide propagation loss calculated throughout the range based on equation 4. This average is then used as the waveguide propagation loss measured by the Fabry-Perot contrast analysis.

Due to the unique structure of suspended waveguides, there are actually several resonant cavities within the waveguide: between the end facets and between any two tether pairs. Equation 2.2 demonstrates, however, that the reflection coefficient, R, at the interface of the waveguide tethers is $2.2 \cdot 10^{-7}$. This is negligible compared with the reflection coefficient of the waveguide facets, 0.274, so resonant cavities established by the tethers should have no effect on our measurements. In fact, analyzing the measured

data at the FSR expected for the resonant cavities between tethers did not reveal any measurable trends.

4.4 Results of Relative Power Measurements

Relative power measurements were used to characterize the tether attenuation of the suspended InP waveguides as a function of tether width. Our waveguide design uses 1.5 μm wide tethers as the standard. All measurements of waveguide loss with respect to number of tethers use these standard 1.5 μm tethers. Waveguides with an identical number of tethers but various tether widths were tested to determine the optical loss per tether as a function of tether width. The Matlab simulation was used to fit a geometric series curve to the measured output power versus number of tethers. From this fit, we can extract the measured loss per tether. The data is expected to display a geometric trend because the power loss of each tether is a fraction of the incident power on that tether. As such, each subsequent tether causes less power loss than the previous. Figure 4-3 shows a plot of output power versus number of tether pairs. From this data we calculate a loss per tether pair of 0.24 dB. Figure 4-4 shows another plot of the measured data along with the results of our Matlab simulation. The width of the tethers was measured using an SEM and used as the width parameter for the simulation. It can be seen that the results of our measurements and our simulation agree very well, the simulated loss per tether pair is 0.25 dB.

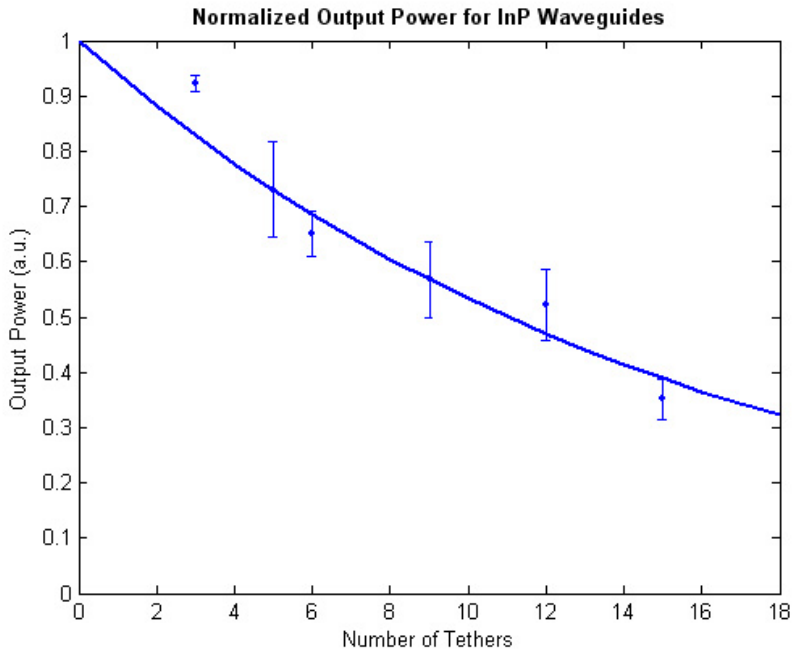

Figure 4-3: Normalized output power versus total number of tether pairs for 1.5 μm tethers on a 2.5 mm long waveguide.

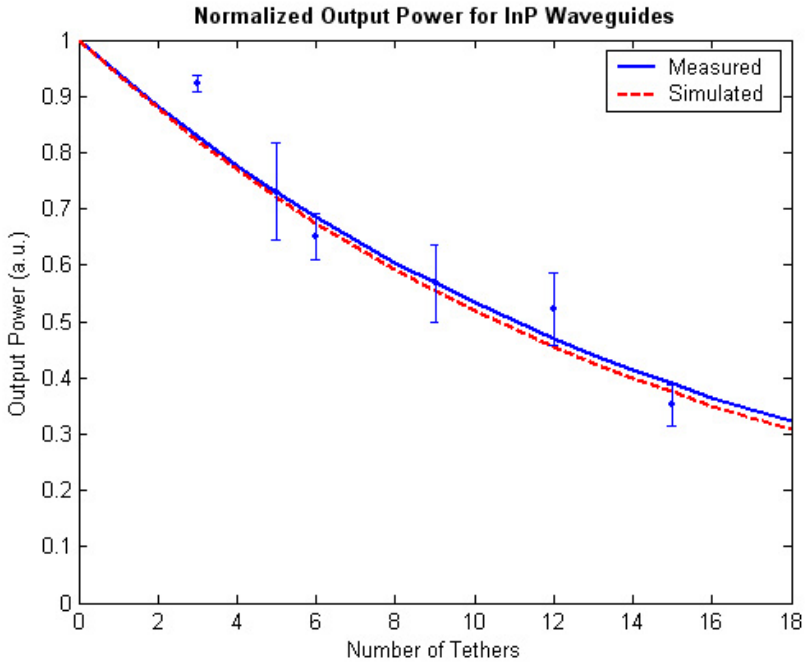

Figure 4-4: Normalized output power versus total number of tether pairs for 1.5 μm tethers showing both measured power and power output predicted by simulations.

Output power measurements were recorded both before and after the sacrificial release of the waveguides. Figure 4-5 shows a plot of the same set of waveguides before and after the sacrificial InGaAs layer removal. Figure 4-6 shows only the measured power before InGaAs removal.

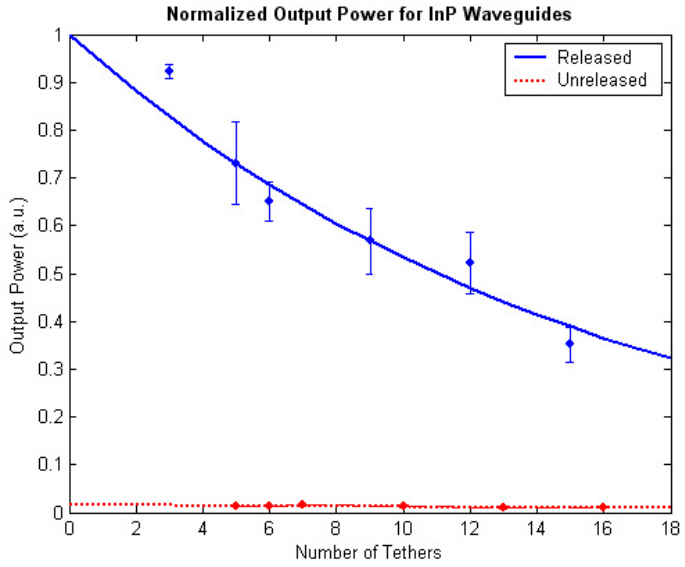

Figure 4-5: Plot of waveguide output power versus number of tethers before and after sacrificial release for a 2.5 mm long waveguide.

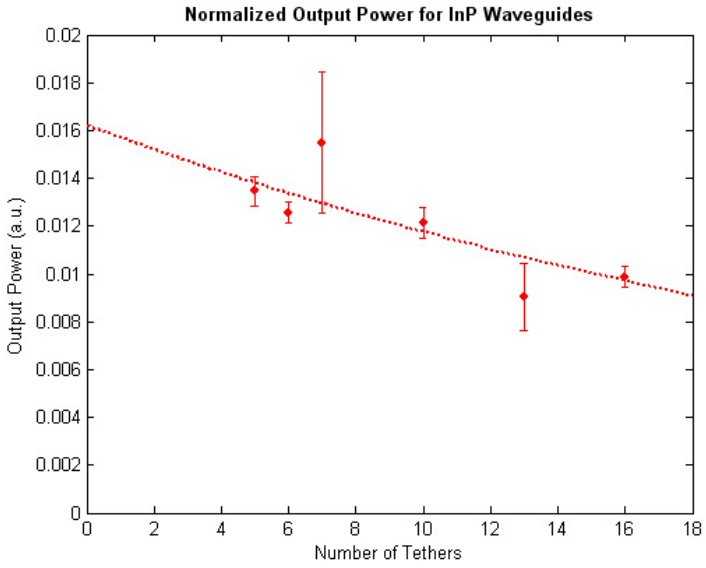

Figure 4-6: Close up from Figure 4-5 of waveguide output power versus number of tethers with InGaAs layer retained beneath the waveguides.

From this data, it is apparent that removal of the entire sacrificial layer from under the waveguides is necessary, as assumed. A gain of 17.3 dB is demonstrated by the sacrificial layer removal for a 2.5 mm waveguide with 6 tether pairs. Although the lateral suspensions used in our suspended waveguides induce an additional loss, they are better than a 30 times improvement over retaining the sacrificial layer beneath the waveguides.

Figure 4-7 is a plot of measured output power with increasing tether width. Also plotted are the results of the Matlab simulation assuming a Gaussian beam expansion within each tether pair. The agreement between these two curves indicates that this assumption is good and Gaussian beam expansion can be used to model the beam behavior within a tether.

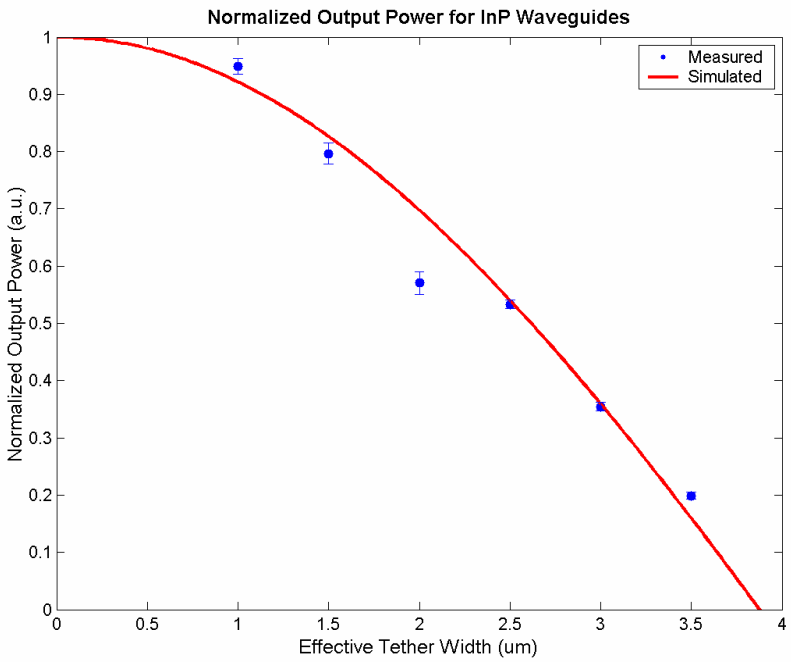

Figure 4-7: Normalized output power versus effective tether width for waveguides with 9 tether pairs. The simulated output power is also plotted.

Again, it should be pointed out that these results are for *effective* tether width, not designed tether width:

$$W_{eff} = W_T + 0.5\,\mu m$$

Figure 4-8 highlights the difference between these two dimensions due to processing limitations. As a result, the 1.5 μm tethers used as the standard are actually plotted as 2.0 μm wide tethers for data analysis. The results indicate that decreasing the tether design width from 1.5 μm to 0.5 μm would produce up to 0.16 dB decrease in loss, yielding 0.08 dB of loss per tether pair while maintaining structural support. Combined with a proven tether spacing of 2.5 mm, a waveguide up to 1 cm in length would require only 5 tether pairs, equating to only 0.40 dB of optical loss due to the tether suspensions.

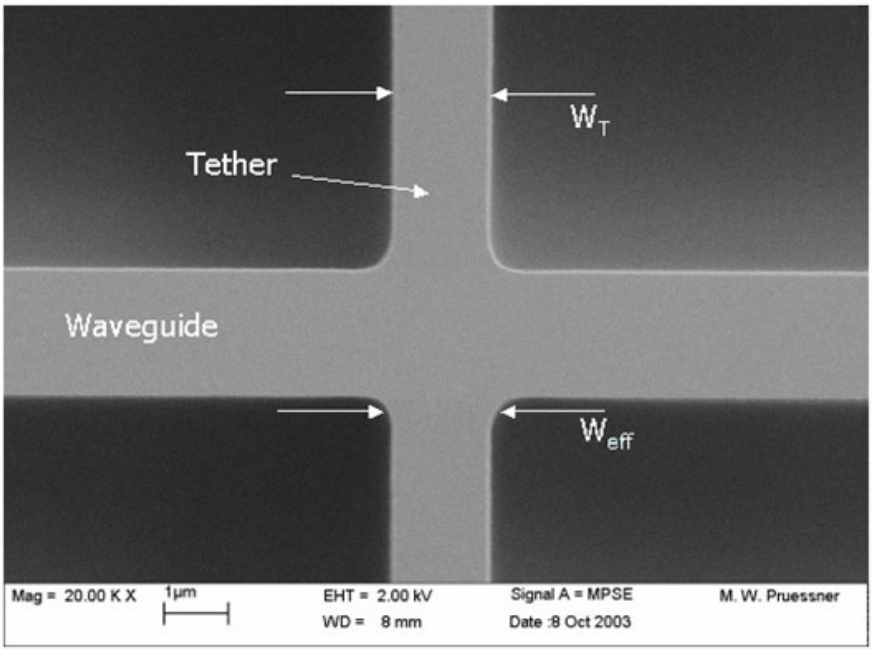

Figure 4-8: SEM micrograph highlighting the difference between the designed tether width (W_T) and the effective tether width (W_{eff}).

4.5 Results of Fabry-Perot Contrast Analysis

Fabry-Perot contrast analysis was used to determine the waveguide propagation loss of our fabricated and released suspended waveguides. For each waveguide, the measurement was repeated at least three times to ensure repeatability. A graph of the output power versus a portion of the wavelength scan for a waveguide with 9 1.5 μm tether pairs is shown in Figure 4-9. Figure 4-10 shows the results of the entire analysis. Two characteristics of the waveguides can be determined by this graph. First, slope of the line reveals the loss contribution of the tethers in dB/tether pair. This slope indicates 0.25 dB of loss per tether pair, an extremely close agreement with the results of the relative power measurements, which give a loss per tether pair of 0.24 dB. This very good agreement lends credibility to the measured data. Of further interest, by extending the line in Figure 4-10 to the y-intercept, waveguide propagation loss due to material absorption, interface scattering, and refractive index inhomogeneity scattering is revealed. This measured waveguide propagation loss is 2.2 dB/cm, on par with a first generation semiconductor waveguide [28,30,38,40].

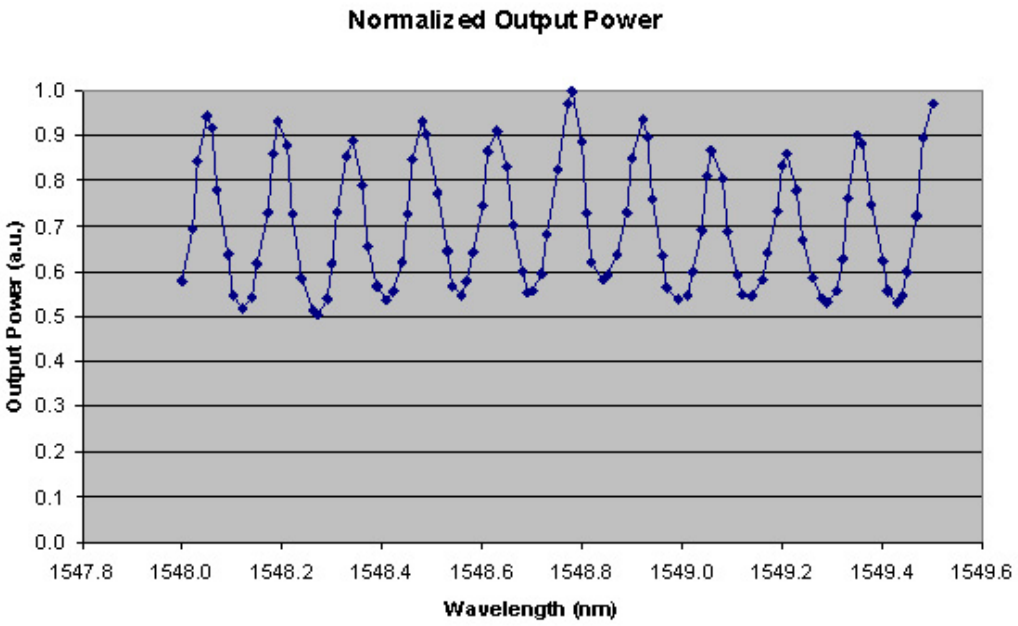

Figure 4-9: Normalized output power versus wavelength for a suspended waveguide with 9 1.5μm tether pairs. Only a portion of the wavelength scan is plotted to show detail.

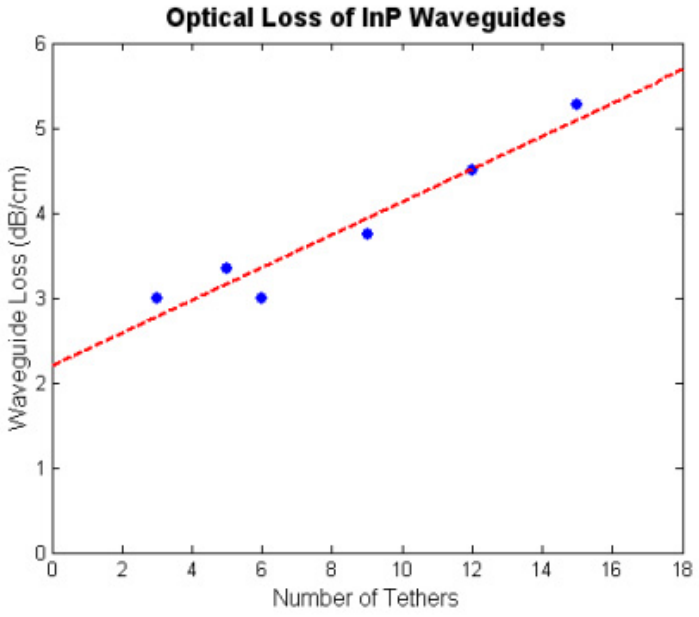

Figure 4-10: Measured waveguide loss versus number of tethers, obtained from Fabry-Perot contrast measurements and calculations.

4.6 Summary of Results

A summary of the results of our waveguide characterization is given in Table 4-2.

Property	Value
Waveguide Loss	2.2 dB/cm
Tether Loss	0.24 dB/pair (W_T = 1.5 μm), r*elative power measurements* 0.25 dB/pair (W_T = 1.5 um), *Fabry-Perot contrast* 0.25 dB/pair (W_T = 1.5 um), s*imulated* 0.08 dB/pair (W_T = 0.5 μm), *calculated*
Maximum Tether Spacing	2.5 mm (maximum demonstrated)

Table 4-2: Summary of suspended waveguide parameters.

The waveguide propagation loss is comparable to other first generation semiconductor waveguides, usually around 1 to 4 dB/cm [28,30,38,40]. The additional losses due to the tether supports are over 30 times smaller than substrate leakage losses caused by the sacrificial InGaAs under the waveguide, demonstrating the necessity for developing the novel suspended waveguide structure for released waveguides in InP. Being equivalent to other semiconductor waveguides, our results show that the fabricated suspended InP waveguides are a viable technology for implementing InP waveguide MEMS.

The loss of the waveguides could be improved through several methods. The most straight forward and obvious would be to decrease the designed tether widths to 0.5 μm, which would result in only 0.40 dB of loss contribution by the tethers for a 1 cm waveguide versus 1.2 dB introduced by 1.5 μm tethers. The waveguide propagation loss itself could be reduced by improving the fabrication process, particularly the InP etch and reduction of the resulting roughness. Good results have been obtained by other groups

using an Inductively Coupled Plasma (ICP) etcher for InP [30,31]. For future devices this technique could be investigated.

The results in Table 4-2 provide a very useful guideline for the design of InP waveguide MEMS using suspended waveguides. The waveguide propagation loss is a function of the dimensions and the sidewall roughness of the waveguide, so each set of fabricated devices could vary slightly. The loss contributed by the tether pairs can also vary since tether loss is a function of both effective tether width and initial mode diameter (equation 2.3). Further optimization of the photoresist processing could bring the effective tether width closer to the designed tether width, reducing tether loss. On the other hand, reducing the waveguide dimensions to move towards single mode will decrease the initial mode diameter, increasing tether loss. Even though the characteristics of future suspended waveguides will vary, these results establish a baseline as well as the general trends and behavior of suspended waveguides. With the design, fabrication process, and basic waveguide characteristics in place, InP suspended waveguides are ready to be implemented as a key technology for development of InP waveguide MEMS.

Chapter 5 – Conclusion and Future Work

This chapter is a summary of our achievements and the importance and impact of our results. The optical properties and fabrication sequence of InP suspended waveguides are the most important contribution of this work. InP optical MEMS devices using suspended waveguides for switching and filtering of optical signals are currently under development. Published results from these devices are reviewed. Functional MEMS systems using a suspended waveguide infrastructure emphasize that suspended InP waveguides are an enabling technology for InP waveguide MEMS.

5.1 Suspended InP Waveguides as a MEMS Platform Technology

The goal of this research is to establish suspended InP waveguides as a MEMS platform technology. To the best of our knowledge, there are currently no published InP waveguide MEMS devices capable of lateral, in-plane actuation. In order to create this type of device, it is necessary to have a waveguide released from the substrate. In the InP material system, this sacrificial release presents a significant obstacle - our solution is the suspended InP waveguide. In order to establish the suspended InP waveguide design as a MEMS platform technology, we had to first design the waveguides for a given set of requirements, develop a simple and robust fabrication process for the waveguides, and characterize the optical properties of the suspended waveguides.

To establish the initial design of the suspended InP waveguides, we employed analytical models, waveguide simulation packages, and material parameters to define the waveguide materials and dimensions. An analytical model of the tethers used to support

the waveguides was written in Matlab. The model was able to provide a prediction of the optical losses caused by the tethers including the effect of tether width and number of tethers. With these results, we were able to predict that a 1.5 μm wide pair of tethers would add 0.25 dB of loss while maintaining waveguide structural rigidity. We used the Optical Waveguide Mode Solver (OWMS) finite-element analysis package to design the dimensions and the desired refractive indices of the waveguide itself. Although single mode operation is ideal, we chose a balance between mechanical robustness and ideal optical dimensions. A core size of 2 μm x 2 μm was selected to ease mechanical alignment tolerances for the MEMS waveguides, even though these dimensions result in multi-mode operation. Once the waveguides have been proven in a MEMS application, reducing the waveguides to single mode operation for the next generation of devices can be pursued. The final design parameters for the suspended InP waveguides are given in Figure 5-1 and a conceptual drawing of the suspended waveguides is shown in Figure 5-2.

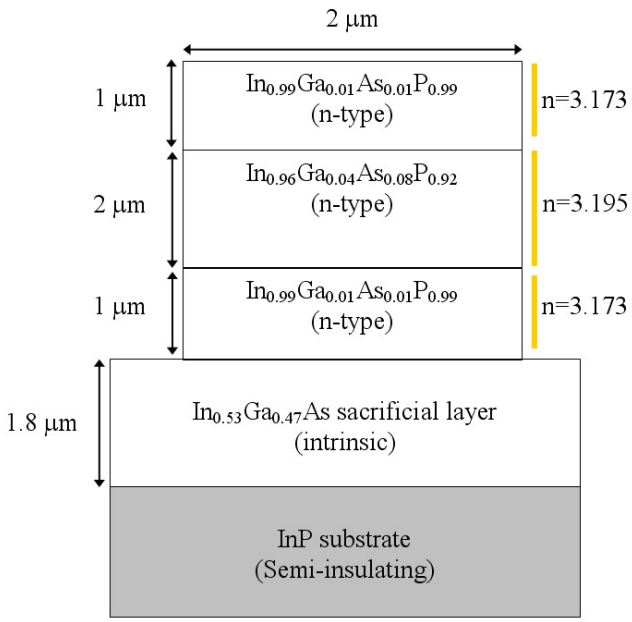

Figure 5-1: Schematic diagram of InP suspended waveguide design.

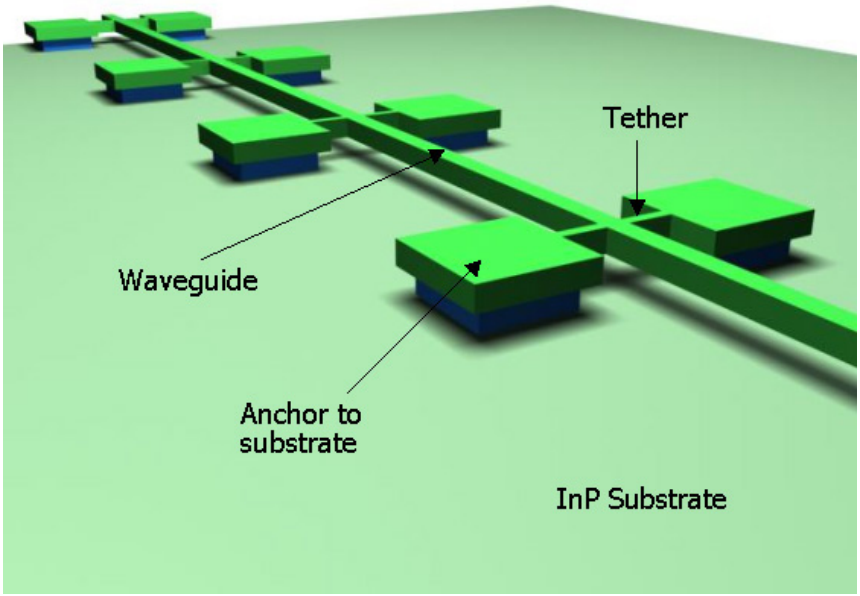

Figure 5-2: Conceptual drawing of a suspended InP waveguide.

It is one thing to be able to design a device, however it is something else entirely to design a device that can actually be fabricated in the lab. In our case, we needed to not

only be able to fabricate the designed waveguides, but to come up with a simple, robust, repeatable fabrication process since these waveguides will become a basic component of InP waveguide MEMS. We have successfully established this fabrication process which involves only a single lithography step and three etch steps. The initial epitaxial wafer growth is performed by solid-source molecular beam epitaxy (MBE) and the thickness and compositions of the layers are precisely controlled. A plasma enhanced chemical vapor deposition (PECVD) silicon dioxide hard mask is used as the masking layer for the InP waveguides – advantageous since PECVD oxide is a well established material and readily available. An InP dry-etch has been developed in a RIE system using hydrogen, methane, and oxygen, all of which are available in many RIE systems. This etch required a great deal of process development, however it is now in a very mature state and can repeatably and reliably produce highly-vertical sidewalls up to 5.6 μm in height with optical-quality smoothness. These sidewalls demonstrate 89° verticality and less than 50 nm roughness. The final etch step is a wet etch in hydrofluoric acid, hydrogen peroxide, and DI water (1:1:8) followed by supercritical drying in CO_2. Figure 5-3 through Figure 5-5 show SEM images of the fabricated waveguides. One of the greatest advantages of this fabrication process is that it is simple in the vertical direction, with only a few deposition and etch steps, but complexity in the lateral direction is unlimited and defined by a single mask. This means that this identical process flow can be used to fabricate simple waveguide test devices such as those presented here, or complex devices with waveguide bends, gaps, Bragg reflectors, comb-drive actuators, and any other features desired for an integrated optical MEMS system.

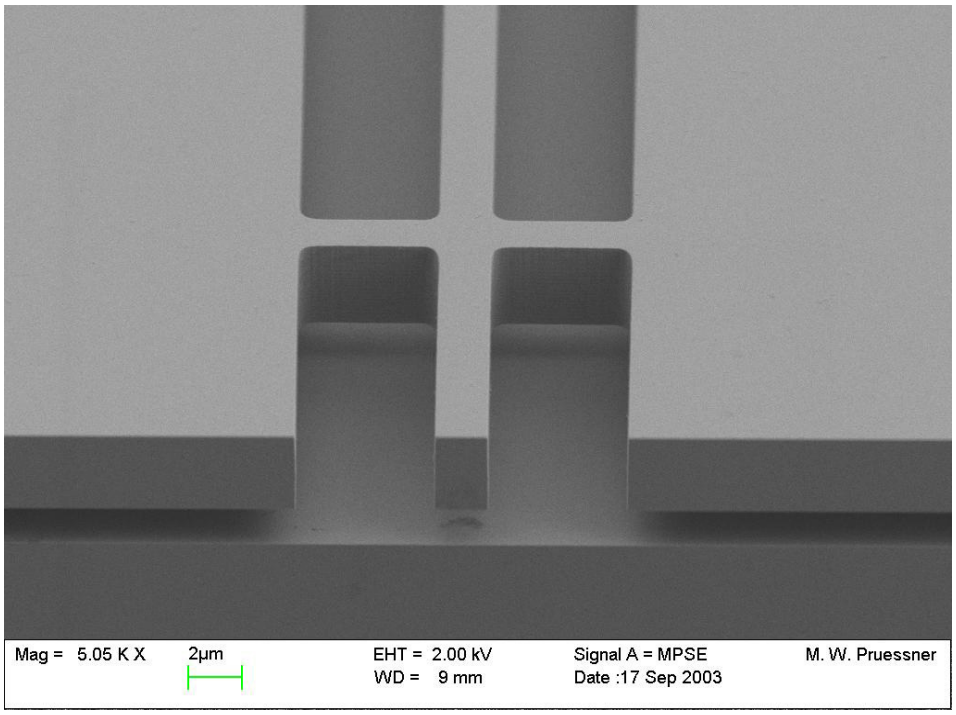

Figure 5-3: SEM micrograph of the end facet of a fabricated suspended InP waveguide. A pair of tethers is also shown.

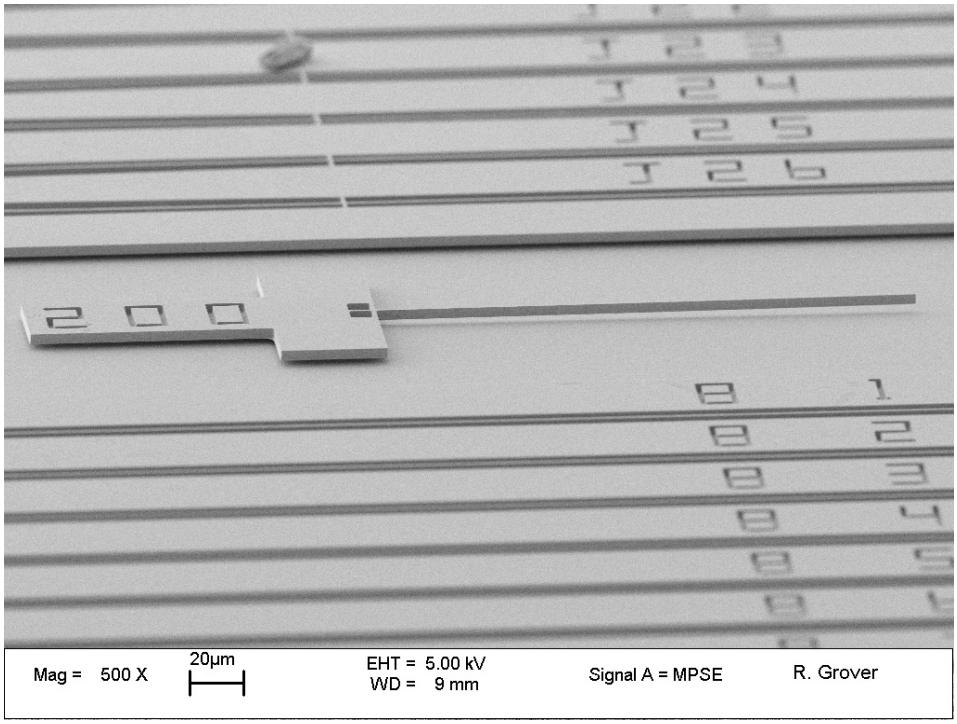

Figure 5-4: SEM image displaying long, perfectly flat segments of suspended waveguides (bottom) and sections of waveguide with tethers (top). A 200 µm long waveguide cantilever test structure is also shown (middle).

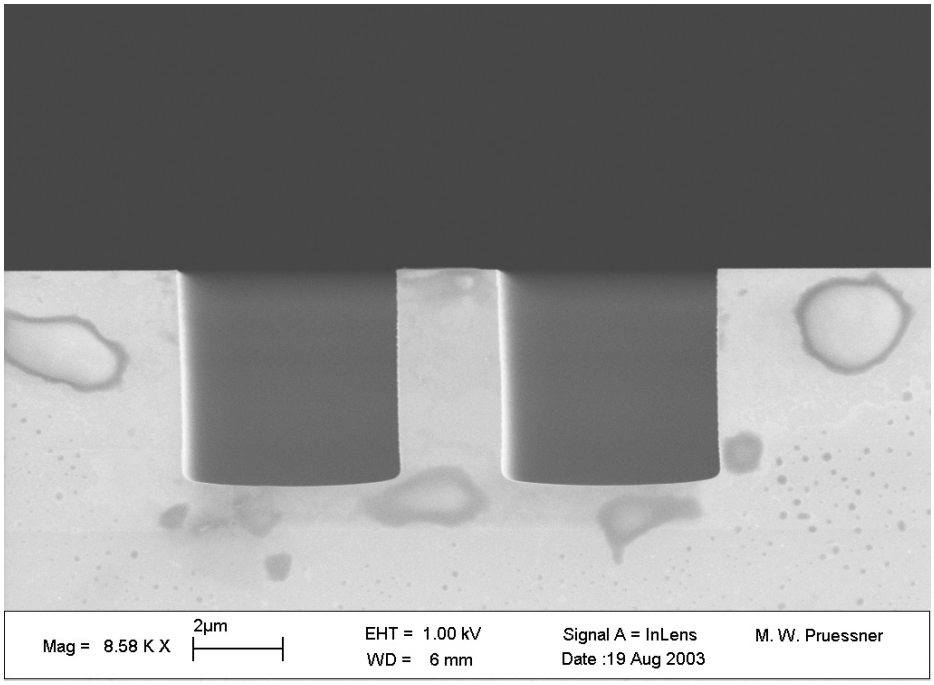

Figure 5-5: SEM micrograph of cleaved facet of an unreleased InP waveguide.

After simulating, designing, and fabricating the suspended InP waveguides, the next step was to understand their optical properties and to test the predictions from our simulations. We tested the waveguides using two methods: relative power measurements and Fabry-Perot contrast analysis. The results from both techniques for tether loss agreed within 0.01 dB, giving 0.24 and 0.25 dB respectively for a 1.5 μm wide tether. Even through this is a fairly large loss, the results regarding loss versus tether width are very promising. We found that reducing the designed tether width to 0.5 μm results in a loss of only 0.08 dB per tether pair. With 2.5 mm tether spacing, a 1 cm waveguide could be suspended by only 5 tether pairs contributing a total loss of 0.40 dB. We also demonstrated a 17.3 dB gain in power by removing the entire InGaAs sacrificial layer from beneath the waveguides. So while the tethers would introduce 0.40 dB additional loss, not releasing the entire waveguide introduces 17.3 dB of loss, making the tethers a very good alternative.

Property	**Value**
Waveguide Loss	2.2 dB/cm
Tether Loss	0.24 dB/pair (W_T = 1.5 μm), *relative power measurements* 0.25 dB/pair (W_T = 1.5 um), *Fabry-Perot contrast* 0.25 dB/pair (W_T = 1.5 um), s*imulated* 0.08 dB/pair (W_T = 0.5 μm), *calculated*
Maximum Tether Spacing	2.5 mm (maximum demonstrated)

Table 5-1: Summary of suspended waveguide properties.

5.2 Extension of Suspended InP Waveguides to Devices

The goal of this research was to study the design, fabrication, and optical properties of suspended InP waveguides. We isolated the optical properties of the waveguides by not introducing the additional factors of mechanical movement and actuation. Our group has already performed a rigorous study of the mechanical properties of InP thin films [22], so the next step is to combine the two studies and create actuated suspended InP waveguide devices. Figure 5-6 shows a schematic of a single-ended suspended waveguide that can be used for waveguide actuation since it is only fixed at one end.

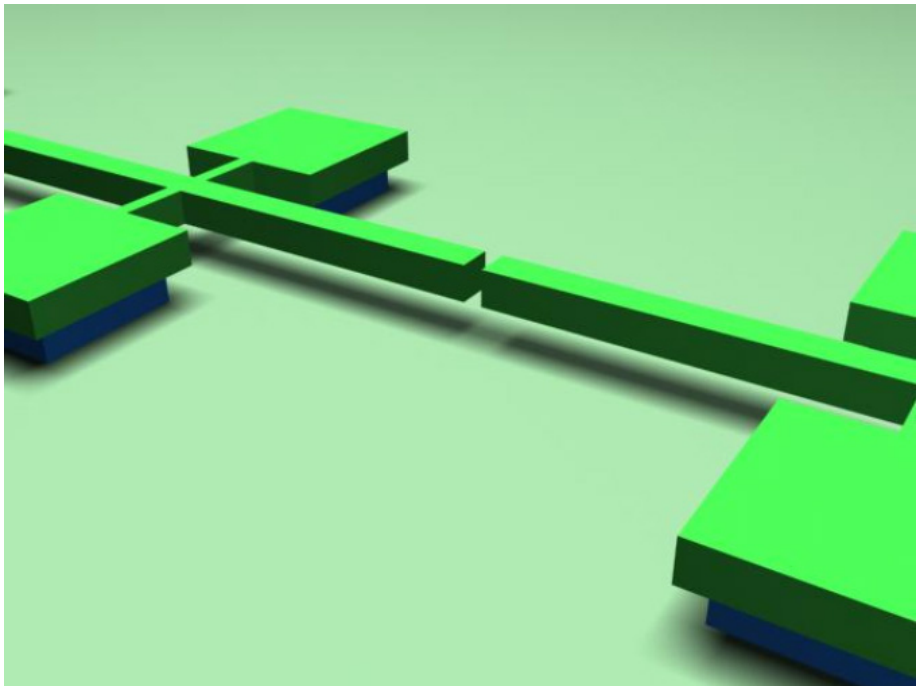

Figure 5-6: Schematic of single-ended suspended waveguide. By actuating one end of the cantilever waveguide to the left or right, the amount of power coupled to the second waveguide is controlled.

We included an n-type doping of $5 \cdot 10^{17}$ in the InP waveguide layer growth so that the waveguides are conductive while the substrate is counter-doped to be semi-insulating. A 50 nm 10^{19}-doped n-type InP capping layer was also grown on top of the waveguides to allow good ohmic contact with deposited metal. By incorporating these attributes, the waveguides fabricated and tested for this research have the potential for lateral (in-plane) electrostatic actuation – the only missing elements are lateral electrodes and metal contact pads. The electrodes, comb-drive or otherwise, would be included on the same mask and undergo the same fabrication steps as the waveguides, so the process is no more complex than fabrication of waveguides alone. Deposition of metal pads requires a further lithography step, metal deposition by e-beam evaporation, and liftoff in acetone. Alignment is not critical for this step and a contact aligner can be used to simplify the lithography.

Figure 5-7 shows the concept of how a simple, electrostatically actuated waveguide switch using suspended InP waveguides could be implemented. An electrode on either side of the input waveguide can pull it left or right to align with either output waveguide. Development and testing of this type of 1x2 waveguide switch is currently underway.

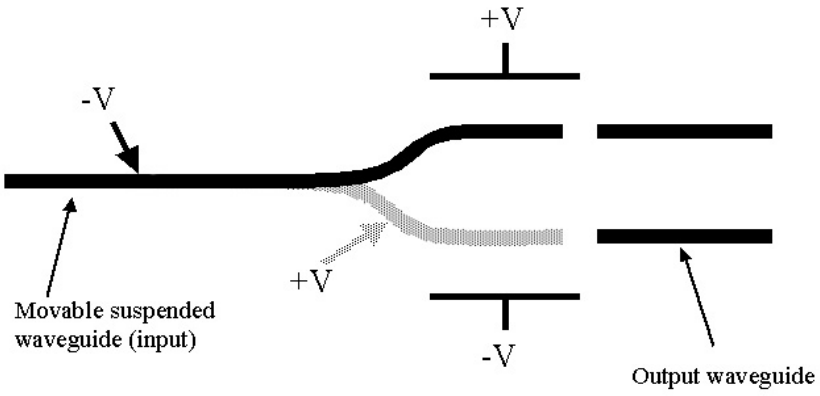

Figure 5-7: Diagram of a simple 1x2 waveguide switch with electrostatic actuation (top view).

5.3 Design Improvements

For the next generation of suspended InP waveguides, there are several improvements to be implemented in the design. These include smaller or redesigned tethers, an improved InP etch, and single mode waveguides. The current tether design of 1.5 μm wide tethers can exhibit a 0.16 dB reduction in loss per tether pair by simply reducing the designed width to 0.5 μm, resulting in 0.08 dB/tether pair rather than 0.24 dB/tether pair. It is also possible that redesigning the waveguide supports could yield even better results – InGaAs supports beneath the waveguide may be an excellent alternative. Although we have shown that InGaAs beneath the waveguide does cause large leakage and absorption losses into the substrate, a short (~5 μm) InGaAs support beneath the waveguide should actually exhibit less optical loss than the tethers since the InGaAs is buffered from the 0^{th} order optical mode by the lower cladding while the tethers are not. This would require another lithography step just before the sacrificial etch to pattern the InGaAs posts, but the alignment is not critical and a contact aligner can be used. The timing of the sacrificial etch, however, would be critical in order to obtain the desired InGaAs post width.

The current RIE etch of InP has been developed to be very robust and repeatable. It yields sidewalls up to 5.6 μm deep with 89° verticality and less than 50 nm sidewall roughness. Still, the etching process is very sensitive to contaminants and extremely lengthy – including chamber conditioning it can take up to 30 hours. An improvement in the speed of this etch would be highly beneficial to our process, and if smoother sidewalls can be obtained the waveguide scattering loss could decrease dramatically, leading to an even less lossy waveguide. The current etch process could be further optimized by

decreasing chamber clean times gradually until the minimum necessary conditioning times are found. Even better yet, an RIE system devoted to etching InP could be kept clean, free of contaminants, and conditioned to InP etching. This would be a great benefit to our future work. Finally, another option to experiment with is using an ICP etcher. Other groups have had success with this type of etch for InP and InGaAsP with etch rates of 0.4 - 0.6 μm/min and very smooth sidewalls [30,31].

Once we have demonstrated mechanical actuation with the current generation of waveguides and characterized the waveguide alignment tolerances, the next step would be to move toward single-mode waveguides. In current long-haul optical networks, single mode fiber and communication is used almost exclusively. The modal dispersion in multimode optical fibers is too great for multimode fibers to be used for long distances and high data rates. For this reason, it is important that our final devices operate in the single mode domain to exploit the full benefits of all-optical MEMS. The reason we have developed multimode waveguides for this research is to simplify the initial development stages of InP waveguide MEMS as a new technology.

In order to achieve a single-mode waveguide and still retain large dimensions to facilitate mechanical actuation and alignment, it is possible that surrounding the static regions of our waveguides with a photo-definable dielectric such as benzocyclobutene (BCB) could help reduce the large waveguide-air refractive index contrast of 2.2 that currently leads to the support of multiple modes in our waveguides [41]. There are several compositions of BCB with refractive indices in the 1.5 range, so the waveguide refractive index contrast could be reduced to about 1.7. Reducing the index contrast

would also help reduce the waveguide propagation loss due to interface roughness since this loss is proportional to the square of the interface index contrast [28].

Using substrate leakage to radiate higher-order modes into the substrate is another proven method to achieve single mode operation in a waveguide with large dimensions [28]. Because a larger fraction of the power in the higher-order modes travels in the waveguide cladding than the 0^{th}-order mode (Figure 5-8), these modes are more susceptible to substrate leakage. Segments of the InGaAs sacrificial layer could be retained beneath the waveguides to not only serve as support, but also to radiate the higher-order modes. Although this would lead to a greater waveguide propagation loss, this could be slightly offset by obtaining smoother sidewalls and by using BCB to reduce the waveguide refractive index contrast. Additionally, because the dimensions of MEMS devices are small, only short lengths of InP suspended waveguide are necessary (~1 cm), so the impact of the slightly greater waveguide propagation is minimized.

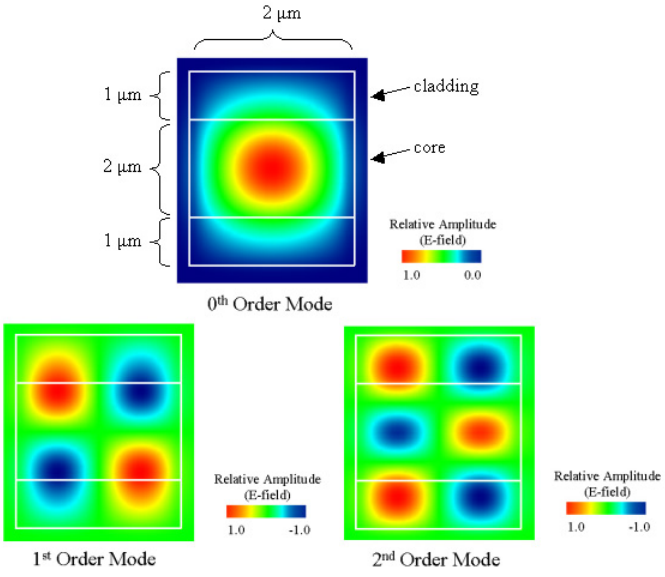

Figure 5-8: OWMS simulation results for the first 3 supported optical modes in InP suspended waveguides. A larger fraction of the power in the higher-order modes travels outside the waveguide core than in the 0th order mode.

5.4 Applications of Suspended InP Waveguides

After developing the fabrication process and characterizing suspended InP waveguides, the next step is to incorporate this platform technology into an optical waveguide MEMS device. Development and testing of several InP MEMS devices based on suspended waveguide technology is ongoing and includes a MEMS waveguide evanescent coupler, end-coupled MEMS waveguide 1x2 switch, and an in-plane tunable Fabry-Perot filter.

Figure 5-9 shows a diagram of an evanescent waveguide coupler using suspended InP waveguide technology [42]. Figure 5-10 shows an SEM image of the fabricated waveguide evanescent switch. The coupler is able to achieve low voltage (5.4V) actuation, 60% coupling efficiency, 47 dB channel isolation in the off state, and 1 ms switching time. With these properties, the evanescent parallel-coupled switch could also potentially function as a variable power splitter/attenuator. In addition to the basic suspended waveguide fabrication process, Ni-Ge-Au-Ni-Au ohmic contacts were deposited onto the waveguides via e-beam evaporation and patterned with a photoresist lift-off. This allows electrical contact to the suspended waveguides.

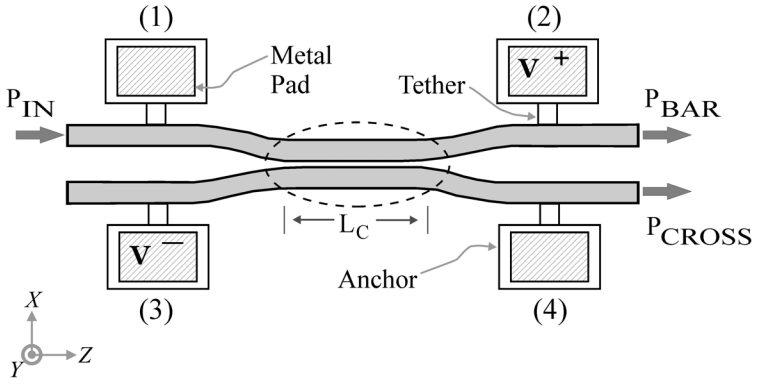

Figure 5-9: Diagram of InP waveguide evanescent coupler [42].

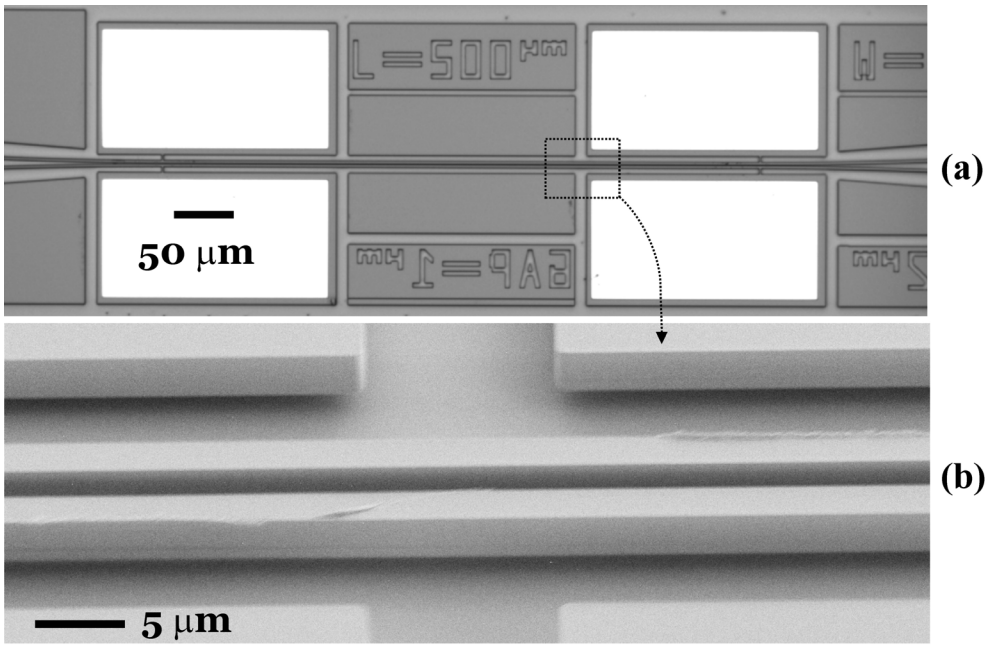

Figure 5-10: SEM micrograph of fabricated waveguide evanescent coupler (a) and a close-up showing the two parallel suspended waveguides in the off state [42].

Investigation into the switching characteristics of the evanescent coupler revealed that the actuation is not entirely electrostatic as designed – it turns out actuation is mostly thermal. Due to an undoped, n = $5 \cdot 10^{16}/cm^3$, 0.45 μm thick InP buffer layer grown beneath the device layers during MBE growth, there is a significant substrate leakage current during actuation. This induces a thermal strain in the waveguides with causes them to buckle. The second generation of InP waveguide MEMS couplers is currently being developed with no InP buffer layer and incorporating p-n junctions between the waveguides and the sacrificial layer. Early results show switching times for these electrostatically-actuated waveguide couplers as fast as 30 us and actuation voltages as low as 3.7 V. [42]

A similar device, the 1x2 waveguide switch, is also under development [43]. An SEM image of a fabricated 1x2 waveguide switch with is shown in Figure 5-11. The switch is designed to be laterally actuated via electrostatic comb-drive actuators. A

mechanical clamping system of serpentine tethers has been designed to prevent the long single-ended suspended waveguide from curling upwards due to the strain gradient induced during MBE growth. This allows for both low-voltage actuation (< 10V) and mechanically flat waveguides. This first generation of fabricated switches can not be tested, however, due to poor electrical isolation as a result of the InP buffer layer as discussed in [42]. This buffer layer has been removed for the next generation of 1x2 InP waveguide MEMS switches that are currently under development.

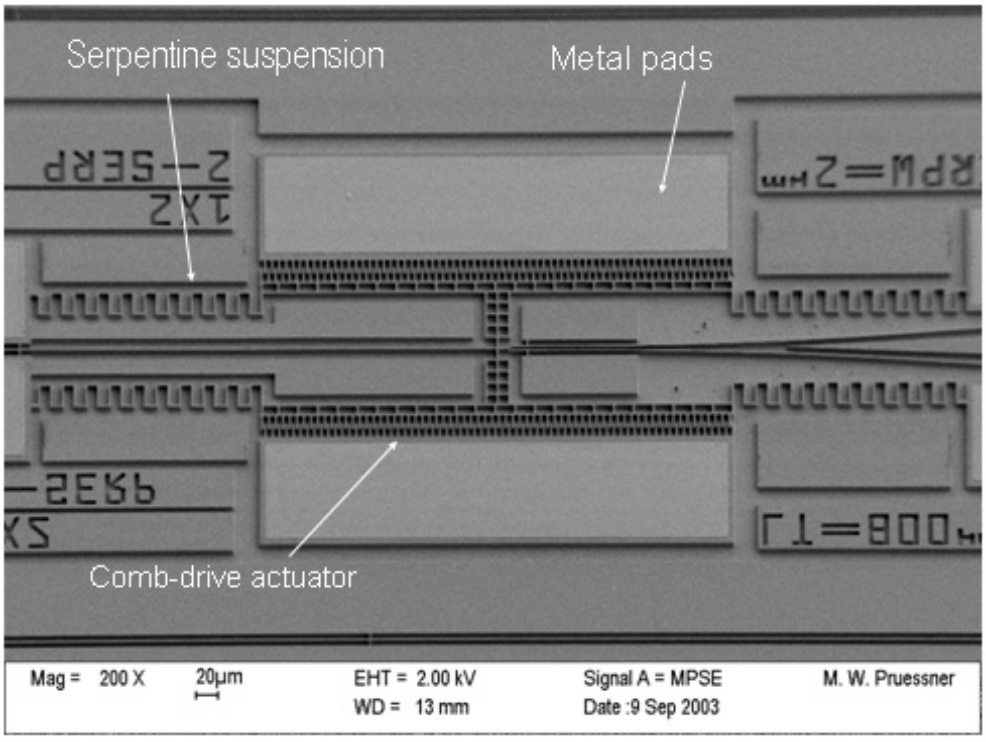

Figure 5-11: SEM image showing an entire 1x2 InP waveguide MEMS switch. The image shows the input and output waveguides, serpentine suspension, comb-drive actuator, and metal contact pads [43].

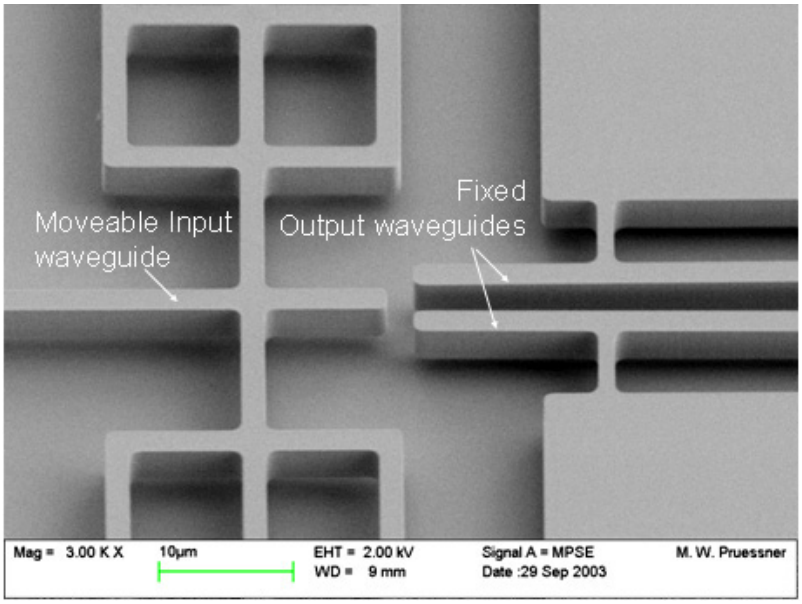

Figure 5-12: SEM image showing close-up of the input and output waveguides. The input waveguide is movable and attached to the comb-drive actuators, as shown in Figure 11 [43].

InP Vertical Fabry-Perot tunable filters have been reported in [44], however vertical filters can not be monolithically integrated in a planar photonic integrated circuit. Fabrication of an in-plane, monolithic Fabry-Perot tunable filter that can be integrated with a photonic integrated circuit is highly desirable. A MEMS in-plane Fabry-Perot tunable filter using InP suspended waveguide technology is currently under development [45]. Figure 12 shows a schematic of the device, which uses a pair of Bragg reflectors fabricated directly on the ends of the waveguides and axial electrostatic actuation to vary the gap between the Bragg reflectors. Figure 13 shows the theoretical spectral response of this filter. The resolution and wavelength range addressable by this in-plane filter allows it to be tuned to any of the Coarse Wavelength Division Multiplexed (CWDM) wavelengths, making it suitable as a channel selector in a CWDM system.

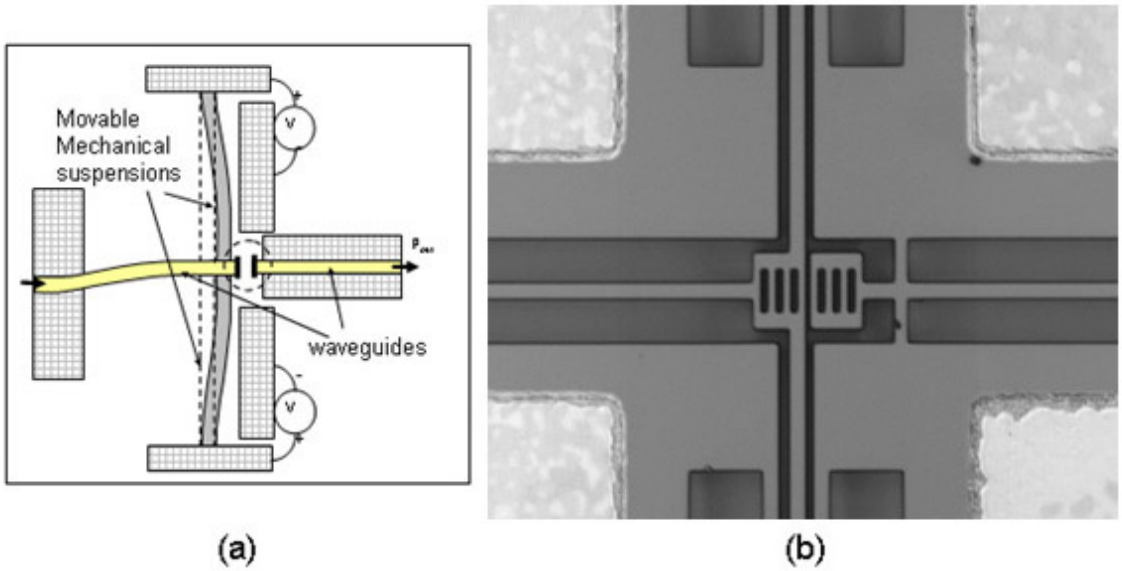

Figure 5-13: (a) Schematic of in-plane tunable Fabry-Perot filter [45] and (b) SEM image showing a close-up of the resonant cavity and Bragg reflectors fabricated directly on the ends of the waveguides [courtesy: Madhumita Datta].

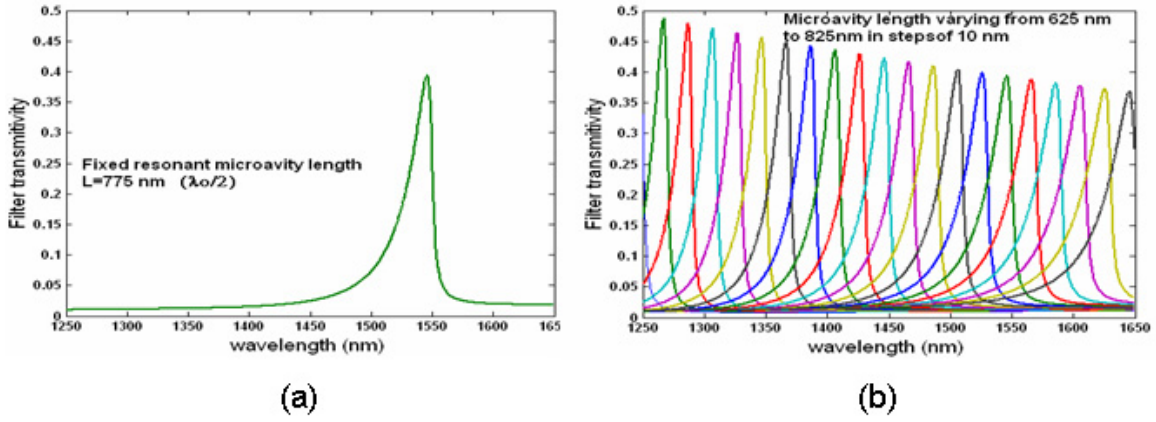

Figure 5-14: Theoretical spectral response of in-plane Fabry-Perot tunable filter for (a) fixed resonant cavity length of 775nm and (b) cavity length tuned from 625nm to 825nm in 10nm steps [45].

Even though the devices reviewed here only represent the first generation of InP MEMS using suspended waveguide technology, they perform a broad assortment of functions. Monolithic, in-plane optical routing, switching, variable splitting/attenuation, and tunable filtering can all be performed in the 1550 nm wavelength regime. The only

fabrication step required in addition to the basic suspended waveguide is a metal electrode deposition for electrical contact to the devices. The use of suspended InP waveguides as the building block for all of these devices demonstrates the robustness and flexibility of the suspended waveguide as an optical MEMS platform technology.

5.5 Conclusion

We have demonstrated monolithically fabricated, suspended InP waveguides for use in optical waveguide MEMS. These waveguides integrate movable and fixed segments with a single lithography step, allowing both optical routing and MEMS functions such as switching and attenuation to be performed laterally on the same chip. The waveguide propagation loss is 2.2 dB/cm and the novel 1.5 μm tethers used to support the waveguide have been shown to induce 0.24 dB of loss per tether pair with waveguide lengths up to 2.5 mm supported between tethers. Additionally, future devices could decrease the tether loss to 0.08 dB per tether pair by using 0.5 μm wide tethers. Several applications of InP suspended waveguide technology are currently under development, including a MEMS waveguide evanescent coupler, 1x2 optical switch, and in-plane Fabry-Perot tunable filter. Additionally, because these devices are all constructed on a common foundation – suspended InP waveguides - eventual monolithic integration of several devices becomes straightforward. By providing good optical confinement and low-loss propagation as well as the ability for in-plane electrostatic actuation, suspended InP waveguides can bridge the gap between InP waveguide optics and InP MEMS devices, positioning them as an enabling technology for InP waveguide MEMS.

References

[1] Kovacs, G.T.A., Maluf, N.I., Petersen, K.E., "Bulk Micromachining of Silicon", Proceedings of the IEEE, vol. 86, no. 8, pp. 1536-1551, Aug. 1998.

[2] Bustillo, J.M., Howe, R.T., Muller, R.S., "Surface Micromachining for Microelectromechanical Systems", Proceedincs of the IEEE, vol. 86, no. 8, pp.1552-1573, Aug. 1998.

[3] Chaudhry, M. S., et. al., "WDM Transmission Limitations in Non Dispersion Shifted and Non-Zero Dispersion Shifter Fibres", IEE, 1999.

[4] Yariv, Amnon, Optical Electronics in Modern Communications, Oxford University Press, New York, 1997.

[5] Hornbeck, Larry J., "Digital Light Processing™: A New MEMS-Based Display Technology", Texas Instruments, 1995.

[6] "Lucent Technologies Announces the World's First High-Capacity, All-Optical Router – Moving Ten Times Today's Internet Traffic", http://www.lucent.com/press/1199/991109.nsa.html, Lucent Technologies Press Release, November 9, 1999.

[7] Leclercq, J.-L., et. al., "InP-Based MOEMS and Related Topics", J. Micromech. Microeng., vol. 10, pp. 287-292, 2000.

[8] Pennings, E., Khoe, G.-D., Smit, M.K., Staring, T., "Integrated-Optic Versus Microoptic Devices for Fiber-Optic Telecommunication Systems: A Comparison", IEEE J. Sel. Top. Quant. Elec., vol. 2, no. 2, pp. 151-164, June 1996.

[9] Soref, R.A., "Silicon-Based Optoelectronics", Proceedings of the IEEE, vol. 81, no. 12, pp. 1687-1706, Dec. 1993.

[10] Bakke, T., et. al., "Planar Microoptomechanical Waveguide Switches", IEEE J. Sel. Top. in Quantum Electronics, vol. 8, no. 1, Jan/Feb 2002.

[11] Ollier, E., "Opitcal MEMS Devices Based on Moving Waveguides", IEEE J. Sel. Top. in Quantum Electronics, vol. 8, no. 1, Jan/Feb 2002.

[12] Sakata, T., Togo, H., Makihara, M., Shimokawa, F., Kaneko, K., "Improvement of Switching Time in a Thermocapillarity Optical Switch", J. Lightwave Technology, vol. 19, no. 7, pp. 1023-1027, July 2001.

[13] “NSM Archive - Physical Properties of Semiconductors”, http://www.ioffe.rssi.ru/SVA/NSM/Semicond/, Ioffe Physico-Technical Institute, St. Petersburg, Russian Federation, 2003.

[14] Keiser, G. Optical Fiber Communications, McGraw-Hill Companies, Inc., Boston, MA, 2000.

[15] Vail, E.C., Li, G.S., Yuen, W., Chang-Hasnain, C.J., “High performance micromechanical tunable vertical cavity surface emitting lasers”, Electronics Letters, vol. 32, no. 20, pp. 1888-1889 Sep. 1996.

[16] Shen, S-C., Caruth, D., Feng, M., “Broadband Low Actuation Voltage RF MEM Switches”, IEEE GaAs Digest, pp. 161-164, 2000.

[17] Thijs, P.J.A., Tiemeijer, L.F., Kuindersma, P.I., Binsma, J.J.M., Van Dongen, T., “High-Performance 1.5 um Wavelength InGaAs-InGaAsP Strained Quantum Well Lasers and Amplifiers”, J. Quantum Electronics, vol. 27, no. 6, pp. 1426-1439, June 1991.

[18] Gini, E., Melchior, H., “Thermal Dependence of the Refractive Index of InP Measured with Integrated Optical Demultiplexer”, J. Appl. Phys., vol. 79, no. 8, pp. 4335-4337, April 1996.

[19] Dantec, R.L., et. al., “Optical Characterization Methods of InP Based Micro-Opto-Electro-Mechanical Systems”, Proceedings of the SPIE, vol. 3008, pp.258-264, 1997.

[20] Greek, S., et. al., “The Strength of Indium Phosphide Based Microstructures”, Proceedings of the SPIE, vol. 3008, pp. 251-257, 1997

[21] Fricke, K., Peiner, E., Chahoud, M., Schlachetzki, A., “Fracture Properties of InP Microcantilevers by Hetero-Micromachining”, Sensors and Actuators A (physical), vol. 76, no. 1-3, pp. 395-402, Aug. 1999.

[22] M. W. Pruessner, "Toward III-V Optical MEMS: Mechanical Property Measurement of Indium Phosphide Using Nanoindentation, Beam Bending, and Electrostatic Testing Methods," Master's Thesis, University of Maryland, College Park, MD, October 2002.

[23] Hjort, K., “Sacrificial Etching of III-V Compounds for Micromechanical Devices”, J. Micromech. Microeng., vol. 6, pp. 370-375, 1996.

[24] Broberg, B, Lindgren, S., “Refractive index of $In_{(1-x)}Ga_{(x)}As_{(y)}P_{(1-y)}$ layers and InP in the transparent wavelength region”, J. Appl. Phys. vol. 55, no. 9, pp. 3376-3381, 1984.

[25] Adachi, S., "Refractive indices of III-V compounds: key properties of InGaAsP relevant to device design", J. Appl. Phys., vol. 53, no. 8, pp. 5863-5869, 1982.

[26] LaPierre, R.R, Okada, T., Robinson, B.J., Thompson, D.A, Weatherly, G.C., "Spinodal-like decomposition of InGaAsP/(100) InP grown by gas source molecular beam epitaxy", J. Crystal Growth, vol. 155, pp. 1-15, 1995.

[27] Madou, Marc J., Fundamentals of Microfabrication, Second Edition, CRC Press LLC, Boca Raton, FL, 2002.

[28] Rickman, A.G., Reed, G.T., Namavar, F., "Silicon-on-Insulator Optical Rib Waveguide Loss and Mode Characteristics", J. Lightwave Technology, vol. 12, no. 10, pp.1771-1776, Oct. 1994.

[29] Holloway, P.H, McGuire, G.E., Handbook of Compound Semiconductors: Growth, Processing, Characterization, and Devices (Materials Science and Process Technology Series), Noyes Publications, Park Ridge, NJ, 1996.

[30] Rommel, S.L., Jang, J-H., Lu, W., Cueva, G., Zhou, L., "Effect of H_2 on the etch profile of Inp/InGaAsP alloys in $Cl_2/Ar/H_2$ inductively coupled plasma reactive ion etching chemistries for photonic device fabrication", J. Vac. Sci. Technol. B, vol. 20, no. 4, oo. 1327-1330, Jul/Aug 2002.

[31] Diniz, J.A., Swart, J.W., Jung, K.B., Hong, J., Pearton, S.J., "Inductively Coupled Plasma Etching of In-Based Compound Semiconductors in $CH_4/H_2/Ar$", Solid-State Electronics, vol. 42, no. 11, pp. 1947-1951, 1998.

[32] Carter, A.J., et. al., "Dry etching of GaAs and InP for optoelectronic devices", IEE Proceedings, vol. 136, pt. J, no. 1, pp. 2-5, Feb. 1989.

[33] Grover, R., Hryniewicz, J. V., King, O. S., Van, V., "Process development of methane-hydrogen-argon-based deep dry etching of InP for high aspect-ratio structures with vertical facet-quality sidewalls", J. Vac. Sci. Technol. B, vol. 19, no. 5, pp.1694-98, Sep/Oct 2001.

[34] Misaka, A., Harafuji, K., "Simulation study of micro-loading phenomena in silicon dioxide hole etching", IEEE Transactions on Electron Devices, vol. 44, no. 5, pp. 751-760, May 1997.

[35] Seassal, C., Leclercq, J. L., Viktorovitch, P., "Fabrication of InP-based freestanding microstructures by selective surface micromachining", J. Micromech. Microeng., no. 6, pp. 261-265, 1996.

[36] Tanner, D. M., "Reliability of surface micromachined MicroElectroMechanical actuators", 22nd International Conference on Microelectronics, vol. 1, pp. 97-104, May 2000.

[37] “Critical Point Dryers Technique”, http://www.2spi.com/catalog/instruments/dryers_technique.html, Structure Probe, Inc. 2004.

[38] Deri, R.J., “Low-Loss III-V Semiconductor Optical Waveguides”, IEEE J. Quant. Elect., vol. 27, no. 3, pp. 626-640, March 1991.

[39] Haruna, M., Segawa, Y., Nishihara, H., “Nondestructive and Simple Method of Optical-Waveguide Loss Measurement with Optimisation of End-Fire Coupling”, Electronics Letters, vol. 28, no. 17, pp. 1612-1613, Aug. 1992.

[40] Takeuchi, H., Oe, K., “Low-Loss Single-Mode GaAs/AlGaAs Miniature Optical Waveguides with Straight and Bending Structures”, J. Lightwave Tech., vol. 7, no. 7, pp. 1044-1054, July 1989.

[41] Ma, Y., Park, S., Wang, L., Ho, S.T., “Low-Loss and Strongly Confined InGaAsP-InP Optical Waveguide Fabricated by Benzocyclobutene Wafter Bonding”, LEOS ’99, vol. 2, pp. 754-755, Nov. 1999.

[42] M. W. Pruessner, K. Amarnath, M. Datta, D. Kelly, S. Kanakaraju, P.T. Ho and R. Ghodssi, "Optical and Mechanical Characterization of an Evanescent Coupler Optical Switch," Technical Digest of the 2004 Solid-State Sensor, Actuator and Microsystems Workshop (Hilton Head 2004), pp.238-241, Hilton Head Island, SC, June 6-10, 2004.

[43] M. W. Pruessner, D. Kelly, M. Datta, H.Lim, R. Maboudian and R. Ghodssi, "Design and fabrication of an InP-based Moving Waveguide 1x2 Optical MEMS Switch," Proceedings of the 2003 International Semiconductor Device Research Symposium (ISDRS), p. 280, Washington, DC, December 10-12, 2003.

[44] Spisser, A. et. al., "Highly selective and widely tunable 1.55-μm InP/air-gap micromachined Fabry-Perot filter for optical communications", IEEE Photonics Technology Letters, vol. 10, no. 9, pp. 1259-1261, Sep. 1998.

[45] M. Datta, M. W. Pruessner, D. Kelly and R. Ghodssi, "MEMS-Tunable Novel Monolithic Optical Filters in InP with Horizontal Bragg Mirrors," Proceedings of the 2003 International Semiconductor Device Research Symposium (ISDRS), p. 282, Washington, DC, December 10-12, 2003.